PHOTONIC ANALOG-TO-DIGITAL CONVERTERS

AIR FORCE RESEARCH LABORATORY
SENSORS DIRECTORATE
ROME RESEARCH SITE
ROME, NEW YORK

STINFO FINAL REPORT

This report has been reviewed by the Air Force Research Laboratory, Information Directorate, Public Affairs Office (IFOIPA) and is releasable to the National Technical Information Service (NTIS). At NTIS it will be releasable to the general public, including foreign nations.

AFRL-SN-RS-TR-2006-109 has been reviewed and is approved for publication

APPROVED: /s/

              MICHAEL J. HAYDUK
              Acting Chief, Electro-Optic Components Branch
              Sensors Directorate

FOR THE DIRECTOR: /s/

              RICHARD G. SHAUGHNESSY, Chief
              Rome Operations Office
              Sensors Directorate

REPORT DOCUMENTATION PAGE

Form Approved
OMB No. 074-0188

1. AGENCY USE ONLY (Leave blank)	2. REPORT DATE MARCH 2006	3. REPORT TYPE AND DATES COVERED In-House Feb 99 – Sep 05

4. TITLE AND SUBTITLE
PHOTONIC ANALOG-TO-DIGITAL CONVERTERS

5. FUNDING NUMBERS
C - N/A
PE - 62204F
PR - PADC
TA - SN
WU - 01

6. AUTHOR(S)
Rebecca Bussjager, Michael Hayduk, Steven Johns, Michael Fanto, Reinhard Erdmann, Joseph Osman, John Malowicki and David Winter

7. PERFORMING ORGANIZATION NAME(S) AND ADDRESS(ES)
Air Force Research Laboratory/SNDP
25 Electronic Parkway
Rome New York 13441-4515

8. PERFORMING ORGANIZATION REPORT NUMBER

9. SPONSORING / MONITORING AGENCY NAME(S) AND ADDRESS(ES)
Air Force Research Laboratory/SNDP
25 Electronic Parkway
Rome New York 13441-4515

10. SPONSORING / MONITORING AGENCY REPORT NUMBER

AFRL-SN-RS-TR-2006-109

11. SUPPLEMENTARY NOTES

AFRL Project Engineer: Rebecca Bussjager/SNDP/(315) 330-2918/ Rebecca.Bussjager@rl.af.mil

12a. DISTRIBUTION / AVAILABILITY STATEMENT
APPROVED FOR PUBLIC RELEASE; DISTRIBUTION UNLIMITED.

12b. DISTRIBUTION CODE

13. ABSTRACT *(Maximum 200 Words)*

This report addresses the development of photonic analog-to-digital converters (ADCs) based on InP technology, a path that could lead to a fully integrated photonic ADC. The historical background of electronic ADC's is followed by a detailed description of photonic ADC architectures pursued by the SNDP in-house Photonic ADC team. The development and the importance of the key components are also presented, namely lasers, modulators, and quantizers. It was initially anticipated that a demonstration of the photonic ADC could be made available for the AFRL Monobit cueing receiver; however, the program was ended before this goal could be achieved. This report summarizes the results obtained up to that point.

14. SUBJECT TERMS
Photonic ADC, O-E Conversion, Optical to Electrical Conversion, Saturable Absorber Etalons, Fiber Laser, Phase Noise, Timing Jitter, Electro-Absorption Modulators, EAMs

15. NUMBER OF PAGES
110

16. PRICE CODE

17. SECURITY CLASSIFICATION OF REPORT	18. SECURITY CLASSIFICATION OF THIS PAGE	19. SECURITY CLASSIFICATION OF ABSTRACT	20. LIMITATION OF ABSTRACT
UNCLASSIFIED	UNCLASSIFIED	UNCLASSIFIED	UL

NSN 7540-01-280-5500

Standard Form 298 (Rev. 2-89)
Prescribed by ANSI Std. Z39-18
298-102

Table of Contents

List of Figures

ii

List of Tables

Photonic Analog to Digital Converters

Summary

Analog to digital converters (ADCs) are an essential link between analog sensor systems, such as RADAR, EW and SIGINT, and high-speed digital signal processing systems in providing global information access to the warfighter. Military utilization of high performance analog to digital converter technology is diverse, spanning a wide range of sample rate and bit resolution values. At one extreme there are devices having higher bit counts with lower sample rate, which offer superior signal-to-noise ratio (SNR) and spurious-free dynamic range (SFDR), but are limited in overall bandwidth. At the other end are ADCs that have very high sample rates and wide bandwidths, but with a corresponding reduction in both bit resolution and dynamic range. Electronic ADCs, photonic ADCs and combined opto-electronic ADCs each address various portions of the dynamic range, sample rate and bandwidth parameter space.

Electronic ADC technology has evolved and will continue to provide higher sample rates and bit resolution, but progress in advancing the electronic ADC modules has been slow, due in large part to the difficulties in fabricating the complex electronic circuitry required for very high resolution, and high sampling rate converters. Roughly 6-8 years is required for each bit of electronic improvement[1]; future war fighting capabilities could be severely compromised unless dramatic improvement in ADC modules is made.

The photonic and opto-electronic ADCs have several key advantages, which include more precise sampling times, narrower sampling apertures, and the ability to sample without contaminating the incident signal. They also have the *potential* to improve on the sample rate and bandwidth performance in present ADCs that operate up to the 8 bit range. There were significant challenges to be overcome in developing photonic ADC architectures with the associated components, as well as making them compact, efficient, and environmentally stable. The progress toward those goals in the course of this work has justified the efforts, and the risks, that were required to pursue it.

The photonic ADC team was awarded US Patent # 6,326910 on 4 December 2001 for the design of a low power, passive, photonic ADC quantizer based on saturable absorbers. The basic components of this ADC may be integrated on a single substrate using integrated electro-optic techniques. These devices include the mode-locked laser, electro-absorption modulator, and a quantization mechanism. The passive nature of this architecture makes it well suited for applications requiring low power components. As in electronic flash ADC systems, the total number of quantizers required is equal to $2^N - 1$, where N is the number of bits of resolution.

The photonic ADC team collaborated with photonic and electronic experts in academia and industry to develop a viable solution. These partnerships allowed the ADC ideas in the patent to be explored with applications geared toward the ultrafast, compact, and accurate receivers needed for the data acquisition in the next generation war fighter. Figure 1 depicts how the photonic ADC program was structured, and this document addresses each spoke in the wagon wheel diagram.
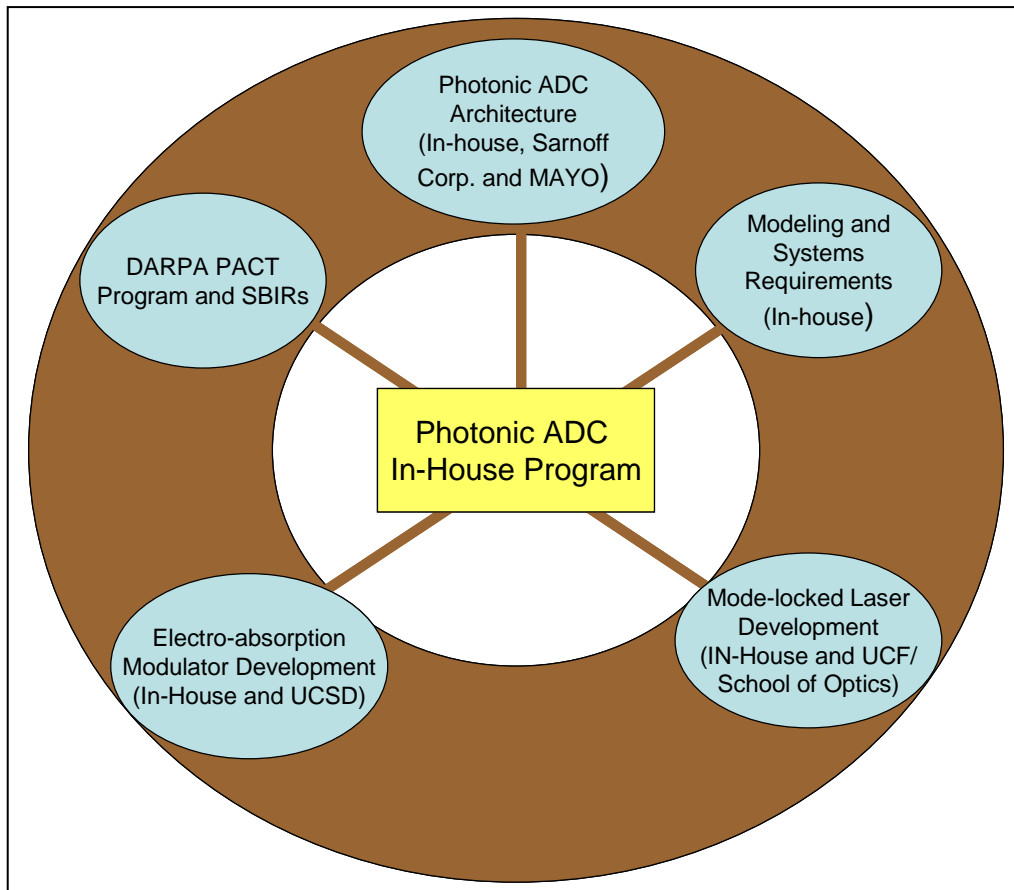
Figure 1. Photonic ADC program extends beyond the focus of an architecture. Emphasis is placed on each technical area depicted in the blue bubbles.

Chapter 1. Introduction

The Photonic ADC program directly applied to sensor technologies such as Force Protection Sensors, Intelligence, Surveillance and Reconnaissance (ISR) Management, and Combat ID (air and surface). Photonic ADCs also applied to other technologies, but for conciseness, attention was confined to the examples provided in this document.

It is the Air Force's (AF) plan to ultimately have a "Sensor Craft" capable of multiple functionalities that provides 360° continuous large area coverage with links to ground, air and space. Some of the functions that meet the above mentioned sensor technologies (but not limited to) include Electronic Warfare (EW) with operation range of 8-14 GHz, Electronic Support Measures (ESM) with operation range of 2-18 GHz, Synthetic Aperture Radar (SAR) with operation range of 7-11 GHz, Ground Moving Target Identification (GMTI) with operating range of 7-11 GHz, and Air Moving Target Identification (AMTI) with 2.8-3.4 GHz for air detection and 1.2-1.4 GHz for space detection. Airborne moving target detection requires a 100-1000 times higher power aperture than GMTI. Current platforms that include some of these technologies are in Table 1-1. Sensor Craft is based on the need for integrated and interactive ISR to support dynamically changing combat operations.

Table 1-1. Current platforms that include various technologies.

Platform	Technology Function
AWACS (AF, NATO)	ESM[3], (GMTI, AMTI)[4,5]
Prowler (Navy)	EW[6,7]
Compass Call (AF)	EW[4,6,7]
Rivet Joint (AF)	(EW/ELINT)[4]
U2 (AF)	(EO, SIGINT, SAR, GMTI*)[8,9]
Global Hawk (AF)	(SAR, GMTI, AMTI*)[8]
Joint Surveillance and Target Attack Radar System (JSTARS)	(SAR, GMTI)[4,8]
Joint Strike Fighter (JSF)	(ESM,(EW,(GMTI,AMTI)[10])[11])[12]
Discoverer II (DII) (AF, NRO, DARPA)	(SAR, GMTI, AMTI)[13]
*with Active Electronically Steered Array (AESA) upgrades	

These sensor technologies are better understood when it is clear what the warfighters' needs are and what enabling technologies provide the capabilities to fit these needs. For instance, in the Force Protection Sensors area, the warfighter needs improved countermeasures against an RF threat, and one of the enabling technologies that helps meet this need is a state-of-the-art digital receiver. Modern digital receivers aid in robust self protection against modern threat radars by analyzing received signals faster and more accurately and in turn provide necessary information to jammers against these threat radars. As always, newer receiver technology must also have reduced size, weight, power and cost.

Another example is Multi-integrated Sensors for Persistent (MISP) ISR technology. The warfighter needs positive identification of air and ground targets, detection and warning of an RF threat, as well as improved target intelligence. The digital receiver must be able to detect, track and identify the RF signal in all weather conditions and with high confidence quickly and accurately. A lesson learned in Kosovo was that mobile targets were effectively hidden by foliage, caves and cloud cover[14], so improved sensors are needed to penetrate these

concealments. The third example, which is related to Combat ID as well as ISR management, is the warfighters need to reduce the susceptibility of detection by enemy ground, air and space RF sensors. Once again, enhanced digital receivers are required to meet these needs. Receivers need to provide the capability of collecting information from simultaneous RF frequencies and must be able to analyze quickly and precisely the information being tracked and targeted in order to reduce vulnerability.

Enhanced digital receivers would enable many other sensor-based technologies that are too numerous to elaborate on in this report. However, an example worth describing is the concept of Space-Based Sensing and the "Connected Battlespace". Secretary of the Air Force James Roche and Chief of Staff Gen. John Jumper made a statement to Congress on the FY03 Budget, "[The AF] is focusing on the horizontal integration of our manned, unmanned, and space assets in order to provide real time actionable, exploitable, intelligence to our commanders"[15]. This statement reinforces that the warfighter needs undeniable all weather surveillance with rapid global revisit while the battlefield commander needs near real time information. Again digital receivers can help meet these needs by enabling the processing of received information in space with precision in minutes. This enhanced capability provides rapid satellite revisitation and provides near real time access to theater commanders as well as rapid battlefield status beyond the theater. Interaction with other systems such as unmanned air vehicles (UAVs) is now possible. A "Deep Look" from space using periodic sampling occurs with the space-based Discoverer II (DII) platform and currently revisits every 15 minutes[13]. A goal of Sensor Craft is to provide continuous coverage complementing DII.

Analog-to-digital converters are critical components in the development of advanced digital receivers. Wide bandwidth and high resolution ADCs will allow direct quantization of the sensor signal at RF frequencies, thereby eliminating the need for analog down conversion stages. Direct conversion also allows the ADC to be placed closer to the antenna front end. With the digital interface closer to the sensor/antenna in military receivers, costly temperature sensitive components that introduce distortions and require considerable calibration will be reduced[16-18]. Increased digital content also increases flexibility and functionality because the suppression of signals can be significantly enhanced through digital filtering and beam forming [16-18].

Current wide bandwidth receivers must go through at least a single down conversion process so that the RF signal can be processed by the ADC at baseband data rates. Electronic ADCs, therefore, create a bottleneck in digital receivers. For example, an X-band receiver, with 4 GHz of bandwidth centered at 10 GHz, requires a mixer stage with a local oscillator, a bandpass filter, a phase shifter, a low pass filter and finally an ADC. Though this type of receiver has a single down conversion stage, an enormous improvement over older receivers with double down conversion stages, there is still a large number of analog components, which leads to reliability and power consumption issues.

Research in photonics and electronics is needed to surpass existing electronic ADC limitations, which are discussed in depth in Chapter 2, "Electronic ADC Architectures". Photonics is by nature wideband (THz) and lightweight making it is well suited for high-speed signal conversion. Specifically, photonic ADCs have the advantage of precise sampling times, narrow optical sampling apertures, and the ability to sample without contaminating the incident signal. Signal sampling with optical pulses could eliminate the need for a sample and hold circuit, a performance limiting component in conventional high speed ADCs[19]. These factors make photonic ADCs a promising fit in digital receiver systems.

DARPA recognized the potential benefits of photonics for signal conversion and started the four year Photonic A/D Converter Technology (PACT) program in 1999. The program had aggressive goals which far surpass current state-of-the-art electronic ADC performance. The primary goal entailed a sample rate of 10 GS/s for 5 GHz instantaneous bandwidth (BW) with 12 to 14 bits of resolution. A secondary goal was a sampling rate of 100 GS/s with 50 GHz of instantaneous bandwidth with 4 bits of resolution. SNDP leveraged the DARPA program to build an in-house Photonic ADC Program primarily focused on addressing AF warfighter needs. SNDP's architecture was distinct from the others developed under the PACT Program, as is clearly shown in the documented comparison to two other photonic alternatives discussed in Chapter 3.

The physical dimensions of systems and subsystems in Air Force platforms can not be overlooked, as it determines the practicality of photonic ADCs. Photonic ADCs must have a maximum footprint of approximately 2 inches by 2 inches in keeping with the traditional space requirements of electronic ADCs. By imagining conceptually a 2-D conformal antenna placed on an aircraft wing, one can envision the tight size constraints of future digital receivers. The requirement that two entire receivers, such as a UHF (0.3-3.0 GHz BW) and an X-band receiver, both fit in the wing dictates the compact size of a photonic ADC. Most wing based antenna/receiver modules are located on the trailing edge of the wing, especially at low frequencies such as UHF where the antenna size tends to be large. Higher frequencies like X-band can be in the nose or the belly of the craft since these antennas are smaller in size. However, this further necessitates small receiver modules for them to reside in the nose or belly regions. The concept of conformally integrating low frequency and high frequency applications can be employed in platforms such as an advanced Global Hawk design, and it is certainly part of Sensor Craft because conformal designs can provide large angular coverage over an examined area.

SNDP's in-house flash photonic ADC architecture and the overall program are explained in the remaining sections of this document. This program was not directly supported by DARPA, but the DARPA PACT goals were appreciated by SNDP team members, and those goals pushed the state-of-art ADC technology well beyond the traditional electronic limits. Though the in-house team considered working towards the PACT goals, Air Force specifications and needs were primary goals. Through the PACT program, members of SNDP's in-house ADC team made contact with several contractors in the PACT program and established productive working relationships and collaborations.

The Photonic ADC Program was specifically geared to address the Air Force warfighters' needs. Changes were made to original ideas, both technically and programmatically, due to simulations and experimental findings. Based on these a design plan was formulated that led to a working integrated photonic ADC. The significant discoveries made in the course of that work are detailed in this report, though the program ended before an integrated photonic ADC could be achieved.

The photonic ADC architecture used as a general photonic ADC, including the SNDP system, is represented in Figure 1-1. The primary photonic components, and keys to its success, are the mode-locked laser, the electro-optic modulator, and the quantizer. The quantization scheme is the subsystem that had many alternative approaches. The specifications for all of these components were highly specialized, and in general not commercially available.
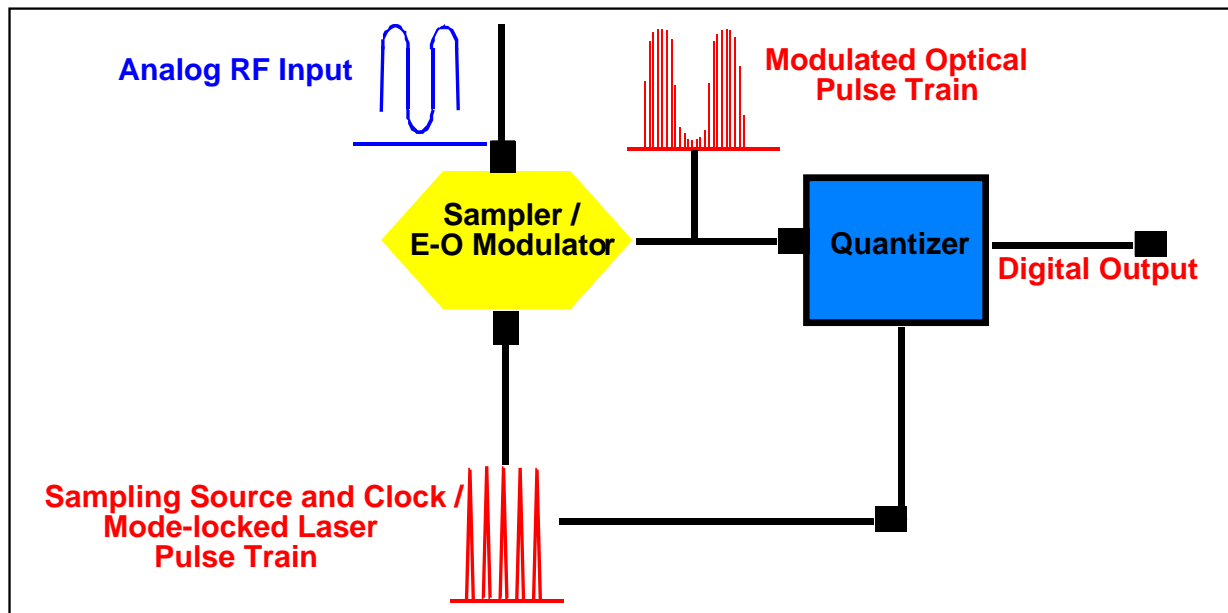
Figure 1-1. Photonic analog to digital converter block diagram.

A primary element of this program was focused on quantization using saturable absorbers (SAs). Modeling, fabricating and testing of saturable absorbers was performed, and the structures were examined in surface normal configurations initially and later within etalons in both surface normal orientations and waveguide structures. This was done in-house and through partnerships with the University of Rochester and Sarnoff Corp. The saturable absorbers were used to provide the "dynamic ranging" in the quantization mechanism, and the operation of these structures is explained in Chapter 3.

An opto-electronics (O/E) module followed the saturable absorbers. This module was developed through industry collaboration with Discovery Semiconductors and the MAYO Foundation, and it is typically referred to as the "back-end" electronics. The staff at Discovery Semiconductors includes leading experts in InP detectors on speed, linearity, and optical power handling. The Mayo Foundation, more specifically, the Special Purpose Processor Development Group (SPPDG), is a nonprofit group that performs state-of-the-art electronics and signal processor research. They are an unbiased, neutral party technology developer who is not viewed as competitive by corporations. This allowed true partnering for advancing the technology.

The conceptual O/E module included a photodiode, a photonic integrate and reset circuit, and an electronic comparator. The O/E module essentially converted the optical signal back to an electronic signal. The output electronic signal following the comparator was in traditional digital format suitable for further signal processing. Information on this subject can be found in Sensors AFRL technical report entitled, "Development of High Performance Electronics and Optical-To-Electrical Advanced Circuitry for Photonic Analog-To-Digital Converters"[20].

Also in collaboration with industry and academia, one concentration was on electro-absorption modulators (EAMs) rather than Mach-Zehnder modulators because of their size, weight and material compatibility in InP. Incorporating EAM modulators would allow integration of the saturable absorbers with photodiodes and InP based electronics that may form the remaining components of the ADC architecture. EAMs are presented in Chapter 4, "Electro-absorption Modulators".

A fourth goal of this in-house program was to construct an environmentally stable, compact laser source with timing jitter of less than 10 fs over an integration interval of 10 Hz-5 MHz. The first system, a contractual effort with the University of Central Florida (UCF) School of Optics (Center for Research in Electro-Optics and Lasers), was based on a semiconductor laser diode placed within an external cavity. The second system, which built upon SNDP's past experience in fiber lasers, was a coupled opto-electronic oscillator (COEO) which eliminated the need for an expensive, large, heavy RF source to provide the mode-locking. Additional investigations included high concentration Er-doped fibers and an Er-doped waveguide as gain media. A discussion on various laser performances is provided in Chapter 5, "Mode-Locked Lasers".

Chapter 6 concludes the report with a summary of the in-house approach, a discussion of its limitations, and recommendations for related future work. This chapter is followed by a series of Appendices that provide the various computer routines used in the experimental portions of this in-house program.

Chapter 2. Electronic ADC Overview

Pushing the performance of ADCs is challenging due to the limits of noise, device matching and integration density. Sampling speed tends to be limited by transistor speed and interconnect parasitics[21] and in switched capacitor techniques by the settling time of op amps[22]. The effective number of bits (ENOB) is inversely related to the sample rate. The distribution of resolution versus sampling rate has become know as the "The Walden Wall", shown in Figure 2-1, and it provides insight into ADC performance limitations[1,2].

The theoretical, RMS noise is caused by the quantization error of the ideal converter. The quantization error in an ADC occurs because each output conversion code can occur across a small range of the input voltage signal, hence the error. The difference between stated resolution, or ENOB, and SNR bits for a given ADC indicates the degradation in SNR due to all other error sources and exhibits this difference with a degradation of approximately 1.5 bits for a given sampling rate[1]. Ideally, the Signal-to-Noise Ratio (SNR) of a converter is equal to

$$SNR_{dB}=6.02n + 1.76 \text{ dB}, \qquad\qquad (2\text{-}1)$$

$$\text{And so SNR bits} =(SNR_{dB}\text{-}1.76)/6.02 \qquad\qquad (2\text{-}2)$$

where n is equal to the number of converter bits and is required over the full operational bandwidth. In Figure 2-1 the y-axis is labeled as SNR bits.

From the chart for sampling rates below 7 Ms/s, resolution appears to be limited by thermal noise. At sampling rates ranging from ∼ 7 Ms/s to ∼ 4 Gs/s, resolution is attributed to uncertainty in the sampling instant due to aperture jitter. The speed of the device technology is also a limiting factor for ADC's operating faster than a 4 Gs/s rate due to comparator ambiguity. In attempts to push back these limits, many ADC architectures and integrated circuit technologies have been proposed and implemented through the years. In recent years the trend toward single-chip ADCs brought lower power dissipation. The Walden Wall illustrates a downward trend; as ADCs advance in sampling speeds, the resolution decreases. It takes approximately 6-8 years for an ADC in development to increase one bit at a particular set sample rate[1].
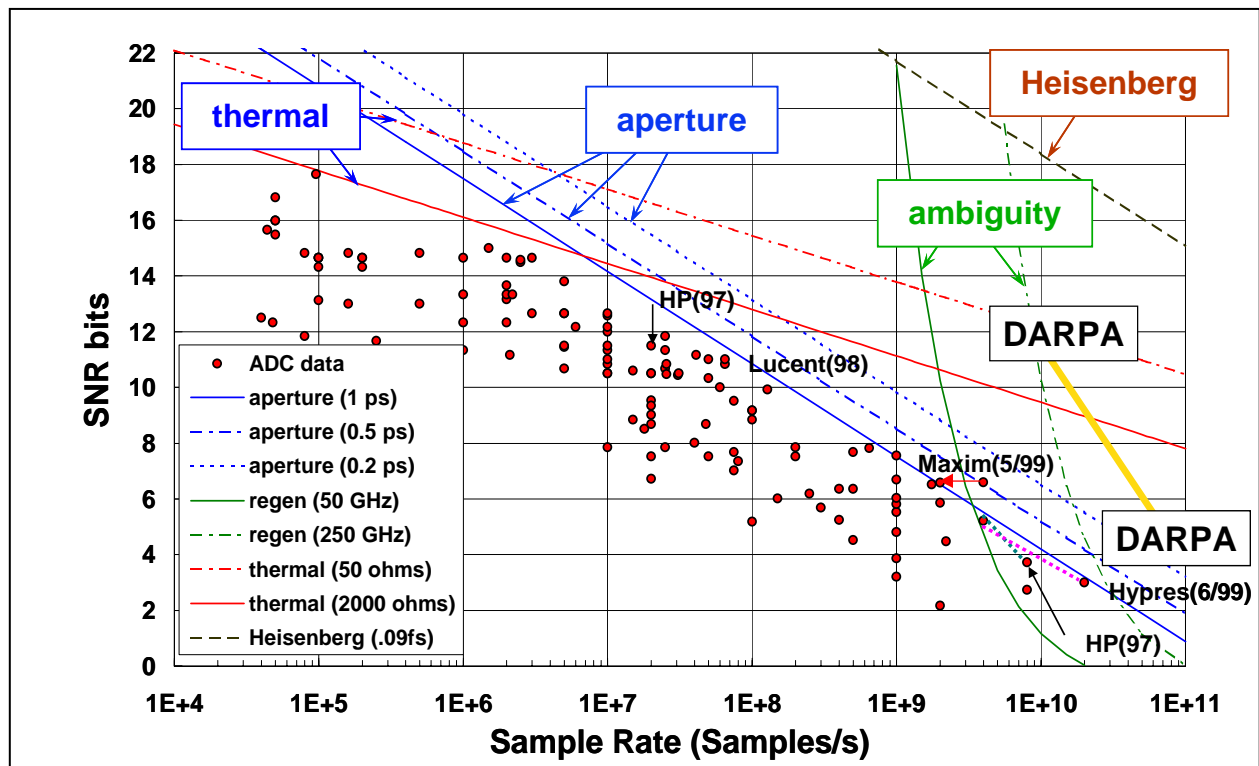
Figure 2-1. Walden Wall with electronic limitations[1,2].

Various types of ADC and their applications are in the following table:
Table 2-1. Matrix of ADC's and Their Applications [23,24].

ADC Architecture	Typical Sampling Speed	Typical Resolution	Applications
Integrating (a.k.a. Dual Slope)	<50 KS/s	> 18 bits	portable instrument applications, Including digital panel meters and digital multi-meters
Flash	250 MS/s - 1 GS/s +	< 8 bits	data acquisition, satellite communication, radar processing, sampling oscilloscopes, and high-density disk drives
Pipeline	1MS/s - 100 MS/s+	8-16 bits	CCD imaging, ultrasonic medical imaging, digital receiver, base station, HDTV, xDSL, cable modem and fast Ethernet.
Successive-Approximation-Register (SAR)	<5 MSps	8-16 bits	portable/battery-powered instruments, pen digitizers, industrial controls, and data/signal acquisition
Sigma Delta	<1MHz	16-24 bit	audio designs, instrumentation and Sonar
Two Step (a.k.a. Half flash or Subranging)	~MS/s	~8 bits	cross between a flash ADC and pipeline ADC can achieve higher resolution or smaller die size and power for a given resolution when needed

Many factors and loss mechanisms affect ADC performance. As Taylor[19] explains quantization error found in all ADCs results from the fact that the coder output can take on only

a finite number of discrete values, while analog signals vary continuously. The maximum quantization error is given by ΔV/2, and the root-mean-square quantizing error is

$$\epsilon_{rms} = 0.289\Delta V. \tag{2-3}$$

Other common sources of errors are associated with the circuitry. These include drift in the sample-and-hold output and noise in the coding circuits.

Aside from quantization noise, Walden explains further that three mechanisms limit the SNR: thermal noise, aperture uncertainty, and comparator ambiguity[1]. In SNR-bits, B, the associated maximum achievable resolutions, can be calculated by the following equations:

thermal noise:

$$B_{thermal} = \log\left(\frac{V}{6kTR_{eff}f_{samp}}\right)^{1/2} - 1 \tag{2-4}$$

aperture uncertainty:

$$B_{aperture} = \log\left(\frac{2}{\sqrt{3}\left(\pi f_{samp}\tau_a\right)}\right) - 1 \tag{2-5}$$

comparator ambiguity:

$$B_{ambiguity} = \left(\frac{\pi f T}{6.93 f_{samp}\tau_a}\right) - 1.1 \tag{2-6}$$

Where R_{eff}, rms aperture jitter is denoted as τ_a, and f_{samp} is the sampling frequency.

The ultimate limit to ADCs is estimated using the Heisenberg uncertainty principle. Using the equation $\Delta E \Delta t > h/2\pi$, where ΔE is the energy of the smallest resolvable signal (1/2 Least Significant Bit (LSB)), and Δt is half the sampling period (T/2), and h is Planck's constant. Assuming a 1 V peak-to-peak input signal and a 50 Ω impedance, the Heisenberg limit yields 12 bits at 840 GS/s. This limit is ~ 4 orders of magnitude beyond the state-of-the-art which is currently aperture jitter limited. Though there may be other limiting factors beyond aperture jitter and the uncertainty principle, it is essential to first develop a thorough understanding of aperture jitter[1].

Low noise designs that achieve less than 0.5 ps of aperture uncertainty and/or technologies with cutoff frequencies (f_T) >>50GHz are required to further advance the state-of-the-art. Experimental heterojunction bipolar transistor (HBT) and high electron mobility transistor (HEMT) integrated circuit (IC) technologies have been reported for devices with f_T and maximum oscillating frequency (f_{max}) ranging from 150 GHz to 260 GHz[25-29]. An InP/InGaAs and an InAlAs/InGaAs HBT were reported to have a f_T of 186 GHz[29] and an f_{max} of 236 GHz[28]. In contrast to GaAs based devices, the InP based devices show lower breakdown

voltages due to the InGaAs collector[27], and InP based HEMT was shown to be the most promising approach[26].

The fastest ADCs use parallel techniques such as flash architectures. Most of these converters have been fabricated in silicon, while a few have been realized in GaAs and InP. The fastest flash ADC reported (at the time of this program) was an InP HBT developed by HRL,[30] which provided 3 bit resolution and sampled at 20 GS/s.

A flash architecture typically uses 2^N-1 comparators, and flash converters often include one or two additional comparators to measure overflow conditions. All comparators sample the analog input voltage simultaneously, so the number of comparators grows exponentially with N, making it difficult to achieve high resolution, while separate adjacent voltage reference levels grows smaller exponentially. This is a major drawback of flash architectures since accuracy is dependent on comparator offset voltage and full scale range (FSR) of the input signal. Comparator offset voltages have to be smaller than ½ the least significant bit (LSB) which implies that 1 LSB = FSR/2^N [21]. Also, these architectures usually have high power dissipation due to the large number of integrated circuits required. Folded-flash and pipeline architectures have overcome the resolution (< 8 bit) problem while achieving GS/s rates. Time interleaving approaches also obtain high speed conversion, but have approximately an order of magnitude higher power dissipation.

Sigma-delta ($\Sigma\Delta$) modulation combined with digital decimation filtering is an approach that trades speed for resolution[18,22,23,31,32] and requires few analog components. In $\Sigma\Delta$ conversion the analog input signal is oversampled, so the quantization noise in the lower portions of the spectrum relative to the $\Sigma\Delta$ clock frequency is suppressed through integration and feedback. The problem is that RF applications require speed from the IC technology that is difficult to achieve. An InP HBT second-order modulator with a sampling rate of 3.2 Gs/s and an over-sampling ratio of 32 yielding a Nyquist rate of 100 Ms/s was reported by HRL[32]. In $\Sigma\Delta$ technology it is also useful to constrain the digitized bandpass characteristics to be narrowband at each frequency in the spectrum of the signal[18,33,34]. Furthermore, the center frequency of the converter must then be tunable. Subsequently two bandpass $\Sigma\Delta$ modulators reported with a 60 MHz center frequency[18] and an 800 MHz center frequency[34] both sampled at 4 GHz were the fastest bandpass modulators built within the duration of this program.

Another tradeoff in ADC performance involves power dissipation (P_{dis}), since the highest performing converters generally dissipate the most power. A convenient way to include this in the performance comparison is with the use of a figure of merit, F, where

$$F = 2^{SNRbits} \text{ x } f_{samp}/P_{dis.} \tag{2-7}$$

On average ADCs had values of $F < 7.9$ x 10^{10} [1]. The following two examples represent current state-of-the-art performance corresponding to a value of F less than this with aperture jitter of ~ 2 ps. The first ADC operated at 13 SNR-bits, 10 Ms/s, 1.1 W, and the second at 7 SNR-bits, 1 Gs/s, 1.75 W. GaAs based HBTs, with superior electron transport properties and low base/emitter turn on voltages, are attractive for their high frequency range and low power dissipation in IC applications[27], yet the highest reported F, 6.6 x 10^{13}, was observed in a superconducting ADC[1].

Engineers in the electronic domain hope to improve electronic ADC performance with antimonide (Sb) and gallium nitride (GaN) based material systems. These material systems may also benefit photonic architectures. Antimonides have a low bandgap (~ 0.3 eV) and higher

electron mobility than silicon (Si), gallium arsenide (GaAs), and InP. This translates to lower power consumption. Potential electronic progress beyond the Walden Wall limitations should not deter research in the Photonic ADC arena.

Chapter 3. Photonic ADC Architectures

3.1 Highlights of Photonic ADCs Offered by DARPA /PACT

Before the in-house ADC team could attempt to meet the needs of AF users with a photonic ADC which far exceeded electronic state-of the-art performance, it was necessary to focus on a more achievable goal. It was also important to understand the state-of-the-art technology alternatives. As previously mentioned, the DARPA PACT program originally set a primary goal of 10 GS/s sampling rate (5 GHz BW) with 12 to 14 bits of resolution and a secondary goal of 100 GS/s sampling rate (50 GHz BW) with 4 bits of resolution. Two successful working photonic architectures from the PACT program are discussed with speeds and resolutions achieved at the time in this section.

The first one from MIT Lincoln Laboratory (MIT/LL), demonstrated an operating photonic architecture that used time-division-demultiplexing (TDDM) techniques[35]. Figure 3-1 shows the schematic layout. The mode-locked laser sampled the input RF electronic signal using an E-O modulator. The optical signal was demultiplexed from 500 MS/s to 65 MS/s using a series of switches to de-interleave the data down to data rates which were processed by a series of "slow" electronic ADCs (65 MS/s) with high resolution (12 bits). MIT/LL demonstrated 505 MS/s BW operation with 51 dB SNR allowing 8 bits of resolution and a SFDR of 61 dB[35]. Although the BW of 505 MHz was far from the 5 GHz goal, MIT was successful at demonstrating this photonic ADC working on the HAYSTACK Radar (HAX) platform in Massachusetts. This demonstration was noteworthy in demonstrating that photonics can accurately convert an analog signal to a digital signal.
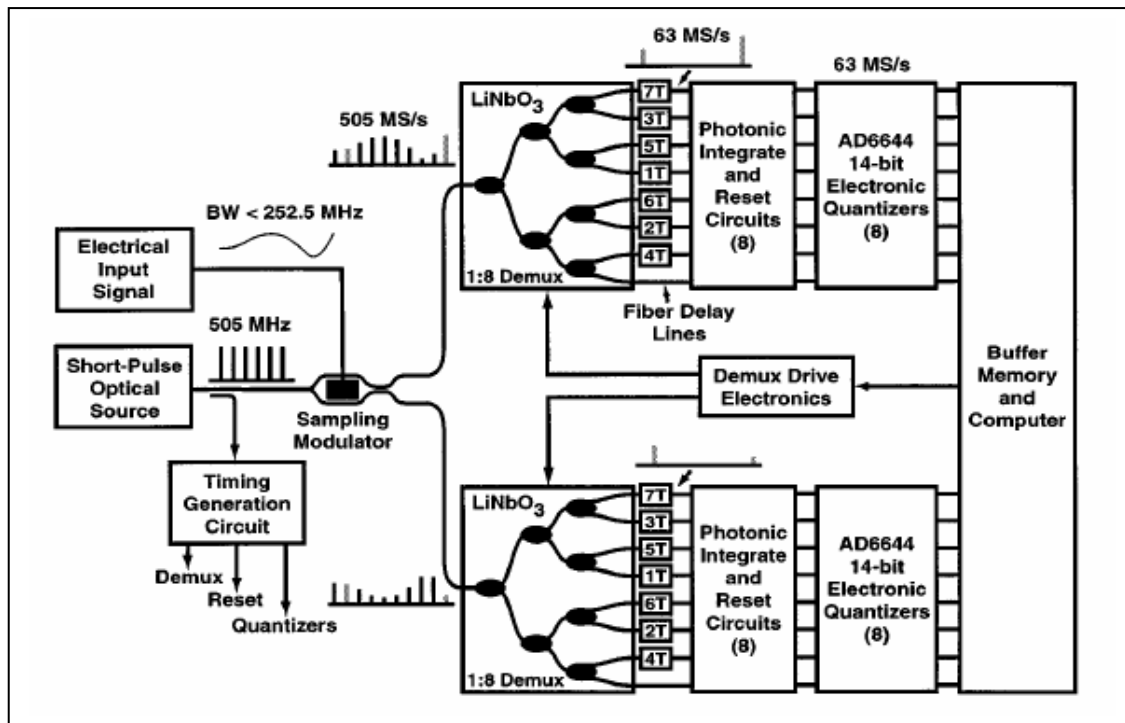
Figure 3-1. Photonic ADC architecture using a time division demultiplexing technique[35].

The main advantage of this approach is that optical sampling allows low-jitter optical impulse signal sampling that does not contaminate the input electrical signal. This design also yields high linearity with a high signal to noise ratio due to the method of phase modulating the optical pulses[35], and it is also insensitive to laser amplitude noise.

A major problem is that integration of this system presents a daunting task because of the multiple electro-optic Mach-Zehnder switches which are large in size and number. The system components were fabricated in many different material systems precluding complete integration. Another draw back is that the phase encoded technique requires twice the number of well calibrated electronic detection and quantization channels as a single output intensity method[35]. One also must consider the effects of pulse degradation and crosstalk in the optical domain due to propagation through the series of switches. Pulse dispersion, spreading the pulse in time as it propagates through the switches, results in crosstalk errors which multiply for each stage traveled. Pulse widening also affects the electro-optic interaction in the modulator[19,35,36]. Such errors degrade the overall system performance. Quantization occurs in the parallel bank of electronic ADCs making the power consumed large from both the quantizers and the numerous E/O switches. Finally, the data after the electronic quantizers must be time-interleaved, a significant signal processing task. These factors in combination would make this system rather impractical for Air Force applications.

Another successful approach in the PACT program was the high sample rate, low resolution architecture by HRL[37,38] mentioned in Chapter 2. They also developed a state-of-the-art electronic flash ADC operated at 10 GS/s with 4 bits of resolution. By multiplexing a 10 GHz mode-locked laser, HRL could potentially sample at 40 GS/s (20 GHz RF bandwidth signal) using a series of four time-interleaved electronic ADCs. They also developed a 3 bit 20 GS/s ADC which, multiplexed four times, could sample an 80 GS/s (40 GHz RF bandwidth) signal[30]. The electrical ADC was a flash architecture that relied on a comparator bank to provide the digitization using a thermometer code. The main advantage of this method was that it too could exploit the optical characteristics of low-jitter impulse sampling and clock distribution. A complete time multiplexed architecture can surpass the Walden Wall using photonic sampling methods, though the electronic quantizer performance specifications still resided on the Walden Wall. It is still unknown if InP-based electronic technology will work beyond the traditional wall and to what extent it can be scaled to obtain higher resolution. In that regard InP shows the most promise as compared with other traditional material systems.

A disadvantage of HRL's technique, as in MIT/LL's case, was that it depends highly on software processing to keep track of the timing of each pulse and to provide error correction. Ensuring accurate representation digitally is a difficult task. It was unknown if the optical multiplexer would add timing jitter to the optical pulses. Drawbacks of electronic flash architectures were mentioned in the previous section and also apply to this architecture since quantization occurs electronically. Having a separate sampling modulator for each channel adds to power consumption, and the photonic samplers were $LiNbO_3$ based devices, which are large area structures.

3.2 SNDP Contractual ADC Development

SNDP investigated two alternative architectures contractually with Professor Eric Donkor of the University of Connecticut (UConn) and Professor Zmuda from the University of Florida Graduate Engineering and Research Center (GERC). The UConn effort consisted of two back-to-back photodiodes arranged to act as a fast optoelectronic switch, which was essentially an

electrical open circuit taken to be the "off" state. When the diodes were stimulated with a laser pulse, the switch toggled to the "on" state. Thus, a train of mode-locked laser pulses applied to the diodes resulted in optical sampling of the RF input. The effort achieved sampling rates of 4 GS/S. The limitation in conversion speed was dictated by the photodiode which had a 3 dB bandwidth of 5 GHz. Details are found in the AFRL final technical report AFRL-SN-RS-TR-2003-271[39].

The GERC approach incorporated a recirculating optical loop to store a time-limited microwave signal so that it may be digitized by using a slower, conventional electronic ADC. Detailed analysis of the dynamic range and noise figure showed that under appropriate conditions the microwave signal degradation was sufficiently small so as to allow the digitization of a multi-gigahertz signal with a resolution greater than 10 effective bits. Experimental data demonstrated that a periodic extension of the input signal was sustained for well over one hundred periods, which suggests an electronic ADC speed-up factor of over 100. More explanation on this method is reported in AFRL-SN-RS-TR-2005-154[40].

3.3 SNDP In-House Photonic ADC Architecture

The basic block diagram of a generic photonic architecture shown in Figure 1-1 and explained in the Introduction applies to SNDP's architecture as well. In summary, the main components are an ultra-low noise mode-locked laser, an electro-optic modulator, and a quantizer. Each of the components was separately examined and will be discussed in depth throughout this document. A single channel was modeled and the results are reported. Both semiconductor and fiber lasers were investigated, as well as semiconductor based electro-absorption modulators. The quantizer component was based on semiconductor saturable absorbers. Near term goals for the in-house ADC program involved a single channel with a single bit resolution and 5 GHz bandwidth (10 GS/s sample rate).

As in MIT/LL and HRL approaches the in-house signals were sampled optically, avoiding distortion of the electronic signal. In contrast to the other photonic architectures that utilized electronic quantizers, SNDP's unique quantization scheme remained optical beyond the sampling stage. By using passive saturable absorbers (SAs) rather than electronically controlled switching elements and by avoiding the use of electronic ADCs, the power requirements could be made much lower than those in other schemes. Although the ultimate speed of the ADC system relies on the convergence speed of the SAs and the available speed of the electronic comparators, the MQWs themselves which comprise the SAs can operate at speeds up to 100 GS/s[41]. The recovery time of typical MQWs, which relies upon the conduction band to valence band recombination, can be tailored to be on the order of a few picoseconds using low temperature growth or ion implantation. The various components of this architecture were from the same material system, with the exception of the fiber laser, and could potentially be integrated on a common substrate thus providing significant advantage over the others cited. Finally, in addition to physical size and power consumption, a SA based system could be much less complex in practice than the other photonic conversion schemes.

3.3.1 Saturable Absorber Based Quantizer–Original Concept and Explanation

The original concept was awarded US Patent # 6,326910 as mentioned earlier. The schematic design of a SA architecture is shown in Figure 3-2 and is based on the ability to fabricate SAs with different values of saturation intensity (I_{sat}). The initial goal was to produce the transmittance curves to yield a family of switching thresholds that correspond to various quantizer levels. An optical modulated signal is sent in parallel to a 1 x N array of semiconductor saturable absorbers of varying thickness. The optical properties of the SA are tailored so that the absorbance can be scaled monotonically over the full range of values. The absorbance is scaled from a very large value for the first one in the array to a very low value for the Nth absorber in the array. If a sampled signal of very low intensity is incident upon all of the absorbers, the signal will be absorbed by the first absorber in the array and also by all of the others except for the Nth absorber in the array. This structure has the lowest absorbance and will pass the weakest signal. A detector following this absorber is then turned "on" by the transmitted optical signal. All of the other detectors remain "off" because the optical signal did not pass through its corresponding absorber. The corresponding electrical signal then corresponds to a certain predefined bit pattern. The "off" detectors have a value of '0' and the "on" detector has a value of '1'.

Similarly, if a signal with a slightly larger intensity is incident upon the series of saturable absorbers, the signal is still absorbed by the upper ones, but it is passed by the remaining absorbers to turn "on" the detectors as well. A corresponding bit pattern is once again formed. As in electronic flash ADC systems, the total number of absorbers or comparators required is equal to $2^N - 1$, where N is the number of bits of resolution. For example, a system operating with four bits of resolution would require 15 SAs.

Figure 3-2. Block diagram of saturable absorber photonic converter system.
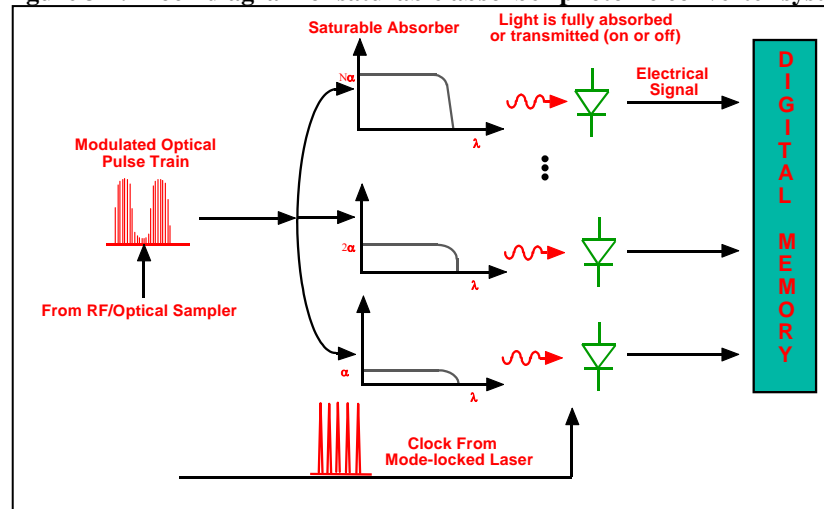
3.3.2 Modified Concept of Saturable Absorber Architecture

Alternatively, one could implement a parallel architecture by using a family of attenuation levels each followed by a SA with the same I_{sat} rather than a tailored I_{sat}; the result would again be a thermometer code. Because of the simplicity of the latter architecture from both design and fabrication viewpoints, it was selected for further examination by the ADC group in SNDP.

The quantization itself includes three steps: pre-conditioning of the optical pulse, conversion from optical to electrical domain, and comparison. The input to this subsystem is an optical pulse, and the output following an electronic comparator is either a 1 or a 0, corresponding to the level of the input pulse. This is illustrated in Figure 3-3.
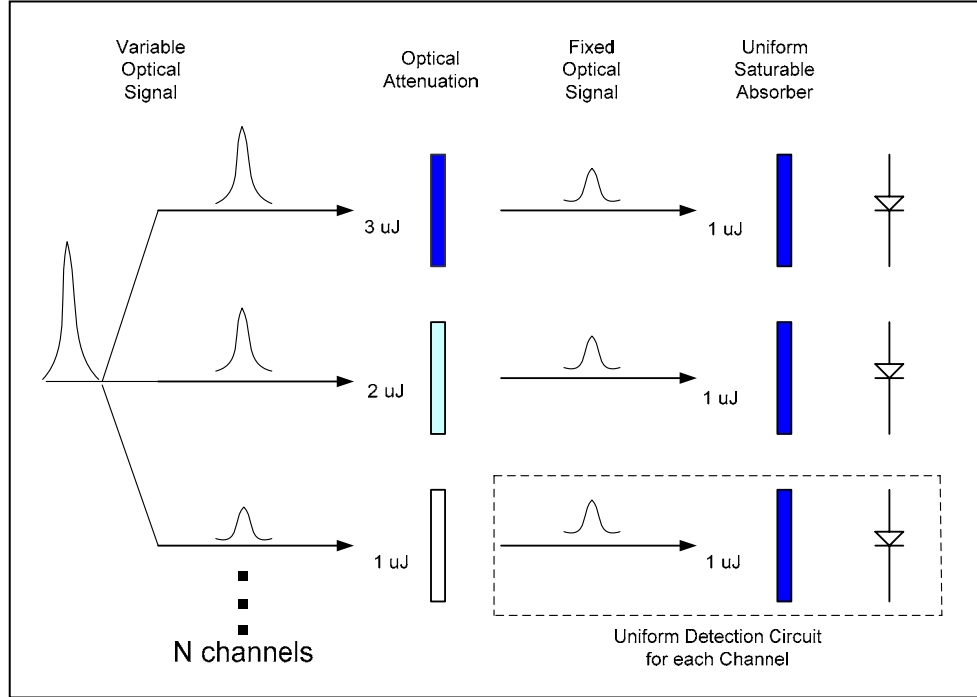
Figure 3-3. Photonic ADC architecture using a combination of variable linear attenuators and fixed nonlinear saturable absorbers.

For greater clarity the scheme illustrated in Figure 3.3 assumes an equal split of the modulated pulse train into N-channels. Each channel is pre-conditioned by appropriate attenuation, SA and opto-electronics (O/E). Depending on the exact layout i.e. large table top, small breadboard, or integrated chip system, the conditioning of the pulses, or equalization of energy in the channels, is done with neutral density filters, or fiber splitters, or custom waveguide splitters respectively. The SA and O/E scheme in each channel is the same. The use of a single reference voltage at the electronic comparators greatly simplifies the detection circuit and allows operation of all absorbers at a fixed design threshold. For example if all absorbers were designed to pass a 1 μJ pulse threshold, then a fixed opto-electronic circuit can be designed to detect a '1' for all pulses greater than 1 μJ and a '0' for pulses less than 1 μJ. The nonlinear properties of the absorber would allow a larger and more responsive dynamic range in the critical region than a simple linear optical detector. This nonlinear benefit is explained thoroughly in Section 3C4.

3.3.3 Saturable Absorber Characterization

The precise control of SA properties is essential to simultaneously achieve high resolution and multi-GHz operation of the photonic ADC. The nonlinear transmission and the recovery time or lifetime of the carriers within the semiconductor are of particular importance. The ability to accurately control the nonlinear transmission of the SA ultimately limits the number of achievable bits, and the ultimate sampling speed of the converter is limited by the

17

recovery time of the SA. InGaAs was chosen as the SA material because it has excellent optical properties near 1550 nm, which coincides with the minimum loss transmission window of optical fiber. Operation of the photonic ADC at this wavelength allows use of commercially available opto-electronic devices such as detectors and modulators. Both multiple quantum well (MQW) and bulk InGaAs, grown lattice matched on a semi-insulating InP substrate, were examined. The approach was first to demonstrate surface normal devices and then to move towards integrated waveguide designs. Professor Gary Wicks at the University of Rochester grew the SAs that were characterized by SNDP.

3.3.3.1 Intensity Characterization

Saturable absorbers were chosen because of the rapid turn-on of transmittance at properly designed I_{sat}. Transmission through the samples as a function of incident intensity is shown in Figure 3-4. The saturation intensity, I_{sat} is related to a model of intensity dependent absorption as:

$$\alpha(I_{in}) = \frac{\alpha_o}{1 + \frac{I_{in}}{I_{sat}}}$$

(3-2)

where α_o is the small signal or linear absorption coefficient and I_{in} is the incident intensity[42]. It is evident from this equation that I_{in} decreases along the length of the sample due to material absorption, and when $I_{in} = I_{sat}$, the absorption is decreased by one-half of its linear value. The change in intensity per unit length as a function of position in the sample, z is:

$$I(z + \partial z) = I(z)e^{-\alpha(z)\partial z},$$

(3-3)

and integration over the unit length results in

$$\ln(I_{out}) - \ln(I_{in}) + \frac{I_{out} - I_{in}}{I_{sat}} = -\alpha_o L.$$

(3-4)

Using the experimental data, we can solve equation 3-4 for I_{sat}. An example of typical measured data is shown if Figure 3-4.
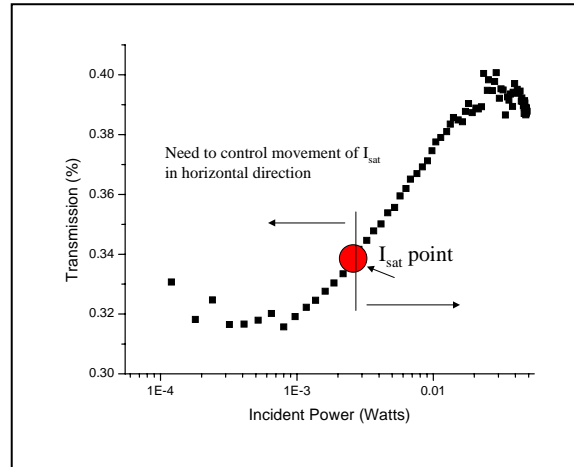
Figure 3-4. Illustration of the movement of absorber saturation point.

18

The data in Figure 3-5 illustrates an array of saturation curves over a wide range of input powers. It is important to note that these curves were generated for a single absorber measured as a function of incident wavelength, but they functionally represent the desired array of different 'turn on' saturation points.
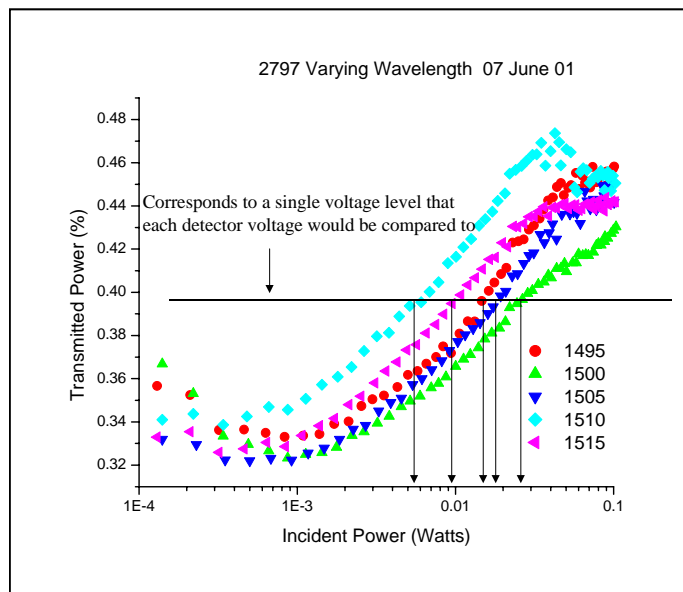
Figure 3-5. Illustrated array of saturation points corresponding to various input power levels.

The linear absorbance spectra of the SAs was measured in-house using a standard white light technique with a tungsten bulb as the white-light illumination source shown in Figure 3-6. A Newport RG 850 filter was used to pass only the near IR portion of the tungsten output, and the incident light was focused onto the sample with a 10X microscope objective. The transmitted light was collected and collimated also with a 10X microscope objective. Reflected light off of the surface of the sample passed back through a non-polarizing beam splitter onto a card placed a small distance away from the beam splitter. The focal position of the sample was adjusted until the best image was observed on the card. A 10 cm focal length lens was then used to focus the collimated light into the ARC 0.275 meter triple grating monochrometer, where a germanium detector collected the dispersed light. The detector was connected to a transimpedance amplifier followed by a SRS 510 lock-in amplifier, and a computer program controlled the monochrometer and collected the lock-in transmission data.
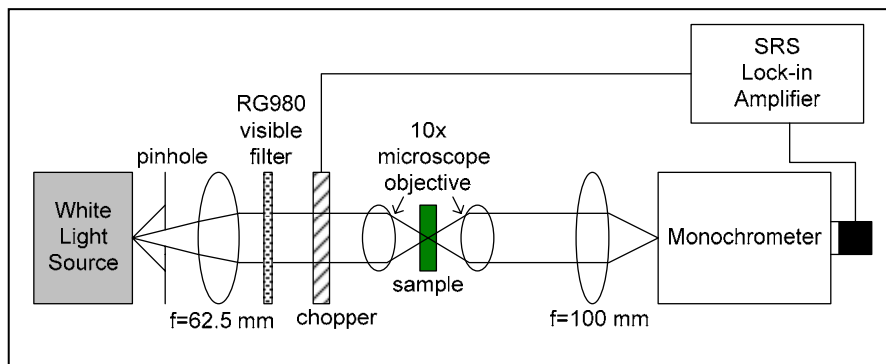
Figure 3-6. White-light linear absorption experimental setup.

19

The transmission measurements were performed using the following calibration procedure. First a baseline or source measurement was performed with no MQW sample present, and the transmission through the sample was recorded. The absorbance, αL of the quantum wells from Beer's law is given by equation 3-3, where the absorption coefficient α was found by dividing the absorbance by the total thickness of InGaAs layer. The absorbance spectra of two exemplary saturable absorbers are plotted in Figure 3-7.
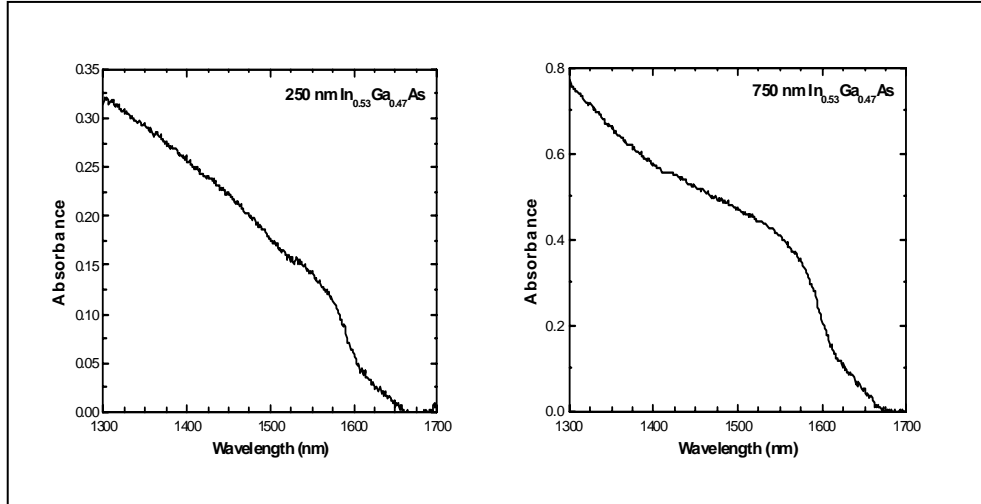
Figure 3-7. Linear absorbance spectra of 250 nm $In_{0.53}Ga_{0.47}As$ layer and 750 nm $In_{0.53}Ga_{0.47}As$ layer grown on InP.

The linear absorbance spectra of the 250 nm and the 750 nm samples were similar in shape as expected. The absorption coefficients of the samples were calculated; the 250 nm sample was 5880/cm and the 750 nm sample was 5506/cm. The values compared well with previously published values of 6800/cm and 6000/cm[43,44]. To verify the results the absorption spectrum was taken at multiple spots on each sample. Substantial variations were found particularly with the 250 nm sample. It is likely that strain present in certain portions of the 250 nm sample contributed to these fluctuations.

The nonlinear transmission experimental setup is shown in Figure 3-8, where the excitation source was a continuous-wave (cw) chromium-doped:YAG (Cr^{4+}:YAG) laser[45-48] operating at approximately 1500 nm. A computer controlled half-wave plate and two polarizers were used to vary the incident intensity on the sample, while a calibrated beam splitter determined the incident cw power. A microscope objective focused the light onto the sample with a spot size of approximately 42 μm^2, while a second microscope objective collected and collimated the transmitted light and sent it to a meter.
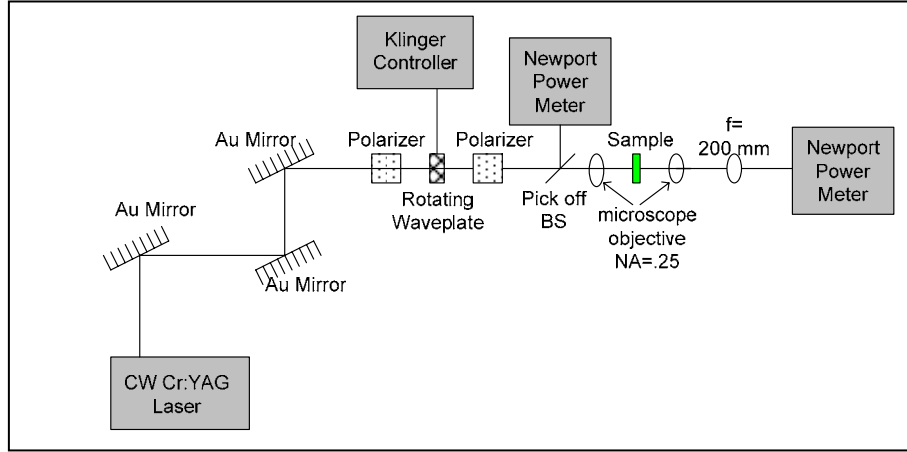
Figure 3-8. Experimental setup for nonlinear transmission measurements.

The results of the nonlinear transmission experiment for three different samples are shown in Figure 3-9. The values of the linear portion of the transmission were normalized to a value of 1 to facilitate comparison between the different samples. Samples 1437 and 2797 had similar saturation intensity values at approximately 10 mW/μm^2, while sample 2796 saturated at approximately 20 mW/ μm^2. Sample 2797 was a MQW sample grown at 400º C, while sample 2796 was 0.5 μm of bulk InGaAs also grown at 400º C. Sample 1437 was grown for use as a saturable absorber in a mode-locked external cavity semiconductor laser, and was included in this work for comparison purposes. It consisted of 100 periods of 115 Å $In_{0.53}Ga_{0.47}As$ wells and 100 Å $In_{0.52}Al_{0.48}As$ barriers.
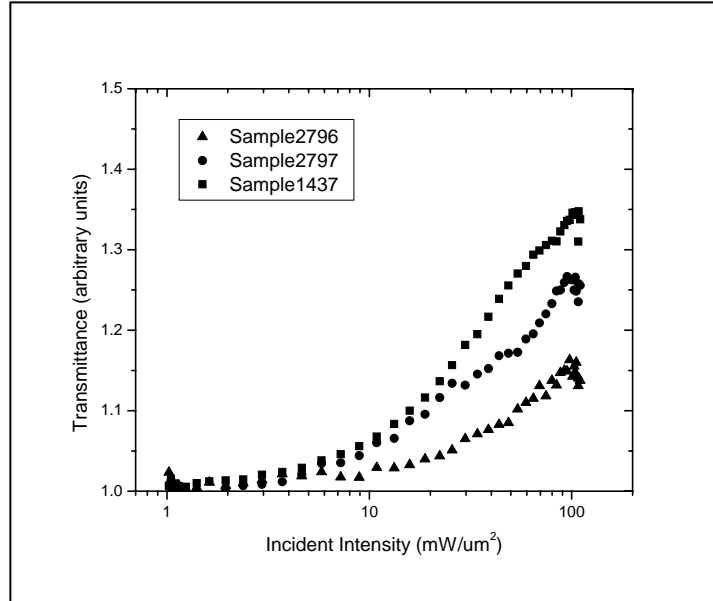
Figure 3-9. Nonlinear transmission measurements for samples of InGaAs grown lattice matched on InP substrates. For comparison purposes, the linear transmittance of all three samples was normalized to a value of one.

Figure 3-9 also illustrates that sample 1437, the thickest (2.15 μm) of the three shown here, had the largest change in value from the linear absorbance region to the point where the transmission saturates. It was desirable to have the largest possible transmission change when

the input intensity saturated the InGaAs. The incident intensity required to saturate these structures corresponded to an average power on the order of tens of milliwatts, which was well within the normal range of compact mode-locked fiber and semiconductor lasers.

Further growth runs were carried out to examine the relationship between thickness and strain and its overall effect on saturation intensity. Those results indicated that steeper nonlinear behavior was achieved, but the various bandgap engineering techniques still did not provide sufficient change in transmission, as is shown in the detailed discussion that follows.

Figure 3-10 compares the performance between pulsed laser operation and CW operation and showed that the pulsed performance reached nonlinear operation significantly sooner. This may have been related to greater heat build up in a CW case, and since an ADC uses pulsed operation, this behavior was favorable.
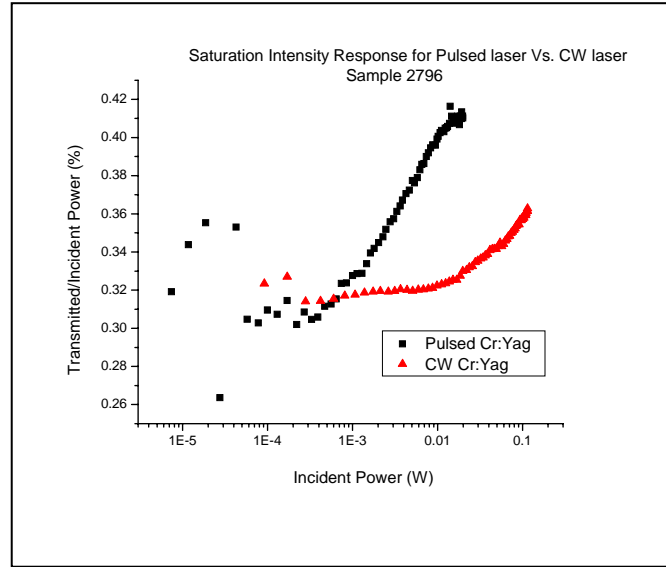
Figure 3-10. Performance of pulsed laser operation and CW operation.

3.3.3.2 Lifetime Characterization

Early investigations[41] showed that use of tailored QW structures with ion implantation generated lifetimes on the order of 26 ps were achieved, which translated to optical sampling speeds approaching 50 GHz (100 GS/s). Ion implantation and low temperature growth were further investigated in this effort and both had similar behaviors. Both techniques introduce non-radiative recombination centers within the bandgap of the InGaAs, which effectively shorten the lifetimes of the carriers[49,50]. The empty trap first captures the electron and subsequently this filled trap captures the hole effectively destroying the electron-hole pair. The process is much faster than the natural band to band recombination resulting from an electron's decay from conduction to valance band

Initial quantum well samples consisted of a 1000Å $In_{0.52}Al_{0.48}As$ buffer layer grown on the InP substrate followed by 50 periods of 100 Å $In_{0.53}Ga_{0.47}As$ wells and 100 Å $In_{0.52}Al_{0.48}As$ barriers and completed with a 100 Å $In_{0.53}Ga_{0.47}As$ cap layer. MQW saturable absorbers were grown at 150º C, 300º C and 400º C. The bulk samples consisted of $In_{0.53}Ga_{0.47}As$ grown directly on the InP substrate with layer thickness set at 0.5 µm, 1.0 µm, 1.25 µm and 1.5 µm, and growth temperature varied from 280º C to 400º C. A sampling of absorber results was selected in this report from to the large amount of data taken on many different types of samples.

The recovery times of the saturable absorbers were measured with standard pump/probe spectroscopic techniques[51]. In this type of experiment, electron-hole pairs are created by the absorption of an intense pump pulse, and the corresponding transmission change is monitored in time by a weaker probe pulse temporally delayed with respect to the pump pulse. The resulting transmission change at different points in time allowed temporal monitoring of the carrier lifetimes in the semiconductors.

The absorption coefficient, α, of the quantum wells in the SA after excitation is given as a function of the probe delay, t, by

$$\alpha(t) = \alpha_o + \Delta\alpha e^{-\frac{t}{\tau}} \tag{3-5}$$

where α_o is the linear absorption coefficient, $\Delta\alpha$ is the change in absorption induced by the pump pulse, and τ is carrier recombination time or lifetime. The recombination time of the absorption recovery in Eq. 1 is related to the transmission data by

$$S(t) = A \int_{-\infty}^{\infty} I(t'-t) e^{\alpha(t')d} dt' \tag{3-6}$$

where S(t) is the energy of the transmitted probe versus delay, A is the area of the probe beam, I is the intensity of the transmitted signal and d is the thickness of the saturable absorber. Using the energy density, $W = \int I dt$, of the probe beam, Eq. 3-6 can be rewritten as

$$S(t) \approx AWe^{\alpha(t)d} \approx AW[1 + \alpha(t)d] \tag{3-7}$$

where it was assumed that the temporal change in the absorption coefficient was small compared to the pulse duration. Finally, substituting Eq. 3-5 into Eq. 3-7 gives

$$S(t) = AW\left[1 + \alpha_o d + \Delta\alpha d e^{-\frac{t}{\tau}}\right] \approx S' + AW\Delta\alpha d e^{-\frac{t}{\tau}} \tag{3-8}$$

where S' is the probe transmission before the arrival of the pump pulse. Therefore, the exponential decay time of the change in the probe transmission indicated, by direct measurement of carrier recombination time, that the speed is sufficient for ADC application.

The degenerate, co-linear pump/probe in-house experimental setup to measure the carrier dynamics in the saturable absorbers is shown in Figure 3-11. The Cr^{4+}:YAG laser was operated in a mode-locked state producing 130 fs pulses at 1500 nm. The pump and probe beams were separated into orthogonal polarizations by a 50/50 polarizing beam splitter. The probe beam was delayed with respect to the pump beam using a linear stage controlled with a stepper motor with 10 cm travel. The beams were recombined co-linearly using a non-polarizing beam splitter and focused onto the sample with 10X microscope objective, and the transmitted light was collected and collimated with another 10X microscope objective. A Glan-Thompson polarizer was used to reject the pump beam and ensure that only the transmitted probe beam reached the detector. The probe beam was focused onto a germanium detector using a 5 cm focal length lens. The detector was connected to a transimpedance amplifier and in turn to a lock-in amplifier. A mirror flipper

and an IR camera positioned well away from the experiment were used to ensure that the pump and probe beams were spatially overlapped when incident on the sample. The data was collected by a LabVIEW program which also controlled the movement of the linear stage. An optical chopper provided the reference signal to the lock-in amplifier and cut the pump and probe beams at different frequencies. This allowed a differential lock-in technique to be used so that only the pump induced change in the probe transmission was detected. The ratio of the pump beam to the probe beam was set at a minimum value of 50:1, and the power of the probe beam was minimized to ensure that it did not introduce nonlinearities in the sample. The laser power was also monitored to ensure that there was no power drift during the experiment.
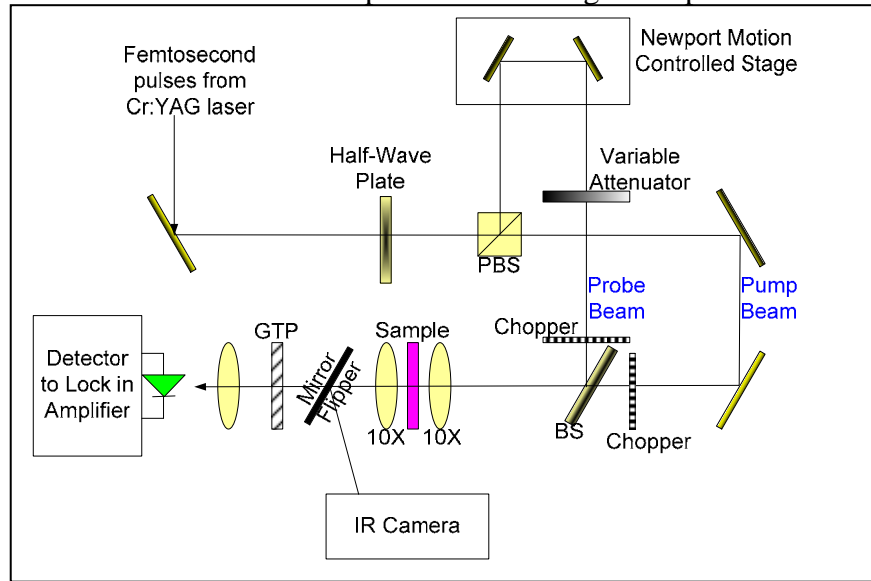
Figure 3-11. Experimental setup for pump/probe measurement to determine the recovery time of the saturable absorbers.

The pump/probe experimental results for two saturable absorbers are shown in Figure 3-12.   Sample 2750 was a MQW structure grown at 300º C and was found to have an exponential decay lifetime of 18 ps.   This saturable absorber fully recovered in approximately 75 ps indicating that this particular device could be used at sampling speeds up to 1/75 ps, or 13 GHz. Sample 2797 was shown to have a much longer carrier lifetime of 204 ps; though this was also a MQW structure, it was grown at a higher temperature of 400º C. These results clearly indicate that lower growth temperatures had a profound effect on reducing the carrier lifetimes within the saturable absorbers. The trend in Figure 3-10 was consistent in all of the saturable absorbers tested with the fastest lifetime observed at approximately 7 ps.
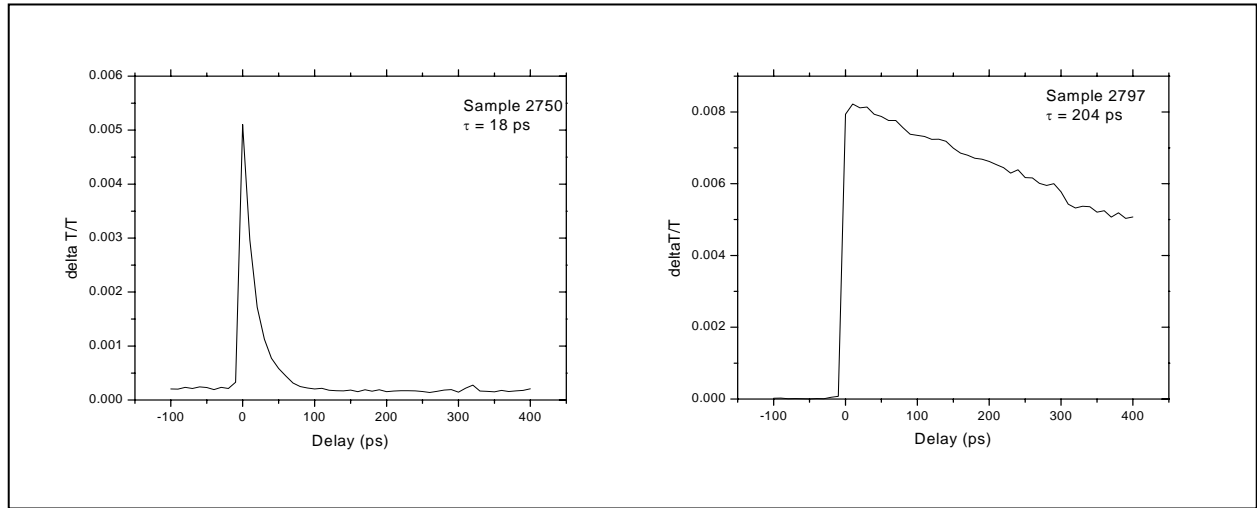
Figure 3-12. Experimental pump/probe results for sample 2750 with 18 ps lifetime and sample 2797 with 204 ps lifetime.

In summary, the optical properties of primary concern were the nonlinear transmission and the recovery or lifetime of the carriers within the semiconductor SAs. A series of both MQW and bulk InGaAs grown lattice matched to InP were examined. It was determined that the largest transmission change from the linear to the nonlinear regime corresponded to the thickest saturable absorber. As expected the SAs grown at the lowest temperatures exhibited the fastest recovery. The recovery times that were measured would enable multi-GHz operation of the photonic ADC; however, there remained some doubt after exhaustive experiments that the absorbers could provide sufficient nonlinearity to benefit a system of this nature. It was decided that calculations based on a simple model would clarify this issue.

3.3.4 Initial Single Channel Model

To review, the optical pulse is first preconditioned through a stage of linear attenuation, which produces a linear P_{out} vs. P_{in} transfer characteristic as shown in Figure 3-13. The purpose of attenuation is to ensure that the optical power incident on the SA in the next stage is appropriate to drive it at the intended operating point. This attenuation can be implemented in different ways; for instance through the splitting loss designed into the optical pulse fan-out, or by use of a linear absorber, or a combination of both. The optical power is then passed through a non-linear element, the SA, after which it is incident upon a photodetector (PD) which produces a current in response to the light. The current is passed through a transimpedance amplifier (TIA) to translate the current signal to a voltage signal. This voltage is finally compared to a reference so that the output of the comparator corresponds to either a 1 or a 0 in the electrical domain.

25
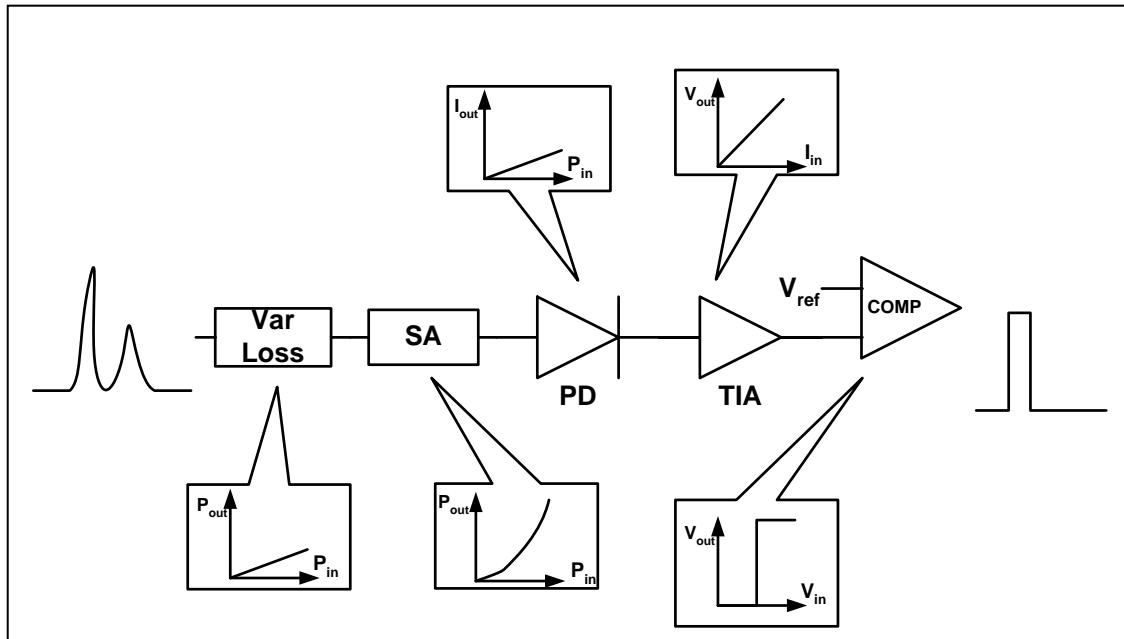
Figure 3-13. Single channel quantizer architecture model with callouts illustrating typical transfer characteristics for the associated component.

Before the input pulse is incident on the photodetector, it must be optically pre-processed to ensure that its power level lies within acceptable specifications. This preconditioning is achieved by judicious use of amplification and attenuation. The power budget for a channel is shown in Figure 3-14: the saturable absorber, photodiode and comparator in combination act as a discriminator, the slope of SA transfer function constrains error sensitivity, and the dynamic range is determined by the properly attenuated input power level.
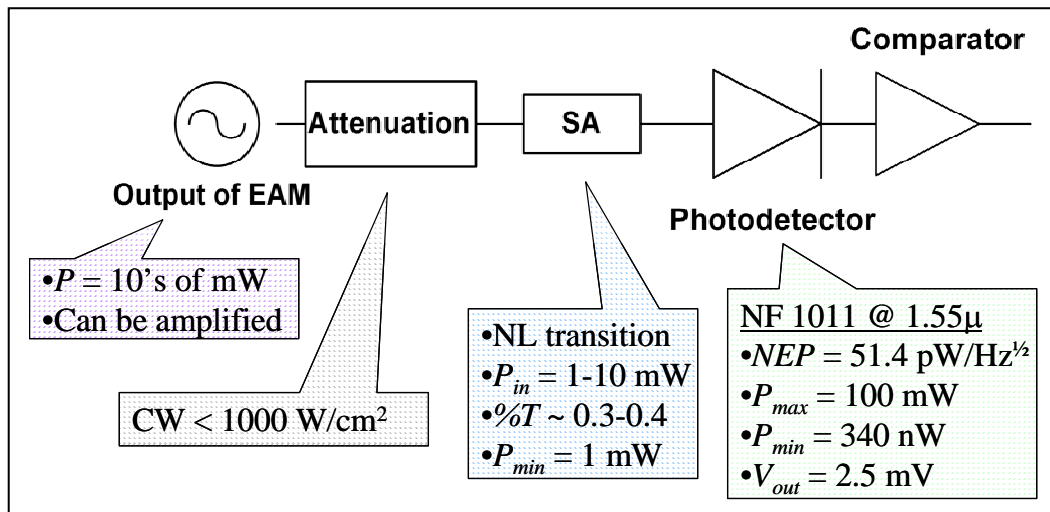
Figure 3-14. Power budget for a single channel.

To understand the role of the non-linear SA element, it is necessary to consider it in conjunction with the photodetector, TIA and comparator in the final stage. It is the combined

action of all the elements which implements the switching necessary to convert the input signal level to a 1 or 0 for the digitization. The comparator acts as an electrical switch, the photodetector converts photons to the electrical signals used in the comparator, and together they determine the threshold optical output power from the SA to switch the state of the comparator. This in turn determines the input optical power threshold for the SA corresponding to the digitization of the pulse.

Thus the SA is not the component that performs the switching in the system, but rather the device that provides the necessary transfer characteristic for power exiting the optical stage and entering the photodetector. In principle it is possible to use a linear transfer characteristic (in conjunction with the comparator), either through linear attenuation or through the response function of the photodetector itself. A SA is not only desirable but essential to control the power levels incident on the backend detection system and, thereby, provide a higher bit error rate than a simple linear absorber. Thus the key feature of the SA transfer curve is not the so-called "non-linearity" of the device, but the steepness of the curve (referred to as the slope efficiency) at the operating point. This answers a natural question: "Why use a SA at all and not a simple linear absorber?" The explanation is provided by the on-off contrast ratio of the device and is defined as the transmittance of the device in the "1" state divided by the transmittance in the "0" state, though its significance may not be immediately apparent. The ultimate limit to the performance is determined by the steepness of the slope, and the fact is that no existing linear absorber generates sufficiently large slope efficiency to achieve the on-off sensitivity needed to avoid comparator ambiguity.

To understand some issues pertaining to the flash ADC design, a preliminary transfer characteristic was modeled in MathCAD. The non-linearity of the SA is characterized by a change in percent transmission as a function of input optical power. The optical transfer characteristics of the SA are obtained by transforming the percent transmission curves. A comparison of linear and nonlinear absorbers is shown in Figures 3-15 and 3-16.
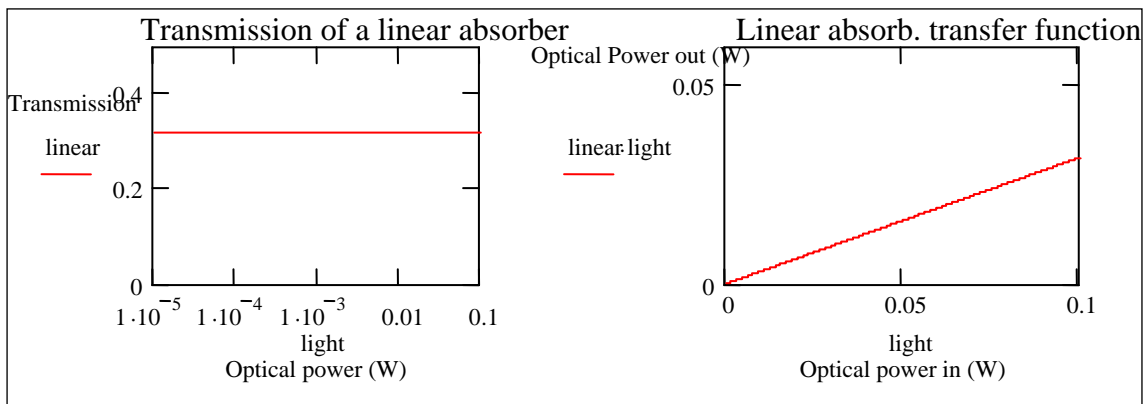
Figure 3-15. Transfer characteristic of a linear absorber. A linear absorber (32% transmission in this case) has as an optical transfer function a line with a slope 0.32.
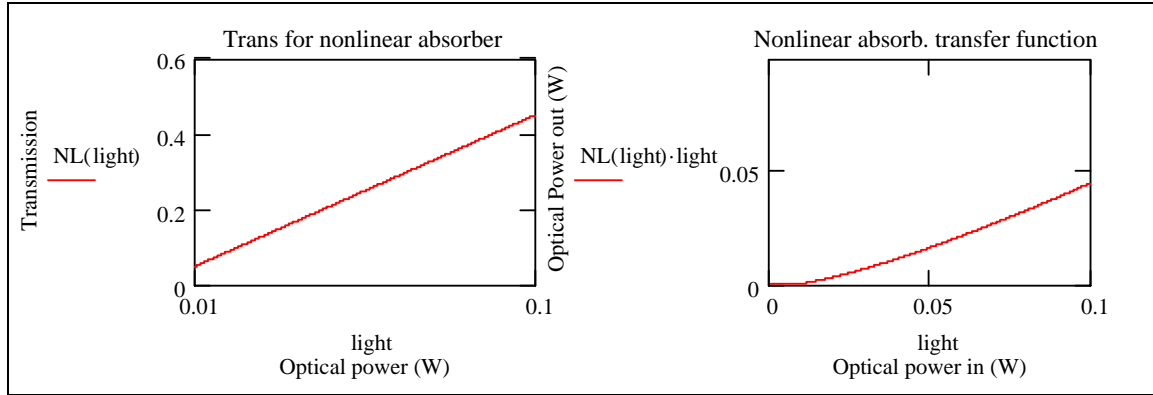
Figure 3-16. A hypothetical nonlinear absorber with a transmission that changes with optical input power. The transmission curve is a line on a semi-log graph with non-zero slope. This produces an optical transfer function that has an x*log(x) characteristic.

Models based on actual measurements of the transmission of our saturable absorber samples are represented in Figure 3-17. The values of transmission have been chosen to highlight the "knee" in optical transfer function that occurs at the transition from the linear to the nonlinear region. Measurements of the transmission of actual samples have the same shape, although the values of transmission in the linear region and the slope in the nonlinear region differ. The nonlinearity of the transfer function is the basis for the architecture.

The nonlinearity of the actual SAs is a separate issue, which was also explored. The degree of nonlinearity in the optical transfer function is governed by the value of transmission in the first linear region and the slope in the nonlinear region of the transmission curves.
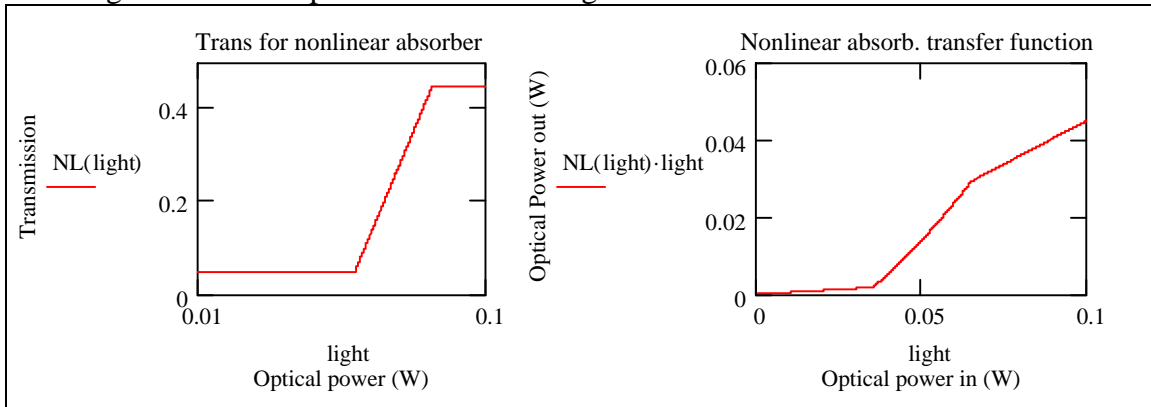
Figure 3-17. Model of transmission for a saturable absorber. The optical transfer function shows two linear regions separated by a region of x*log(x) behavior. The transition from linear to x*log(x) produces a knee in the curve. The sharpness of the knee is dependent on the value of transmission in the linear region, and the slope (on the transmission graph) in the nonlinear region.

The performance of the transfer characteristic for a saturable absorber has been quantified in terms of the Bit Error Rate (BER) in the literature[52]. In an effort to provide quantitative evaluation of the superior performance of SAs over linear counterparts, we present a zeroeth-order comparison of the BER between the two types of devices.

As described by Hirano *etal*,[52] the Q factor of the detector is defined and related to the BER, with:

$$Q = \frac{n_1^{elec} - n_0^{elec}}{\sigma_1^{elec} + \sigma_0^{elec}} \qquad (3\text{-}10)$$

$$BER = \frac{1}{2}\text{erfc}\left(\frac{Q}{\sqrt{2}}\right) \qquad (3\text{-}11)$$

where n^{elec} and σ^{elec} are the number of and variance in the number of photoelectrons, respectively, and the subscripts refer to the "1" and "0" states. Assuming a quantum efficiency of unity for the photodetector, we can directly relate the number and variance of the photoelectrons to the number of incident photons. Assuming Poisson statistics, and ignoring external effects, we have:

$$Q = \sqrt{n_1}\left(\frac{1-R}{1+\sqrt{R}}\right), \qquad (3\text{-}12)$$

where R is called the extinction ratio, and is defined as the transmittance of the device in the "0" state divided by the transmittance in the "1" state (this quantity is essentially the inverse of what we have heretofore referred to as the contrast ratio). B is the bandwidth of the photodetector and n_1 is the mean number of photons detected in the "1" state. For instance, the value of R from data previously presented is approximately $0.3/0.5 = 0.6$. In comparison, R for a linear absorber would be close to unity, thereby strongly suppressing Q.

The BER was calculated for several scenarios, and is shown in Table 3-1. For these estimates, the following assumptions were made: absorber input power = 1 dBm, detector bandwidth = 5 GHz, and pulse duration = 12 ps. It should be emphasized that these numbers are not to be taken as design specifications; their importance lies primarily in the direct comparison they allow between the effect of linear and non-linear components. When all effects are taken into consideration and more sophisticated calculations are performed, it can be shown that BERs on the order of 10^{-15} are achievable using SAs[52]. The important point cannot be over-emphasized: ***small changes in R have a large effect on the BER, and only non-linear behavior can produce the required values of R.*** The smaller the value of R, the better; linear responses simply do not change rapidly enough to yield a small enough R.

Table 3- 1: Comparison of BER estimates for various scenarios.

	R	Q	BER
Linear	0.999	6.64E-04	0.5
Current Sample	0.6	7.12	1.00E-13
Nonlinear	0.1	21.6	1.00E-16
Hirano, *ibid*.	0.1	15	1.00E-15

However, in order to realize a quantizer of this nature, it became clear that there must be a "sample and hold" circuit after the photodiode to grab the photodiode output, make a comparator decision to convert it to a "1" or a "0", hold it for the arrival of the next electrical clock pulse, and then reset it before the next optical pulse. If the saturable absorber transfer functions were "ideal" (0 to 100% transmission over a narrow range of input optical power), then the optics would augment this process by adding effective "gain" to the electrical comparator function. The larger the gain, the lower the effective aperture uncertainty, as it reduces the likelihood that the comparator will not make the proper decision (1 vs. 0). However,

if the transfer functions are relatively "soft" as shown in the plots with a transmission change from ~ 30% to ~ 40% over a wide range of input power; then the input optics may actually degrade the performance by "reducing" the comparator gain below what could have been achieved by the electrical ADC alone.

Given this analysis, great emphasis was placed on increasing the contrast ratio (maximum transmission/minimum transmission) of the SAs. It is clear that the SAs fabricated up to this point did not provide a sufficiently steep slope. However, absorbers in an etalon configuration exhibiting the required bistability were developed by other groups[53,54]. Waveguide etalons[54] are also compatible with the single chip integration, underlying SNDP's approach to a SA based ADC architecture.

3.3.5 Bistable Etalons

3.3.5.1 Growth and Experimental Testing

Since the University of Rochester did not have the capability to fabricate the required mirror structures on the SAs, the ADC in-house team contracted Sarnoff Corporation to grow the bistable etalon structures as well as model the structure and device performance. Simultaneously, SNDP examined bistable etalon theory[55] for an in-depth understanding of the device physics.

The devices consisted of planar multi-quantum well saturable absorbers an etalon defined by editorially grown reflective distributed Bragg reflector mirrors. A detailed approach is described in the final report, AFRL-SN-RS-TR-2003-210[56], submitted by Sarnoff. In short, nonlinear transmission was observed, but bistability could not be obtained. Detailed modeling showed that thermal mechanisms override the quantum well nonlinearity, even at sub-nanosecond time scales, due to the very small size of the etalon (several microns). The sequential procedure used for modeling the output versus input of the BRET device is given in TABLE 3-2[56].

Table 3-2: Sarnoff's Modeling Procedure for BRET Device[56]

1- Calculate $\alpha(\lambda,N)$
2- Calculate $\alpha(\lambda,I_c)$ using iterative methods (I_c is the optical intensity inside the cavity)
3- Calculate $\Delta n(\lambda,I_c)$ using Kramers-Kronig
4- Calculate cavity internal phase change $\Delta\phi=\Delta nk_0 L$
5- Calculate input optical intensity $I_{IN}=C(1+F\sin(\phi)^2)I_c$ where:
$C=\alpha L(1-R_e)^2/[(1-R_F)(1+R_B e^{-\alpha L})(1-e^{-\alpha L})]$
$F=4R_e/(1-R_e)^2$
$R_e=(R_F R_B)^{0.5}e^{-\alpha L}$
L= cavity length
R_B= back mirror reflectivity
R_F= front mirror reflectivity
6- Calculate output optical intensity $I_{out}=I_c\alpha L(1-R_B)e^{-\alpha L}/[(1- e^{-\alpha L})(1+R_B e^{-\alpha L})]$
7- Plot output optical intensity vs. input optical intensity

L=0.249 μm

L=0.250 μm

L=0.251 μm
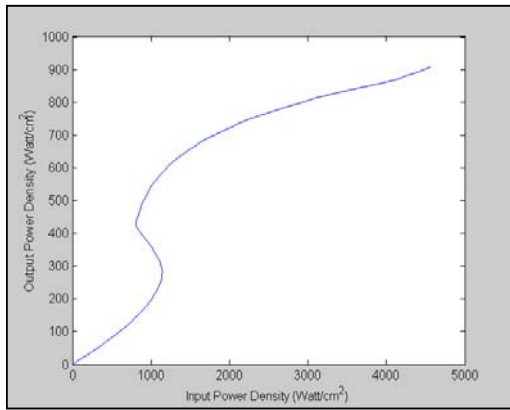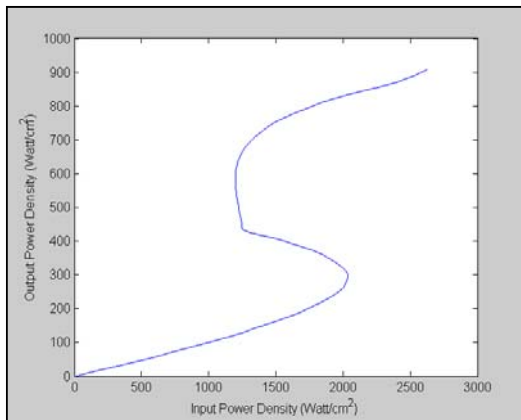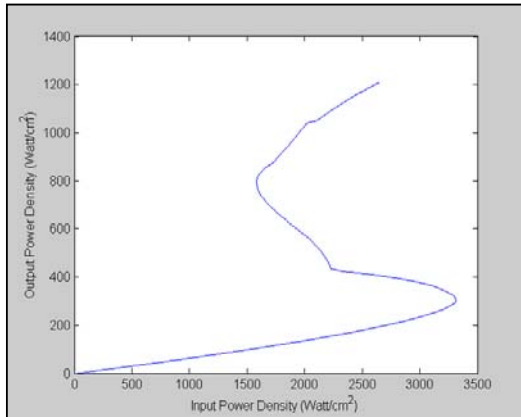
R_B=98%, R_F=95%, λ=1.575 μm, τ=2 ns

Figure 3-18. Results of Sarnoff's modeling showing bistability[56].

Sarnoff's modeling showed that with the correct parameters set for the front and back mirrors, and the cavity length, bistability should be obtainable in a particular wavelength range. The modeled results of changing the thickness are shown in Figure 3-18, which illustrates the high sensitivity of the bistability versus cavity length. A few nanometer variation in the thickness has a very large influence on the bistability. The modeled bistability characteristics were much less sensitive to wavelength and front mirror reflectivity as shown in their report[56].

Two iterations for the fabrication of etalon structures were performed. The first with a BRET structure consisted of a front mirror (epitaxially grown DBR) reflectivity of 95%, a back mirror (dielectric stack) reflectivity of 98% and a cavity length of 360 nm. A schematic of the design is shown in Figure 3-19. The samples were backside polished and anti-reflection coated, while the front side had a dielectric mirror deposited. The dielectric DBR consisted of 4 pairs of Si/Al_2O_3 to give a peak reflectivity of ~ 98%. The devices showed some non-linear behavior but no bistability, as was confirmed in tests at both Sarnoff and AFRL. It was concluded that the material band-gap was blue shifted possibly preventing bistability. In the second iteration three structures were grown, and the wavelength of the active region was shifted to longer wavelengths for all structures. Two of those contained InGaAs/InAlAs active regions similar to the first iteration but with a longer etalon resonance peak. One structure was grown using Al-free InGaAs/InP for the active region to eliminate possible problem with the Al containing layers.
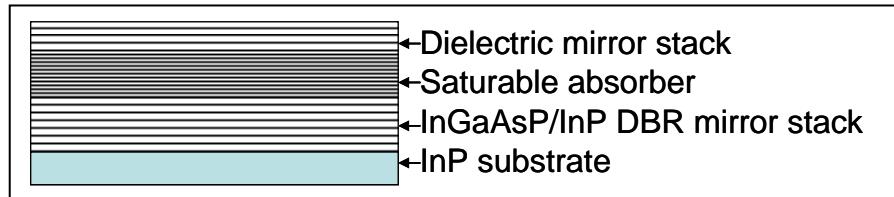
Figure 3-19. Structure of BRET device.

One half of each wafer from the second iteration was coated at Sarnoff with a dielectric mirror comprised of three pairs of Al_2O_3 (255.76 nm) and Si (111.07 nm) with a measured reflectivity of 99.3% at 1550 nm. These half wafers were cleaved into quarters and one quarter of each was sent to AFRL, so testing could be done at both Sarnoff and AFRL. A second half of each wafer from this iteration was coated externally at Rugate Technologies, Inc. with an 8 pair dielectric stack designed for 99% reflectivity at 1550 nm.

AFRL's test results, shown in Figure 3-20, on samples from the second iteration indicated that the transmission varied with location on the sample indicating that excessive stress and strain remained.
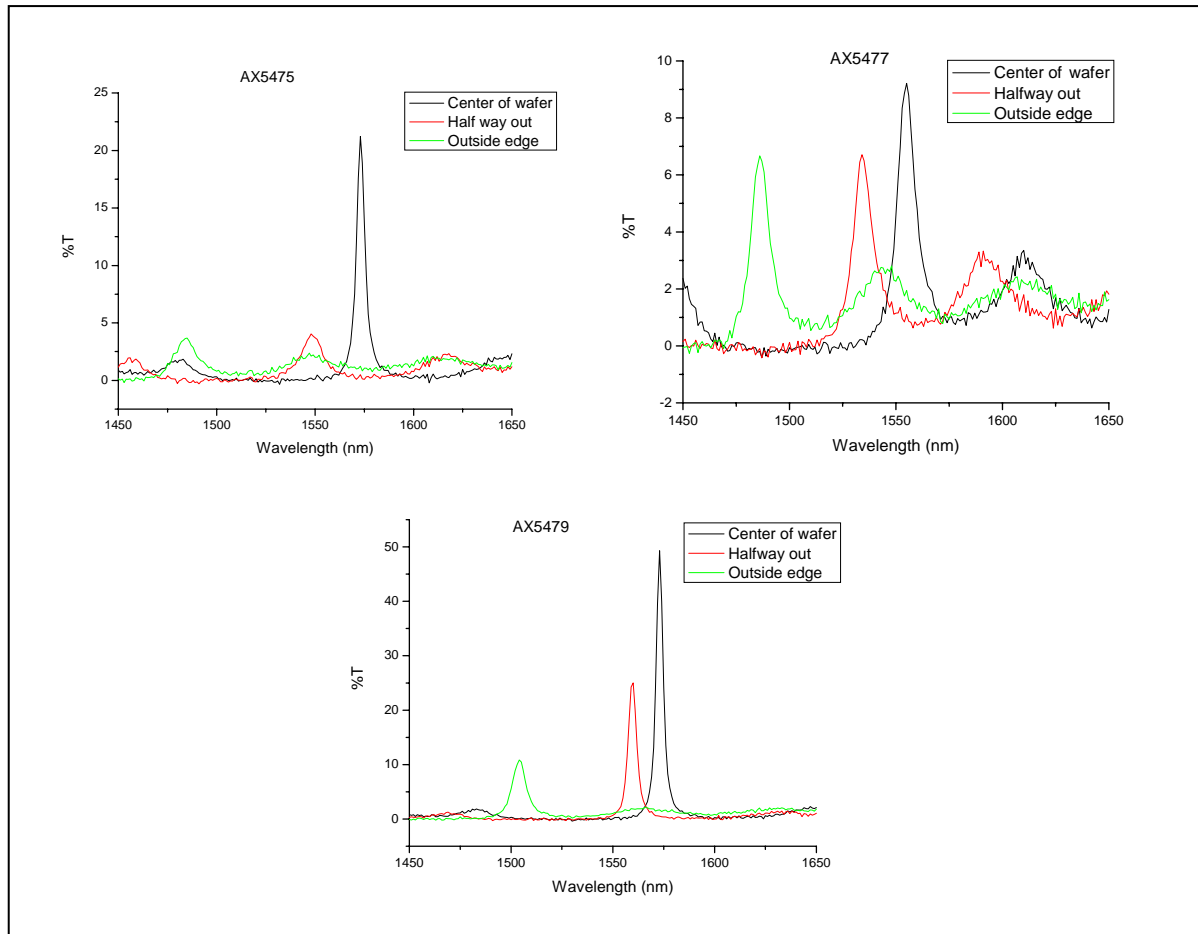
Figure 3-20. SNDP tested devices. Transmission still varied with location on the sample indicating that stress and strain still existed.

Sarnoff measured enhanced nonlinearity with the second iteration, and Figure 3-21 is representative of the best result. AFRL did not witness nonlinearity to the same degree in a

typical measurement shown in Figure 3-22. To eliminate the possibility that some differences may be due to different laboratory setups or that the wavelength in the AFRL plot may not have been on resonance, angle tuning and wavelength scanning were performed.
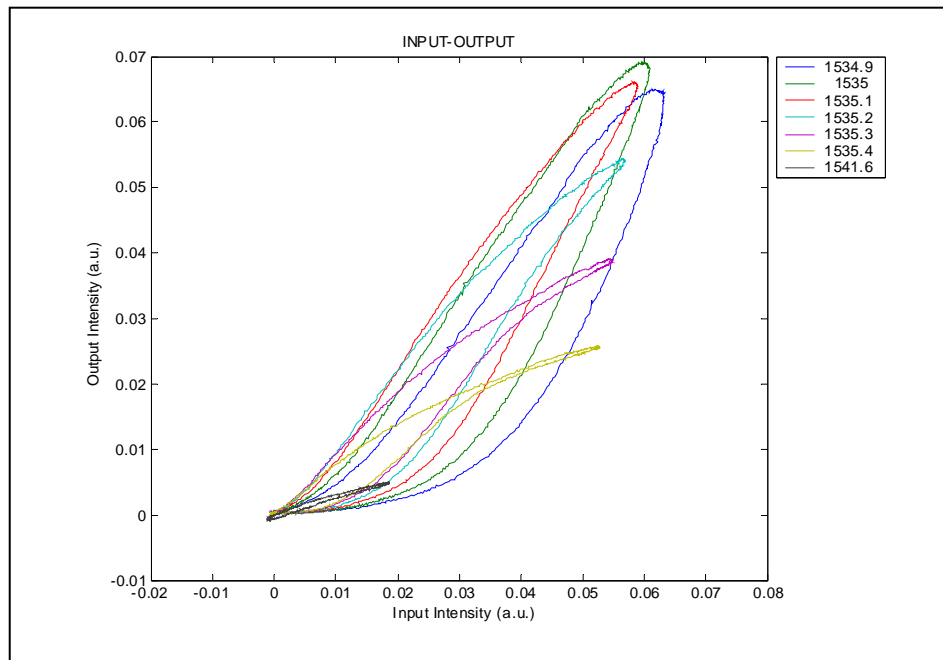
Figure 3-21. Sarnoff measured nonlinearity for sample AX5475.
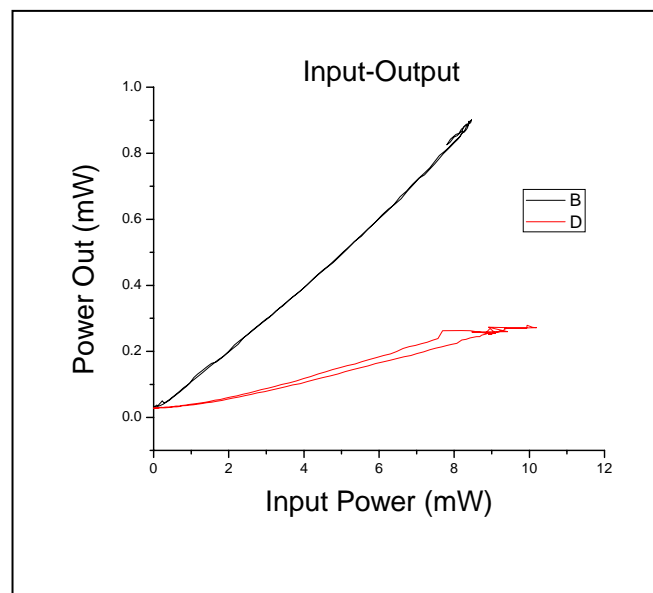
Figure 3-22. AFRL measured nonlinearity for sample AX5475.

AFRL's test results did not exhibit the nonlinear enhancement measured by Sarnoff. It is possible that "ideal" locations on the wafer were required, but a thorough scan of sample positions did not eliminate the experimental discrepancy. Regardless, bistability was not confirmed in either case.

The experimental setup to characterize etalons is shown in Figure 3-23. Zemax was used to model various spot sizes incident on the sample to determine if local heating effects still prevented bi-stable behavior. The pump probe experiment made use of a 980 nm laser to excite the material and a weak tunable laser near 1550 nm to probe the device.
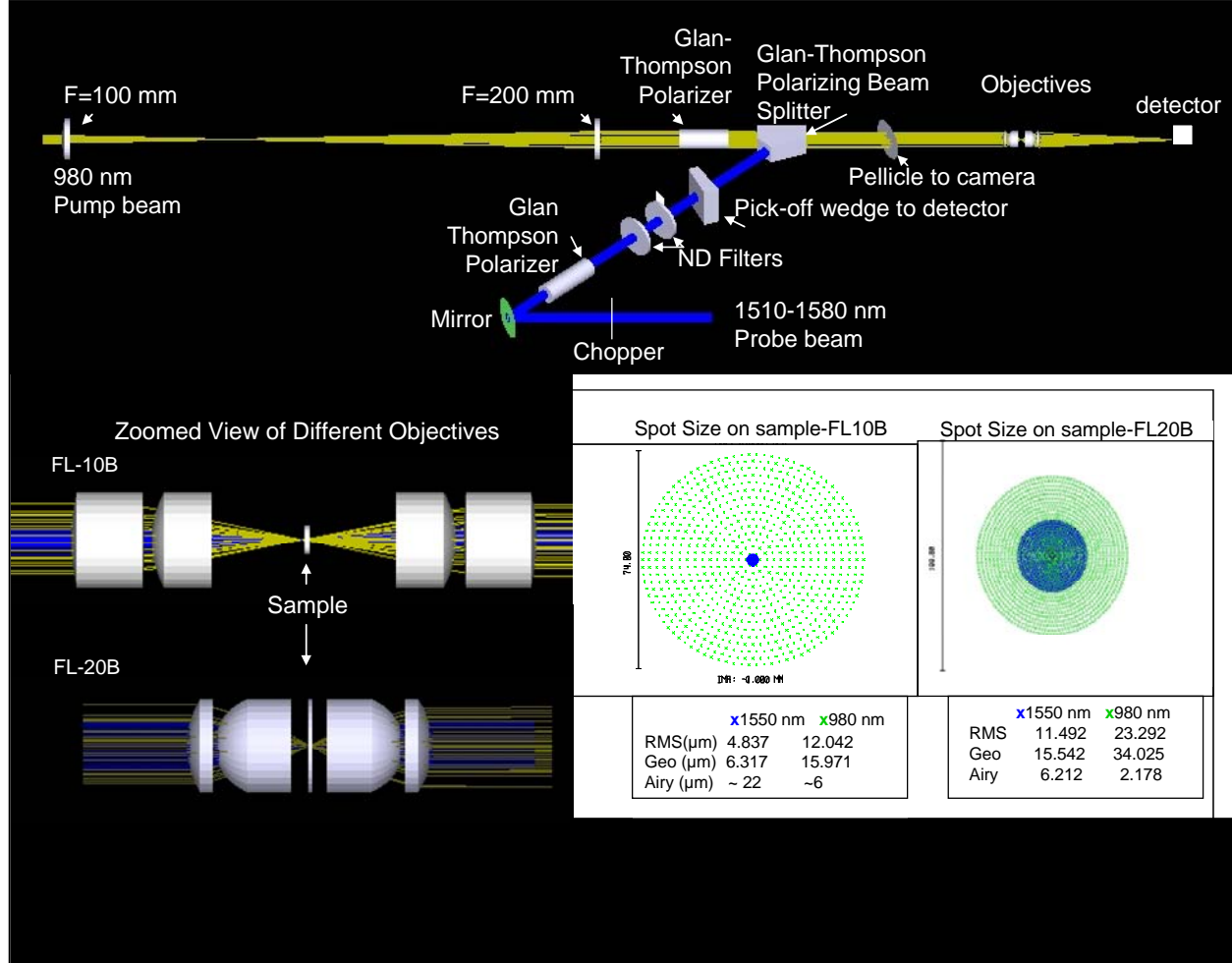
Figure 3-23. Experimental setup to characterize etalons.

3.3.5.2 Explanation of Problems and Proposed Solutions

It was the consensus of those involved that the main obstacle to bistability in the BRET structure was indeed the heating effect. This is an extremely important issue in bistable devices, since the change of index resulting from the change in temperature competes with the change of index resulting from the carrier generation. Lower optical threshold power in the ridge waveguide geometry combined with much lower heat resistance make this geometry less susceptible to heating. The heating problem can be reduced only to a certain extent by decreasing optical pulse width and duty cycle, because the rate of temperature change with time is independent of both of those, and varies only with the material's heat capacitance and the optical power. For example, as reported by Sarnoff[56], a two-dimensional thermal modeling of a vertical geometry with beam spot size of 5 μm showed that an input power of only 1 mW ($\sim 4 kW/cm^2$) gave a change of temperature versus time of $\Delta T/\Delta t \sim 7.45 \times 10^7$ K/sec. This means that the

temperature will rise approximately 7°C in only 100 ns. Since $\Delta n/\Delta T$ in the InGaAs quantum wells is approximately 5×10^{-4} 1/K, the calculated change of index of $\sim 3.5 \times 10^{-3}$ is comparable to the carrier induced change of index.

A related problem is posed by the uniformity of the quantum well thickness composition[56]. The thickness of the active layer should be limited to less than one micron in an etalon configuration, whereas in a vertical cavity resonator such thickness leads to a free spectral range of more than 400 nm. This places a stringent requirement on the cavity's thickness accuracy, since only one resonant frequency is close enough to the band edge. Simulations showed that bistability required a resonant detuning with accuracy of ~ 5 nm, which indicates ~ 5 nm accuracy in thickness ($\sim 0.5\%$), while typical accuracy of the MOCVD growth is only a few percent. It was assumed in the above that the bandgap of the active layer was known, but in actual practice the bandgap of the active layer changes by about ± 5 nm in successive growth runs, so this variation reduced the chance of a successful device even more. A ridge waveguide configuration would alleviate these problems by providing a free spectral range in the order of a few nanometers, so that there is always a resonance wavelength within the ~ 5 nm detuning range.

Lowering the optical threshold benefits the results, since the change of index versus optical intensity in a quantum well active layer shows a saturation characteristic. This means that material sensitivity decreases at higher optical power densities, and for a given input optical power, one can obtain a higher total change of phase if the nonlinear medium is elongated in the optical propagation direction (resulting in a lower optical density). Therefore, bistable ridge waveguides can fundamentally provide a higher sensitivity and lower optical threshold than their vertical counterparts. Finally ridge waveguide geometry has obvious advantages over the vertical cavity geometry in terms of any potential integration.

3.3.5.3 Waveguide Bistable Etalons

Sarnoff Corporation provided samples of waveguide devices which had been developed for another program. Details of those structures were not provided, but their experimental results showed that bistability was observed. Figures 3-24 and 3-25 show the experimental results from Sarnoff and SNDP, respectively. When the input pulse was on the falling edge, the output of the device remained highly transmitting with respect to time. This program was ended before SNDP could investigate waveguides further, but these results indicate that the conceived SNDP architecture could be realized.
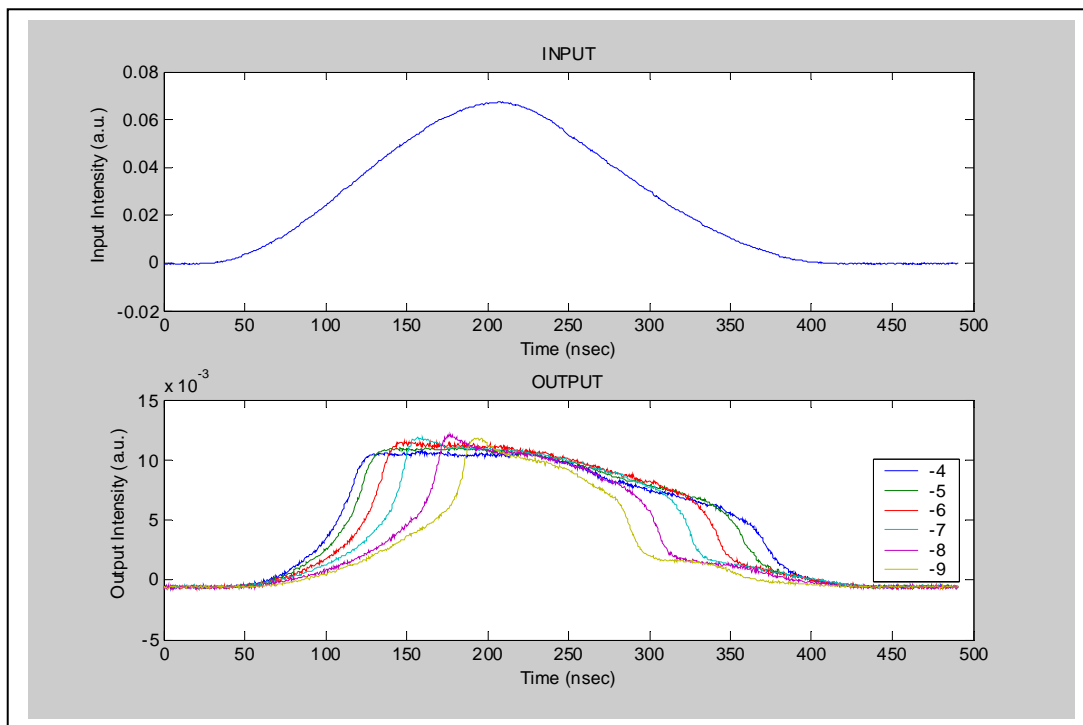
Figure 3-24. Sarnoff's measured results on bistable waveguides.
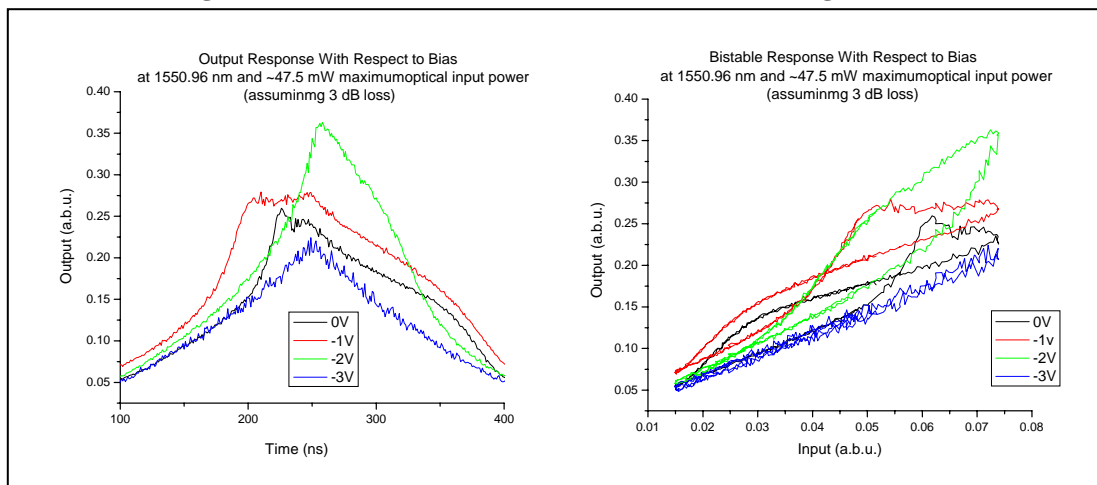
Figure 3-25. SNDP's measured results on bistable waveguide.

3.4 Photonic ADC Architecture Conclusions

There are, in summary, several important advantages for quantizers making use of a SA based configuration. The RF signal is sampled optically and remains in optical domain, so the electronic signal is free of distortion. An advantage of this technique over some others is that photodiode linearity is not a limitation because the photodiodes are used as comparators with no need to sample the entire dynamic range.

It is also significant that in this flash architecture, using SAs actually *allows the electronic comparators to have a single reference voltage,* which alleviates the difficult task of holding and deciphering differential voltage levels. This key feature differentiates the in-house photonic ADC system from traditional electronic flash architectures. In an electronic, flash architecture, 2^N reference voltages are required, and in a system with a large number of bits, it is difficult to accurately generate and stabilize these voltages. By using passive SAs, rather than electronically controlled switching elements, and by avoiding the use of electronic ADCs, the power requirements may be much lower than in other photonic schemes, although the resolution limit is unknown at this point. In contrast to other photonic ADCs, the basic components of this ADC may be integrated on a single substrate using integrated electro-optic techniques. The multi-gigahertz requirements of photonic ADCs can be met by exploiting the ultrafast processing speed of the multiple quantum wells (MQWs) that comprise the SAs as well as EAMs and photodiodes. As previously mentioned the ultimate speed of the system may still be limited by the convergence time of the etalon as well as the electronic comparators. SAs in a waveguide etalon configuration are essential to offer a viable solution. Finally, in addition to the physical size and power consumption, the SA based architecture conceptually is much less complex than the other photonic schemes.

Chapter 4. Electro-Absorption Modulators

4.1 EAMs: Evolution of the State of the Art

The success of this particular in-house ADC architecture, and that of many other ADC designs, relied on the advancement of mode-locked lasers and electro-optic (E-O) modulators. The front end of the ADC architecture system used a mode-locked laser and an E-O modulator to sample the RF input signal; together they comprise the "RF link portion". SNDP worked closely with Professor Paul Yu from UCSD on electro-absorption modulator (EAM) technology; his group provided sample devices and extensive consulting with regards to theoretical issues. The productive collaboration included test fixture design as well as specialized device characterization methods. This chapter discusses E-O modulators, explains the advantages of EAMs, and follows with an overview of UCSD's contractual research results for electro absorption modulators. Further discussion is provided in the final reports[57-60]. Lastly, the in-house experimental setups, procedures, and test results are described for the EAM devices.

There are primarily three competing material systems used for high speed electro-optic modulator devices: lithium niobate ($LiNbO_3$), semiconductors, or polymers. $LiNb0_3$ Mach-Zehnder (MZ) modulators are commercially available and are useful for laboratory demonstration, but their Spur Free Dynamic Range (SFDR), or linearity, falls short of that needed in many Air Force applications. The modulators used in high resolution photonic ADCs and RF links typically require a SFDR greater than 130 dB $Hz^{2/3}$, whereas state-of-the-art MZ modulators have a SFDR of approximately 110 dB $Hz^{2/3}$. Polymer modulator technology is not as mature as that of $LiNbO_3$ or semiconductor devices, and cannot be readily integrated with the other components of a semiconductor based ADC system. Such devices use a Mach-Zehnder configuration, so the required interaction length of several centimeters makes multi-device integration in an ADC even more difficult.

A *fundamental* advantage of EAMs over established $LiNbO_3$ MZ technology is the flexibility to linearize the performance by suppression of the 3rd order intermodulation product (IP3). With its sinusoidal transfer curve, a *single* stage MZ at quadrature suppresses even order effects, but *cannot* suppress any odd order (3rd in particular) effects regardless of bias value. MZ devices can only be 'linearized' (suppression of 3rd order slope of IP3) by the use of specially designed multiple stage MZ or directional coupler devices[61,62], which add significant complexity to fabrication and operational control.

The EAM approach places the design effort on the media itself. The single waveguide stripe itself involves little complexity and no interferometric effects. The 3rd order slope of IP3 can be directly suppressed at a proper bias, and if the transfer curve characteristics can be tailored properly, 2nd and 3rd order intermod products can be simultaneously suppressed to yield a highly linearized device. To achieve optimum modulator linearity, several trade-offs are involved for V_π, material thickness, length, and electrode design.

The expression for the dynamic range of a modulator shows that SFDR is inversely proportional to noise figure, gain and bandwidth. Therefore a greater bandwidth or gain due to improved technology does not improve SFDR, unless the IP3 can be improved as well. In depth equations are described by Welstand[63],

With EAMs it is the effects at the edge of the material's bandgap that are exploited, in particular electro-absorption and electro-refraction. EAMs make use of the Franz-Keldysh Effect (FKE), or the Quantum Confined Stark Effect (QCSE), or simultaneously a combination of those. The p and n doped materials act as cladding layers in a waveguide, which confines the light propagation. The absorption at a fixed wavelength can be controlled with the reverse bias voltage applied to the modulator, and this change in absorption with applied electric field results in a shift of the band-edge to longer wavelength. A transfer curve for an EAM can be used to model those characteristics[64]:

$$T_{EA}(V) = t_e e^{-\gamma \alpha(V)L} \tag{4-1}$$

Where T_{EA} is the transmission, γ is the confinement factor, $\alpha(V)$ is the absorption coefficient at a DC bias, and L is the waveguide length. Figure 4-1 illustrates modulation of the optical signal by RF input[63].
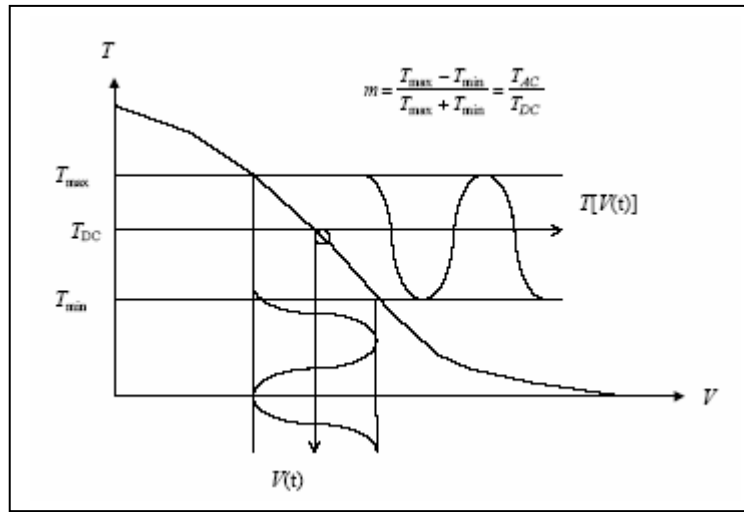
Figure 4-1. Modulation by RF input signal given by an optical transfer curve[63].

The term "slope efficiency", often discussed in EAMs, is the derivative of the normalized transfer curve (T_N) with respect to voltage. Because EAMs are not sinusoidal, they do not have a V_π (180 degree phase change at a particular voltage) as do Mach-Zehnder modulators. However, by using the slope efficiency an equivalent V_π can be calculated, so the performance characteristics of EAMs can be compared directly with those of Mach Zehnder devices[63, 64]:

$$V_\pi = \frac{\pi}{2 * \left. \frac{\partial T_N}{\partial V} \right|_{max}} \tag{4-2}$$

Low V_π is necessary for a high RF link gain; the ultimate goal of most work in this field is to achieve $V_\pi < 1.0$ V.

Examination of equation 4-3 shows that the link gain is directly related[63] to the slope efficiency by,

$$G_{RF} = \left(P_{opt} \cdot \frac{\partial T_N}{\partial V} \cdot \eta_{ins} \cdot \eta_{det} \right)^2 \cdot R_{in} \cdot R_{out} \tag{4-3}$$

where P_{opt} is the optical power, η_{ins} is the insertion loss, η_{det} is the detector efficiency, and R_{in} and R_{out} are the input and output impedance. To achieve high RF link gain, the EAM needs high optical power handling with low loss coupling to single mode fiber. Low optical residual propagation loss is required to ensure small insertion loss, and a large optical/microwave field interaction volume is needed to yield a low V_π for high RF link gain. In summary, improving the optical insertion loss, optical power handling, or V_π can lead to improved gain, IP3 and noise figure. During this effort Paul Yu examined various methods of improving on these factors, and in-depth analysis for those is given in the final reports that were submitted[57-60].

Figure 4-2 illustrates the evolution of EAM waveguide design. Traditional EAMs have a strongly confining intrinsic layer in the PIN structure so the optical mode tends to be elliptical. To improve on optical power handling, insertion loss, and linearity, a more circular mode can be obtained by designing the device to have a large optical core (LOC). This facilitates the coupling and improves the mode matching to a fiber. There are several distinct types of LOCs; earlier designs focused on a LOC with the active EA layer sandwiched between the waveguiding layers on each side. The dilute core is another type of LOC; it is asymmetric with respect to only the waveguiding layer on the lower side of the active layer, while the EA layer still has a large confinement factor similar to the symmetric LOC. The peripheral coupled waveguide (PCW) differs from the dilute core in that the confinement (~ 4%) in the active layer is very small and the optical mode is mainly in the waveguiding layer, so it may be viewed as an extreme case of the single-sided LOC (dilute core). The designs which evolved in this manner greatly improved on the optical power handling capacity, hence also the linearity.
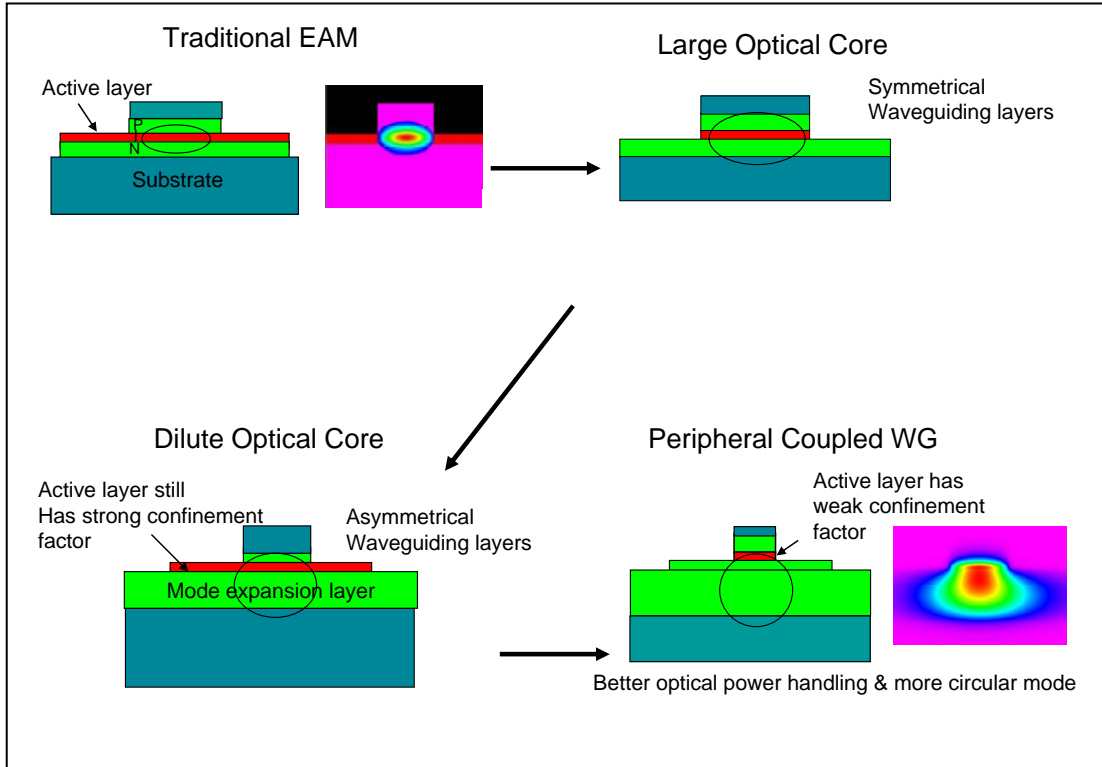
Figure 4-2. Schematics of EAM waveguide evolution.

In conventional EAMs large bandwidth and high slope efficiency require a traveling wave (TW) electrode for the large interaction length. However, sharing of the EA layer in the

optical and microwave waveguides results in a compromise of EA thickness. Residual absorption gives a high propagation loss limiting device lengths to 200-300 μm[58,65]. These short lengths with thick EA layers preclude a small equivalent V_π and yield high propagation losses causing large insertion losses. In addition, photogenerated electro-absorption current per unit length also limits the highest optical power handled by the device, but longer TW designs can overcome some of these obstacles.

Modulation bandwidths for TW-EAMs were measured to be > 50 GHz[65]. The TW-EAM modulation frequency response is determined by the waveguide properties, including waveguide impedance, microwave velocity and microwave loss. Long device length can increase the optical/microwave interaction, which promotes higher modulation efficiency. Professor Yu determined that maximum link gain was achieved with a waveguide length of ~ 200 μm[58,65]. He also demonstrated that proper termination for short TW-EAM breaks the RC-limit rule for bandwidth. With 50 Ω termination, an L-EAM bandwidth is 20 GHz and a TW-EAM was 21 GHz. At 22 Ω termination, an L-EAM improved to 30 GHz and a TW-EAM was greater than 50 GHz.

Improving the optical power handling was demonstrated in a PCW EAM, where the optical core layer was undoped. The microwave electrode design could, therefore, be decoupled from the optical design. The microwave electrode's location, including the EA region, was peripheral to the optical waveguide mode, but within its evanescent field. The low confinement factor in the EA layer reduced the photogenerated current per unit length, and greatly enhanced the power handling of the EAM. The design of the microwave electrode affects the optical mode minimally, so a small EA thickness could be used to lower V_π. Since the guided optical mode was also further from the surface, it experienced lower propagation loss (< 2 dB/mm) and reduced the insertion loss significantly. This method also permitted waveguide lengths exceeding a millimeter, thereby allowing even lower V_π to improve the RF link gain 15 dB over that of a conventional TW-EAM. Lastly the optical waveguide also had a larger and more symmetric mode shape to better match that of a single mode fiber (See PCW insert in Figure 4-2). Typical conventional MQW TW-EAMs have a small optical saturation power, ~ 2 mW. UCSD demonstrated PCW EAM use with high optical power of ~ 80 mW before saturation[66]. Even with a footprint on the order of millimeters, PCW structures are still an order of magnitude smaller than traditional Mach-Zehnder modulators, and are inherently compatible with semiconductor based device integration.

Another way to improve the device optical power handling is to incorporate intra-step-barrier quantum wells (IQW) in the active region[59,67,68]. IQWs are essentially a quantum well within a quantum well. A portion of the well is replaced by the higher bandgap materials and the step barrier works as a barrier for the holes. An example of the structure is shown in Figure 4-3[59,67,68].
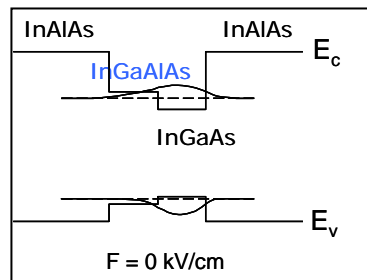
Figure 4-3. Schematic of IQW[59,67,68].

Normally the saturation optical power of the MQW EAM is relatively small due to the carrier pile-up in the well, which leads to electric field screening and optical saturation. This can be improved by using materials with a small valence band offset, e.g. InGaAs/InAlAs, InGaAsP/InGaAsP) to increase the electric field and reduce the pile-up screening effect. Simply increasing the bias voltage is not effective because of the associated drop in gain (slope efficiency).

The IQW design suppresses the onset of electroabsorption as Yu explains[68] in depth,

> [At zero electric field (A) in Figure 4-4], the electron in the conduction band is rather loosely confined over the whole well region, while the hole is tightly confined in the deeper intrawell, mostly due to the effective mass difference. As the electric field is applied (B), in the -z direction, the electron envelope wave function moves in the +z direction, while the hole envelope wave function spills over the intra-step-barrier in the -z direction. Up to this point, the overall transition energy shift is very small or even a little positive (blueshifted). This is because the hole energy level increases with the electric field although the electron energy level decreases. Hence, the normal redshifted QCSE is effectively suppressed. With the electric field further increased, the energy shift becomes negative (redshifted), as the hole envelope wave function spills further over the intra-step-barrier (C), and the hole energy level starts to decrease. Also the oscillator strength, which is proportional to the square of the spatial overlap integral between the electron and the hole envelope wave functions, changes dramatically as the hole envelope wave function spills over the intra-step-barrier. At a larger field (D), the hole is mostly confined over the intrastep- barrier and the oscillator strength becomes very small. Therefore, optical saturation power is increased by suppressing the onset of the quantum confined Stark effect (QCSE) to higher voltages.
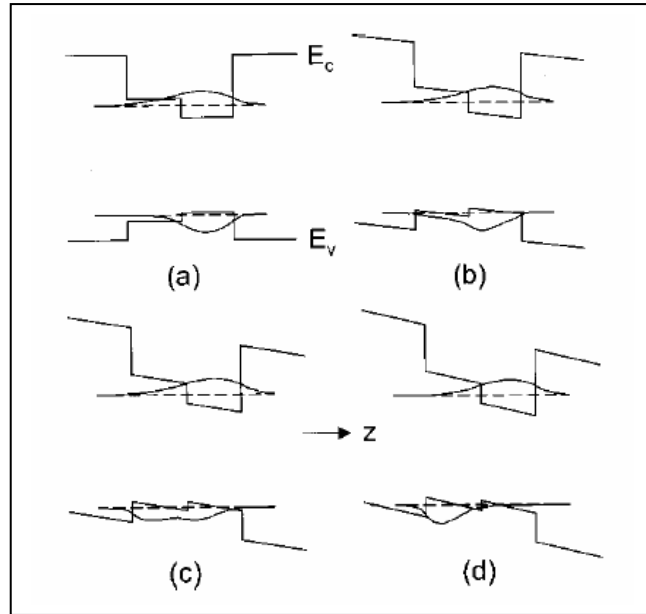
Figure 4-4. Schematic of confinement as bias is applied to IQW[68].

4.2 Experimental System for Testing EAMs

SNDP has also worked contractually with UCSD to promote the development of electro-absorption modulators and leverage Paul Yu's world leading expertise. UCSD provided SNDP with modulators, and a test system was built to be capable of characterization up to 40 GHz bandwidth. This enabled SNDP to establish experience in the testing of EAMs, which was also

required for the team to provide third party testing of such devices for AFRL's Wideband Agile Receiver (WAR) program[69,70].

A photo of part of the in-house optical assembly is shown in Figure 4-5 with a cartoon schematic inserted. A microscope views the devices from the top and a photo of some EAMs are shown in the next figure. The EAMs were cleaved from the wafer so that the waveguide arrays could be carefully silver-epoxied to a copper mount without damage to the end facets. Newport ULTRAlign^{TM} stages allowed lensed fibers to be precisely aligned at the input and output interface of the device. A JDSU fiber coupled laser diode was used as the source, because at that time, it provided the lowest value of relative intensity noise (RIN) (~ -160 dB/Hz). The polarization was oriented with controllers and optimized for maximum slope efficiency. Most EAMs are polarized horizontally to the substrate and thus correspond to a TE polarized state. EAMs can also work with TM polarization, but not as efficiently. The collecting lensed fiber was connected to a fiber pigtailed photodiode, which sent the RF information to the test equipment. A ground-signal-ground (GSG) coplanar 40 GHz probe with 50 µm spacing from Cascade Microtech was used to deliver the DC bias and RF signal.
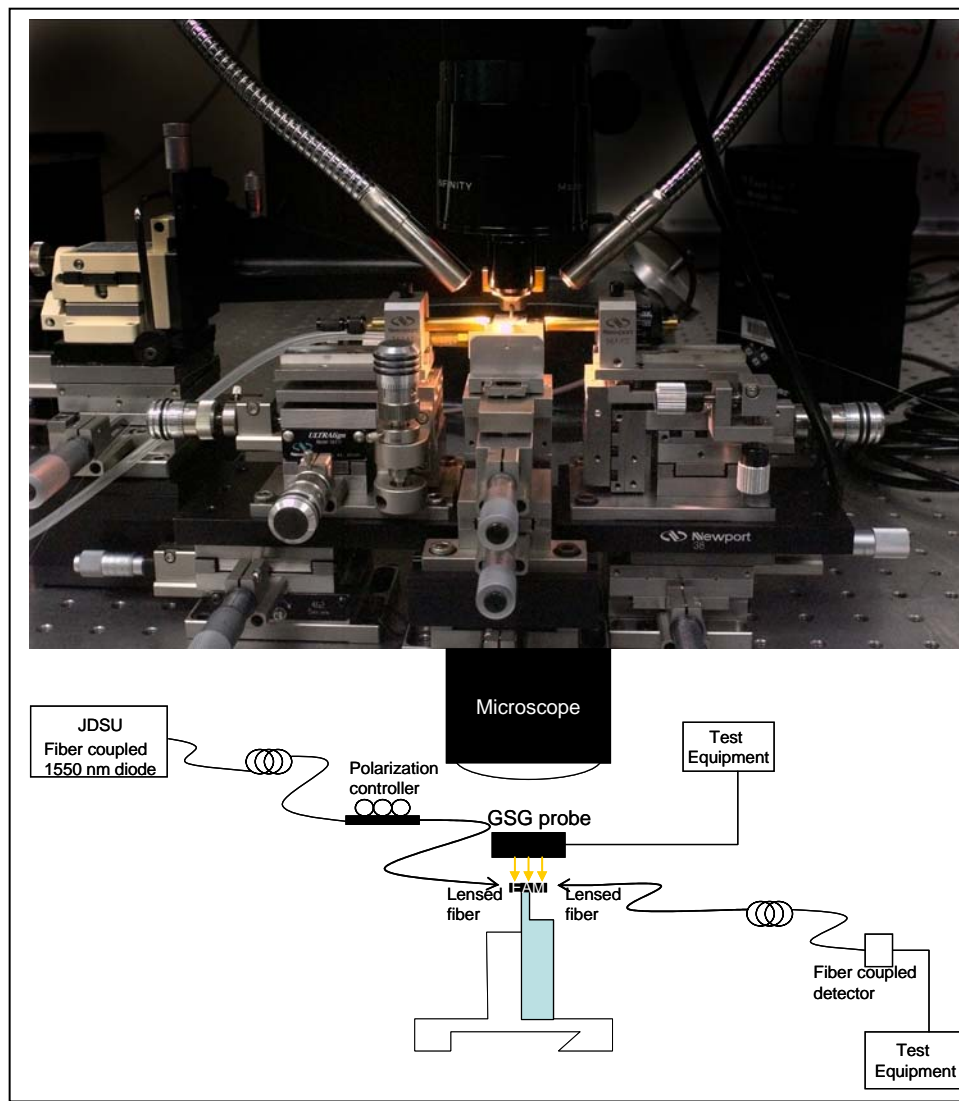
Figure 4-5. Experimental setup for testing EAMs.
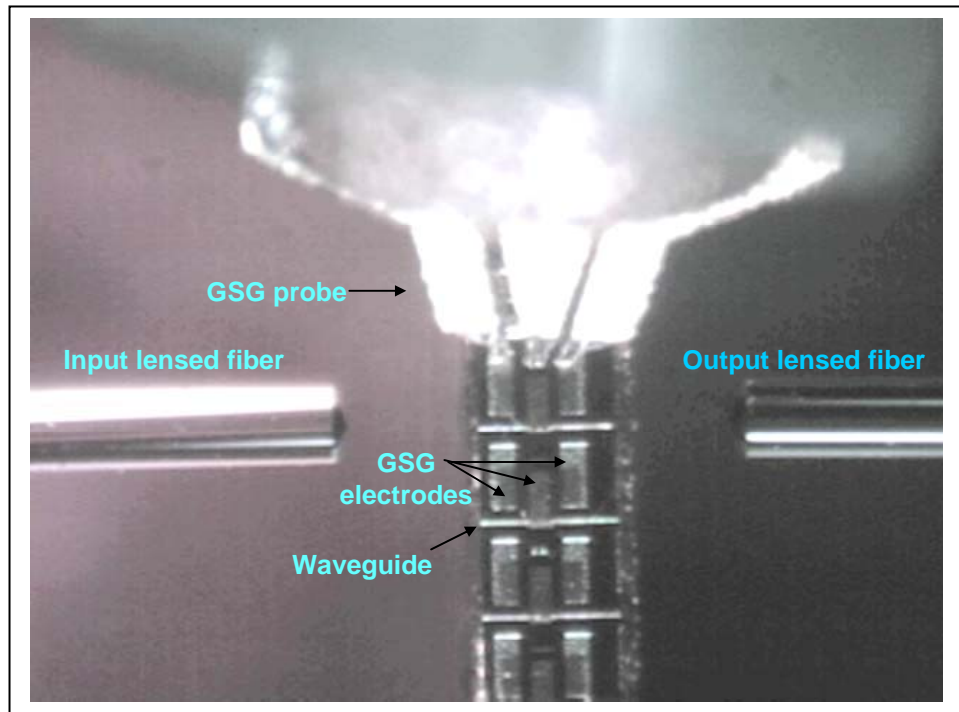
Figure 4-6. Top view of EAMs with lensed fibers shown at input/output.

Because EAMs were at least 180 μm long, special mounts had to be machined, one for the EAM mount and one to adapt to the Newport ULTRAlign^{TM} micro-positioning stages. These schematics are shown in Figure 4-7. It was critical that the mount's width be less than the EAM length, so as to allow efficient input/output coupling of fibers. The EAM mount screwed to the machined ULTRAlign^{TM} adapter as shown in the figure.
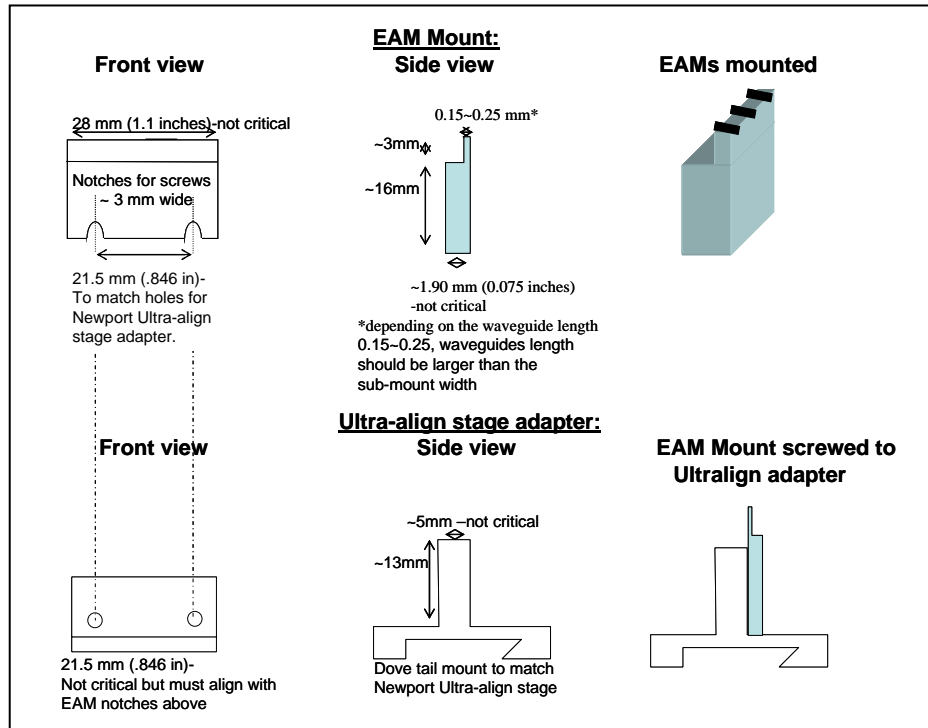
Figure 4-7. Custom mounts for mounting EAMs into experimental system.

4.3 Procedures for Testing EAMs

After visual inspection of devices under the microscope, electronic characterization was performed. The first step involved probing the devices to obtain a characteristic I-V diode curve. An Agilent 4155C semiconductor parameter analyzer (SCPA) was used to test these devices by scanning the reverse bias to determine the breakdown voltage. The voltage output was connected to the probe cable and the current generated in the modulator due to the applied bias was monitored. Typical I-V traces are shown in Figure 4-8 and represent characteristic diode behavior. The acquisition and storage of the measured data was performed with LabVIEW software, and Appendix A shows the LabVIEW user window and wiring diagram for the instruments. The user simply entered the instrument address and the X and Y axis names. If there was another variable to be monitored, a second set of axes could be entered and designated by X2 and Y2. (Note: "Time" is mislabeled on the X axis on the graphical user interface shown in the appendix, but the data with this program was captured correctly.)
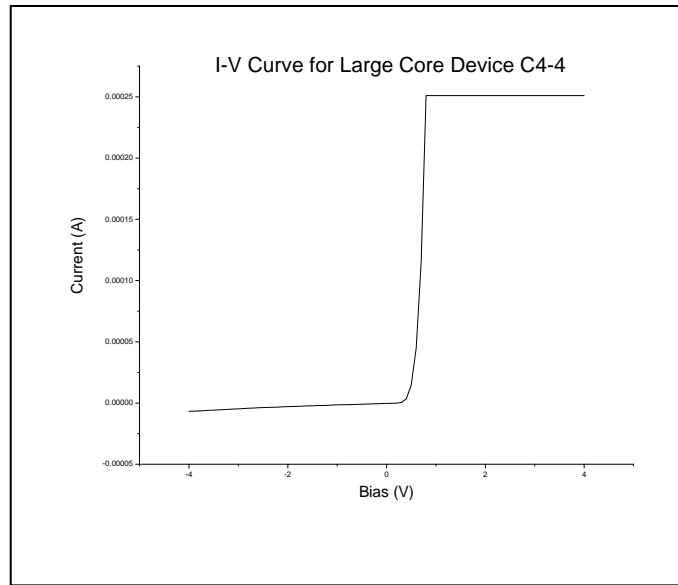
Figure 4-8. I-V trace of a lumped element QW LOC device 215 μm long.

After a device functioned electrically, it was optically tested to verify that light coupled into and out of the waveguide. The most direct method for this was to treat the modulator as a detector and use the same instrumentation. A variable voltage was still used and the current was monitored from the diode in the same way. A second variable was entered to provide a constant voltage to bias the detector, and its current was monitored through a second port. (Note: A different power supply can be used to bias the detector, but it was simpler to monitor the current of the detector using the instrument). As light was injected via lensed fiber into the device, the modulator current increased. This was maximized by adjusting the fiber position and monitoring the instrument's display. Once the fiber position was optimized, the other end was disconnected from the fiber coupled laser and connected to the detector. In turn the laser was connected to the fiber on the other side of the modulator and the alignment procedure repeated. Once the second fiber was aligned, the original configuration was restored. This gave good approximate optical alignment, and sufficient power was generally coupled into the detector to see the current generated on the SCPA. The positions were then "tweaked" and the polarization adjusted to provide optimal optical performance for the transfer curve data. An example of the output is shown in Figure 4-9 for ~ 2 mw input. This was examined for input power levels from 0 dBm up to the saturated maximum value, while watching for residual leakage, which results if the transfer curve at large input power fails to exhibit extinction at a large reverse bias.
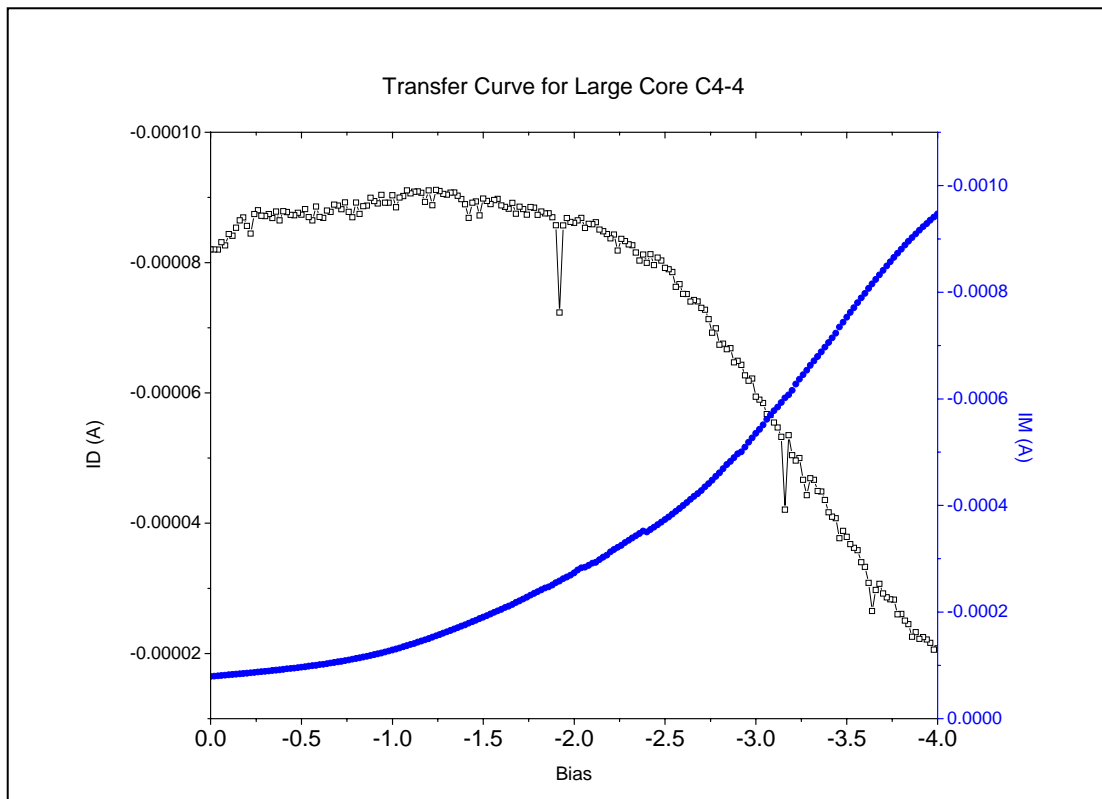
Figure 4-9. Transfer curve of a lumped element QW LOC device 215 μm long.

RF measurements could be performed once optical alignment was obtained. These included frequency response, gain and SFDR measurements, all of which are found from derivatives of the transfer curve. The derivatives were obtained with computational software or a spreadsheet, such as MathCAD and Excel. The data was imported, fit to a higher order polynomial, typically 7th order, and the derivatives calculated. An example MathCAD calculation is shown in Figure 4-10. When the 1st derivative is a maximum, the 2nd derivative equals zero. When the bias voltage was set to meet that condition, the EAM had optimal broadband performance. This is because the second order intermodulation products were minimized, so that only effects of higher nonlinear order, with smaller magnitude, limited the SFDR.
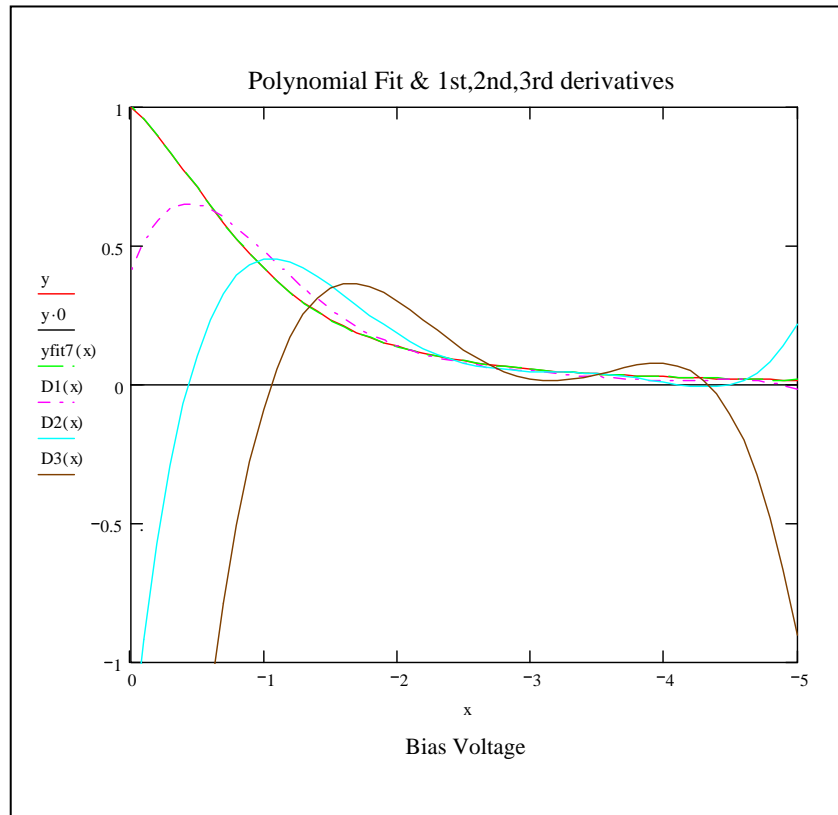
Figure 4-10. MathCAD derivatives for a commercial EAM Cyoptics with 2 mW input.

The frequency response was measured with Agilent's 86030A Lightwave Component Analyzer, comprised of a spectrum analyzer, 8510C vector network analyzer (VNA), 8717 B S-parameter test set, and 86032A Lightwave test set. The advantage of this system was that there was an internal 1550 nm laser diode and a calibrated internal photodiode. The system guided the user through a full calibration prior to use and provided straightforward RF frequency S11 (reflection) and S21 (throughput) measurements. One port measurements were used for EAM devices. Calibration was first performed up to the connection of the probe, so that subsequent measurements included contributions from the probe and the device under test.

To deconvolve the probe contribution from the measurements, a routine was written with MatLab (See Appendix B). Probes typically come with S parameter data which can be read into a file and mathematically eliminated. If this data is not available it can be measured as follows: The calibration is performed up to the connection of the probe to eliminate all effects from cabling and connectors. A ceramic calibration standard (ours from Cascade Microtech) was used to probe and measure an open, short and load. A picture of this calibration standard is shown in Figure 4-11. Each data file was saved and then read into the program so that file names matched the parameter names in the program.
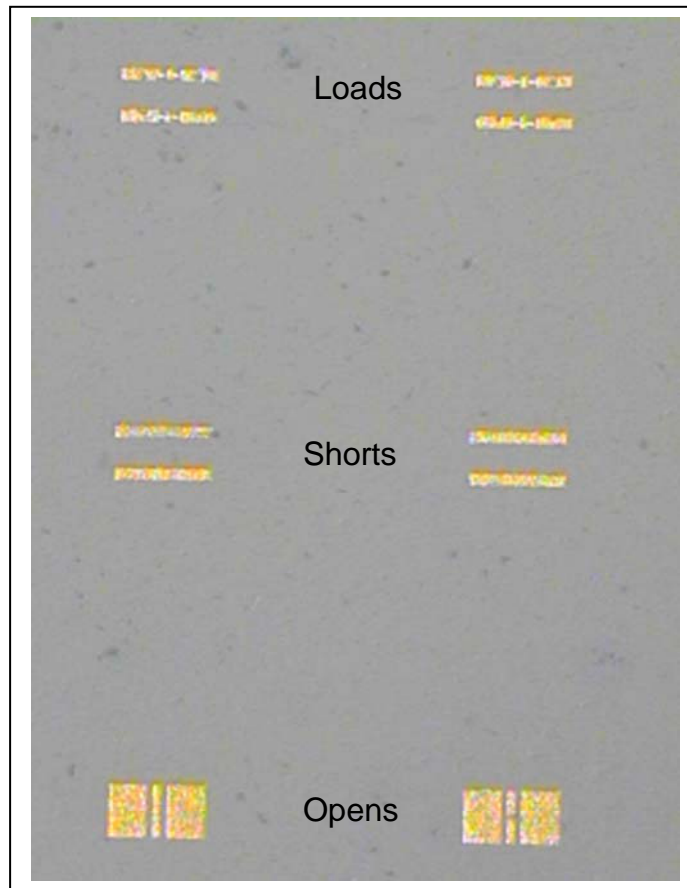
Figure 4-11. Open, Shorts and Loads on a ceramic substrate used for calibrating out a probe.

If a Lightwave Component Analyzer is not available, the same measurements can still be performed with a standard VNA, an S-parameter test set, an external laser and detector. The test setup is shown in Figure 4-12. Calibration would be carried out the same way for the probe, but the detector would be characterized and calibrated to cancel out its contributions. The S parameter data for a detector can be obtained from the manufacturer or one can measure it using the VNA, and its data would be then called into the OurCaliMod routine (Appendix C). When using the Lightwave approach, the lines of code related to the detector information are commented out because the Lightwave system automatically accounts for the internal detector during the calibration routine. When not using the Lightwave approach these lines of code need to be enabled.
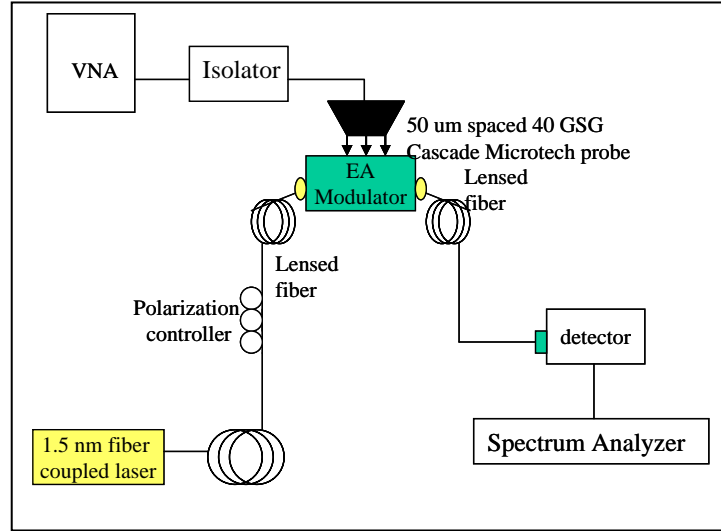
Figure 4-12. Experimental setup for measuring the frequency response if a Lightwave analyzer is not available.

Figure 4-13 shows frequency response results of a lumped element (LE)-QW LOC modulator with a length of 215 μm tested in-house by the methods described above. The 3 dB roll off point was ~ 4.5 GHz and remained there out to at least 7 GHz. There is a sharp low frequency roll off from 0.2 to 0.5 GHz, likely due to errors in the calibration or measurement. Another sharp roll off at ~ 3.5 GHz occurs for S21 (throughput) while an increase in S11 (reflection) occurs at the same frequency. This peculiar behavior was repeatable but the reason for it is not known.
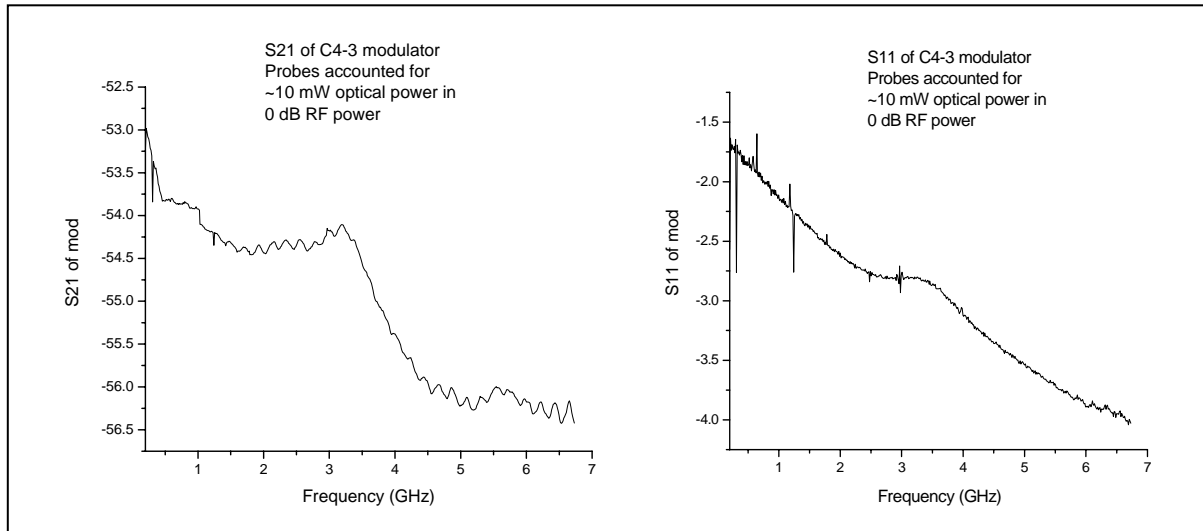
Figure 4-13. S-parameters measured with probes contributions deconvolved from the measurement for a LE QW LOC-- 215 μm long.

The next test to characterize EAMs was the measurement of linearity, or SFDR. To have unambiguous results it is necessary to ensure that the detector itself is sufficiently linear so that its IP3 contribution is negligible. The high power, large bandwidth, high speed detectors (Discovery Semiconductor # 30S) used in our experiments met that requirement.

If an uncharacterized detector is to be used, however, the following procedure needs to be performed. The experimental setup is shown in Figure 4-14. Two MZ polarization dependent modulators are used and need to be controlled with the input. After the modulators and before the coupler, the polarization of the arms must be orthogonal, which is indicated when the noise floor on the spectrum analyzer is a minimum. No more than 10 dB optical input power should be used. The bias is set so that the IP2 signal is nulled on a spectrum analyzer, while the fundamental and IP3 remain. When the laser is turned off, so as not to excite the detector, the RF will still pass. If IP2 is observed, such as 2f1 - f2, then it is from the detector, and it can be measured by turning the laser back on.

The saturation of the detector also needs to be known or measured to ensure that it remains in the linear region. Measuring this is more difficult and requires three lasers near the same wavelength as shown in Figure 4-14. The optical power at which the detector response rolls off identifies the 1 dB compression point, and the detector should not operate beyond it. The upper two lasers in the diagram beat together and generate the RF signal for this test. The wavelength is controlled through the phase locked loop, and the optical attenuators allow the power to be varied so as to generate the RF vs. Optical Power curve.
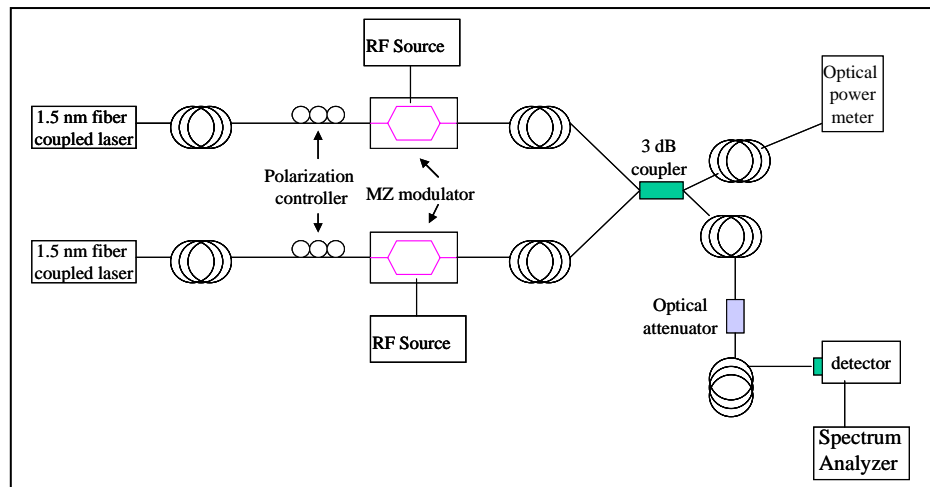
Figure 4-14. Experimental setup to measure the linearity of a detector.
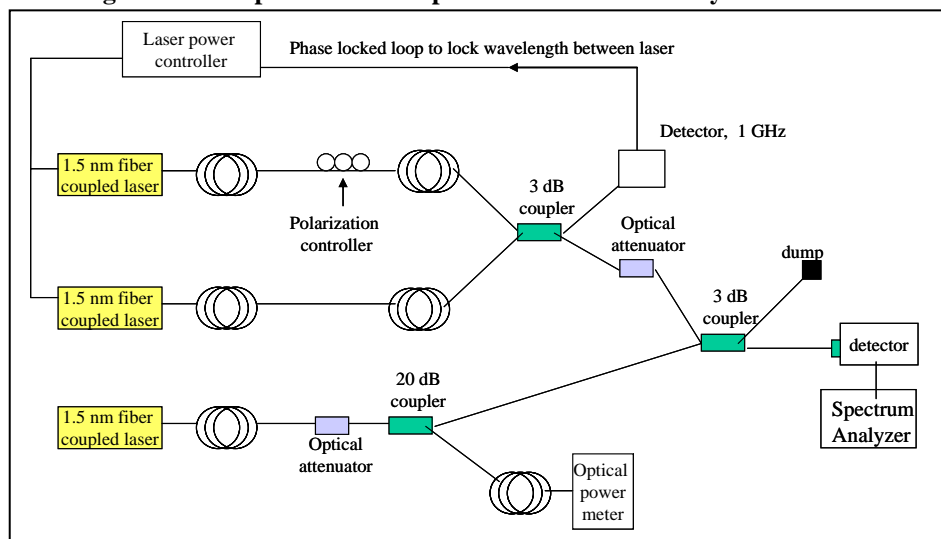
Figure 4-15. Experimental setup to measure the 1-dB compression point of a detector.

Once it is verified that the detector is sufficiently linear, the SFDR measurements can take place. The experimental system used is shown in Figure 4-16, and the instruments were automated using LabVIEW. The user interface panel and wiring diagrams are shown in Appendix D. This experiment mixed two RF signals customarily separated by 10-20 MHz. As with traditional electro-optic modulators, the second order intermodulation product can be nulled at the particular bias where the 2nd derivative of the transfer curve equals zero. This is observed experimentally by monitoring the IM product while scanning the bias voltage. The ideal bias point may exhibit some drift so the measurements should be carefully monitored. Once the IP2 is nulled, the fundamental and IP3 are measured as a function of increased RF input power. When these two are plotted, the SFDR can be graphically displayed or calculated.
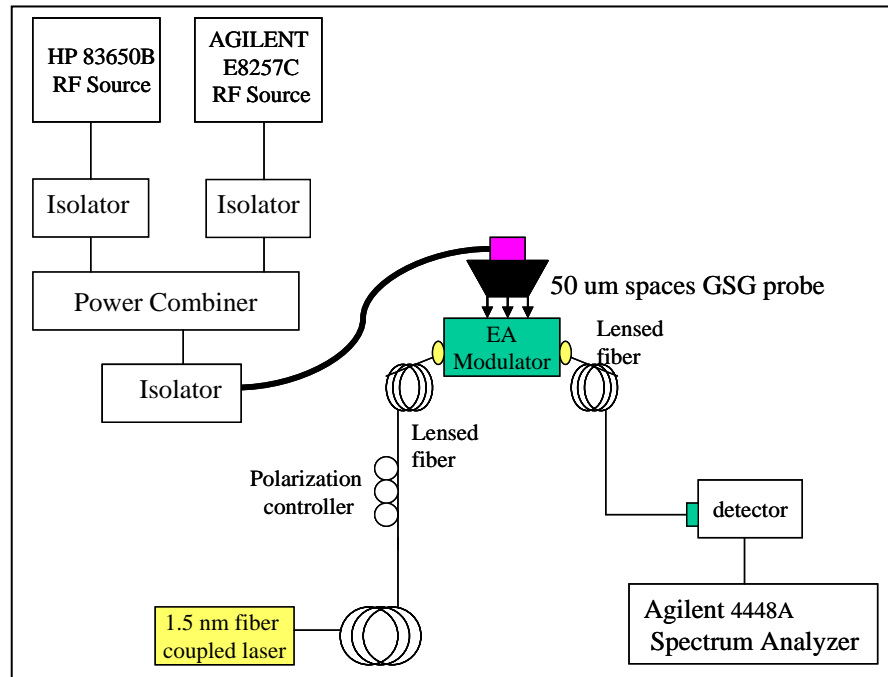
Figure 4-16. SFDR experimental setup.

The LabVIEW interface allowed the user to enter the instruments' addresses and the desired frequencies along with any offset the RF sources may have. The span and resolution bandwidth of the spectrum analyzer were set as well as the RF power range and power increments. A toggle switch was available to turn on and off the second order measurements, though the program operated faster with it off. The noise floor was calculated and then entered into its appropriate cell, and the calculation was performed using a MathCAD routine and is shown in Appendix E. The data was read into an Excel spreadsheet some plots of which are shown in Figure 4-17.
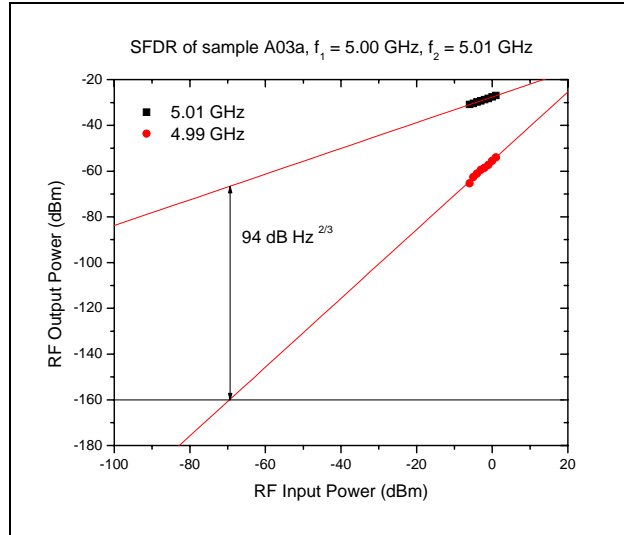
Figure 4-17. SFDR measurements of early devices.

As previously mentioned EAMs are capable of nulling IP3, which is particularly applicable to narrowband applications. When the bias is set to null the 3rd order derivative, the IM3 exhibits a 5th order slope dependence, which yields a higher SFDR. The same automated program was used to measure this dependence, and the best measured results were obtained at UCSD for a PCW device[60,66].

The wideband and narrowband measurements performed by UCSD are shown in Figure 4-18. The SNDP test facility was not prepared at that time to perform independent measurements on those particular devices. Other sample devices were provided in order to develop the proper alignment, probing, interfacing and all other necessary handling techniques, and they were largely used up in that process. The experience gained enabled most of the testing methods to be successfully developed subsequent to the termination of this project. Those results will be reported in full detail in the current in-house EAM project.
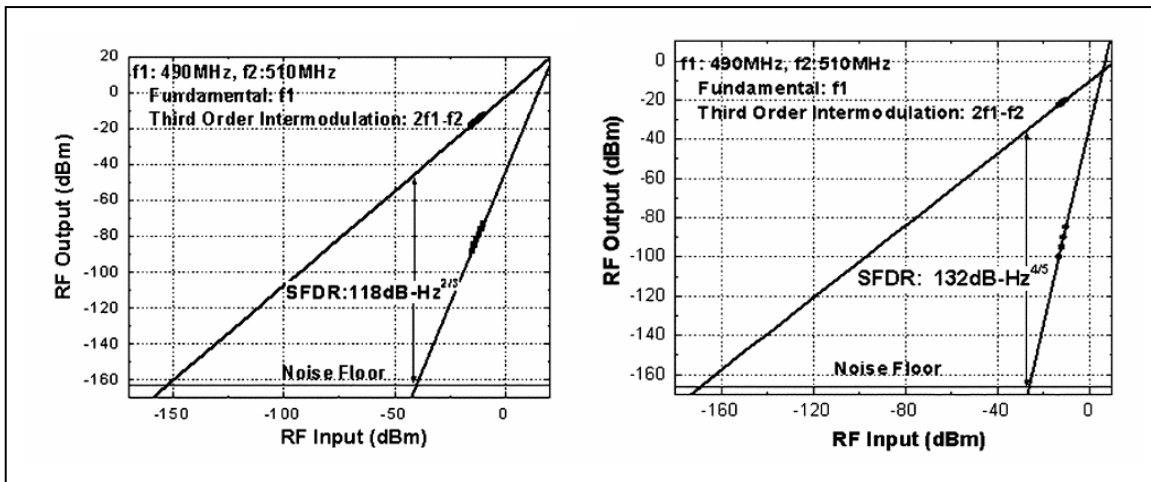
Figure 4-18. Wideband and narrowband SFDR results for a PCW device[60,66].

In summary, substantial time and effort was required to build up the highly specialized physical test system and to develop the associated LabVIEW routines for automated control and

53

data acquisition. SNDP's methods, which were in some respects more efficient than those implemented at UCSD, were shared with them so as to advance the instrumentation control used in their characterization. For measurements that require full device characterization beyond 10 GHz, SNDP's capability exceeds that of UCSD; this could assume critical importance now that EAM devices approach the performance entailed in recent broadband AF system specifications.

Another major problem involved the fragile unpackaged nature of the devices provided. The waveguides were usually in bar form, and often did not function properly, either electrically or optically. For this reason the SNDP Semiconductor Modulator development team is expanding the project's scope to include theoretical modeling, fabrication, and simulation capability. The other goal is to augment UCSD's lack of packaging expertise; SNDP will coordinate the engineering needed to provide more robust and stable devices that are ultimately more suitable for Air Force applications.

Chapter 5. Mode-Locked Lasers

5.1 Mode-Locked Lasers for ADC Applications

The mode-locking of a laser refers to the generation of ultrashort pulses with 1×10^{-12} to 10^{-15} s pulse widths; their generation in a laser cavity can be achieved by a variety of methods. Many parameters need to be considered when choosing a mode-locked laser for use as a sampling source in a photonic ADC; of particular importance are pulse width, pulse repetition rate, power, size and stability. The pulse width determines the width of the aperture sampling window. Its maximum width, τ, is given by

$$\tau < \frac{\left(\dfrac{3}{2^{N-1}}\right)^{1/2}}{\pi f_{max}} \qquad (5\text{-}1)$$

where N is the number of bits of ADC resolution, and f_{max} is the maximum analog input frequency[19, 71]. For example, for a specification that breaks the Walden Wall limit, a 10 GS/s sample rate (5 GHz BW) ADC with 12 bits of resolution, the maximum pulse width allowed is 2.4 ps, while a 100 GS/s sample rate (50 GHz BW) ADC with 4 bits requires a maximum pulse width of 3.9 ps. These pulse widths can be generated using a variety of lasers, but the repetition rate of the laser determines the sampling speed of the ADC. Using the Nyquist theorem, an 18 GHz RF signal must be sampled at a minimum of 36 GS/s, requiring a laser with a 36 GHz repetition rate. The required laser power is dependent upon the ADC system architecture, and it must be high enough at the receiver to yield an acceptable SNR. Closely tied to the power requirement is the size of the laser; it should be small enough to allow integration or to permit remote distribution to a series of photonic ADCs.

Laser stability is the most important parameter that needs to be considered for a photonic ADC; stability refers to both the amplitude fluctuations and the timing jitter of the pulse train, and both of those lead to errors in the sampled signal. Timing jitter, defined as fluctuations in the laser repetition rate or variation in the pulse to pulse arrival time, is given by:

$$\sigma_{J_T} = \frac{1}{(2\pi f_m)} \sqrt{2 \int_{f_L}^{f_H} L(f) df} \qquad (5\text{-}2)$$

where f_m is the mode-locking frequency, f_L and f_H are the frequency limits of the integration, and $L(f)$ is the spectral density in dBc/Hz [71].

Compared with amplitude fluctuations the timing jitter is not as easily controlled, but a mode-locked laser with ultra-low timing jitter is essential for a high resolution ADC. The maximum allowable timing jitter, δt is given by[19, 71]

$$\delta t < \frac{1}{2^{N+1} \pi f_{max}} . \qquad (5\text{-}3)$$

To look again beyond the Walden Wall limit, a 10 GS/s sampling ADC with 12 bits of resolution requires less than 7.8 fs of jitter and a 100 GS/s sampling ADC with 4 bits of resolution requires less than 198.9 fs of jitter. Extensive research efforts were, therefore, initiated, both contractual and in-house, toward developing a laser with a timing jitter less than 10 fs. Haus[72] showed that timing jitter was primarily due to cavity length fluctuations, which result in fluctuations in the pulse arrival time. This is particularly true of passively mode-locked lasers where the cavity length exclusively determines the pulse repetition rate.   In actively, as well as passively, controlled mode-locked lasers, fluctuations in the cavity length are in part due to environmental instabilities.   Temperature fluctuations within the cavity medium, such as erbium-doped (Er-doped) fiber, can lead to cavity length changes on the order of several microns, and thereby alter the repetition rate by hundreds of hertz[73]. Smaller fluctuations, such as cavity vibrations cause fluctuations at acoustic frequencies, which have a much smaller effect on the repetition rate than the temperature fluctuations.   Amplified spontaneous emission also affects the cavity length through carrier density fluctuations which directly affect the index of refraction. Fluctuations in the index of refraction, which also results in modulation of the cavity length[72].

SNDP examined the timing jitter associated with several different semiconductor laser systems, which were potentially very compact and could be integrated with the other components forming the ADC system. Their jitters are summarized in the table below[74].

Table 5-1. Comparison of residual timing jitters among certain laser systems.

Laser System and Mode-locking Technique	RMS Timing Jitter
Active monolithic	530 fs
Passive monolithic	12.5 ps
Hybrid monolithic	1.13 ps
Active external	65 fs
Passive external	12.2 ps
Hybrid external	980 fs

As shown in Table 5-1, active external cavity lasers were reported to have the lowest timing jitter.   External cavity semiconductor lasers are composed of a semiconductor gain medium placed between two external mirrors. Active mode-locking refers to the placement of a shutter, such as an E-O modulator, within the laser cavity. An external frequency source then controls the opening and closing of the shutter allowing precise timing of the pulses within the cavity.   Active mode-locking also allows the precise repetition rate to be maintained even if multiple pulses propagate within the laser cavity, so this technique allows pulse repetition rates of tens of gigahertz to be routinely generated. Because of the small physical dimension of the semiconductor gain medium relative to the free-space length of the rest of the cavity, the temperature and refractive fluctuations are also smaller than those of a monolithic semiconductor laser. The resulting timing jitter is therefore low as well, being only several times greater than the 10 fs figure for a state-of-the-art electronic frequency synthesizer[75].

5.2 Contractual Laser Development with CREOL

Since the beginning of this effort, SNDP collaborated with Professor Peter Delfyett, of the University of Central Florida/School of Optics, to develop a compact, mode-locked

semiconductor diode laser with characteristics for ADC application. To better understand the noise properties of mode-locked lasers, he studied the supermodes, which produced the spurs shown at > 1 MHz in the left graph of Figure 5-1. The relationship between noise and cavity length can also be better understood when looking at that figure. Short cavities have higher fundamental frequencies and lower supermode noise, but they have higher phase noise, or timing jitter. Longer cavities have lower fundamental frequencies and lower phase noise (less timing jitter), but they exhibit higher supermode noise. Ideally a long cavity provides low fundamental frequency and low supermode noise, while the desired repetition rate is obtained by harmonically mode-locking the laser so that many pulses are simultaneously present in the cavity.
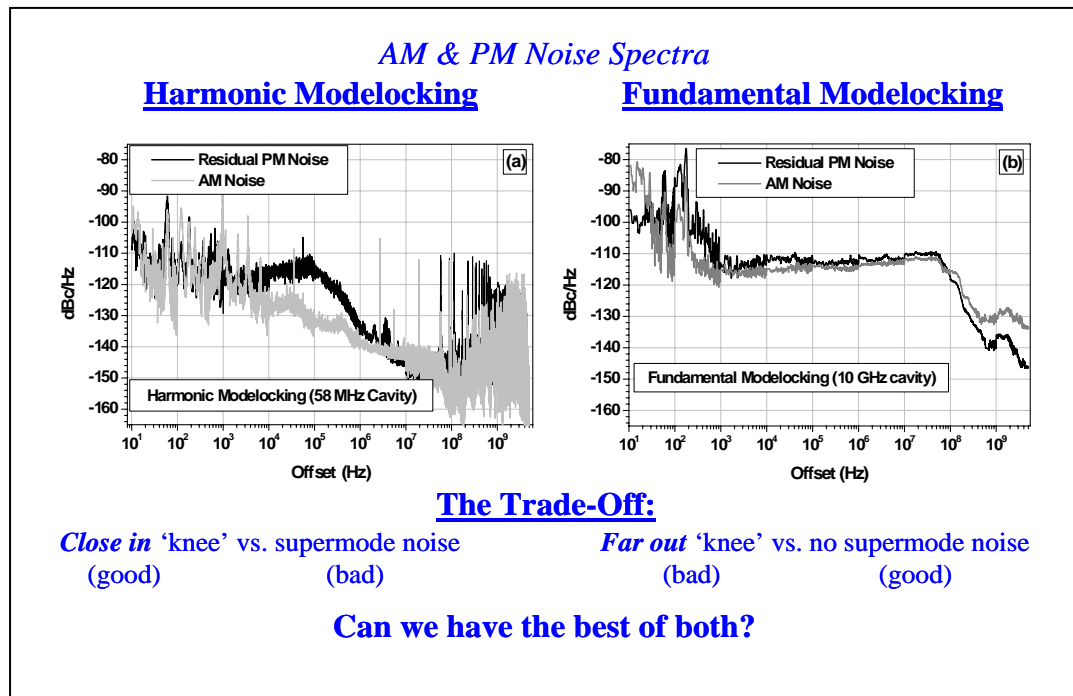
Figure 5-1. Phase noise comparison of harmonically and fundamentally mode-locked lasers and the trade-off between short and long cavity lengths[76].

The suppression effect in a long cavity is depicted in Figure 5-2. This laser demonstrated the lowest ever phase noise (jitter = 18 fs) and amplitude noise (0.05%) for an external cavity diode laser from 10 Hz to 10 MHz[76,77]. This performance would support nearly 10 bits of resolution. The supermode suppression was achieved by using a very narrow Fabry-Perot filter within the cavity. Professor Delfyett also successfully measured the phase noise side-bands to the Nyquist frequency of 5 GHz, whereas most research groups mathematically integrate only over the frequency range of interest, well short of the Nyquist value. Measuring results to the Nyquist value gives an extremely accurate representation of the overall noise present in the sampling system.
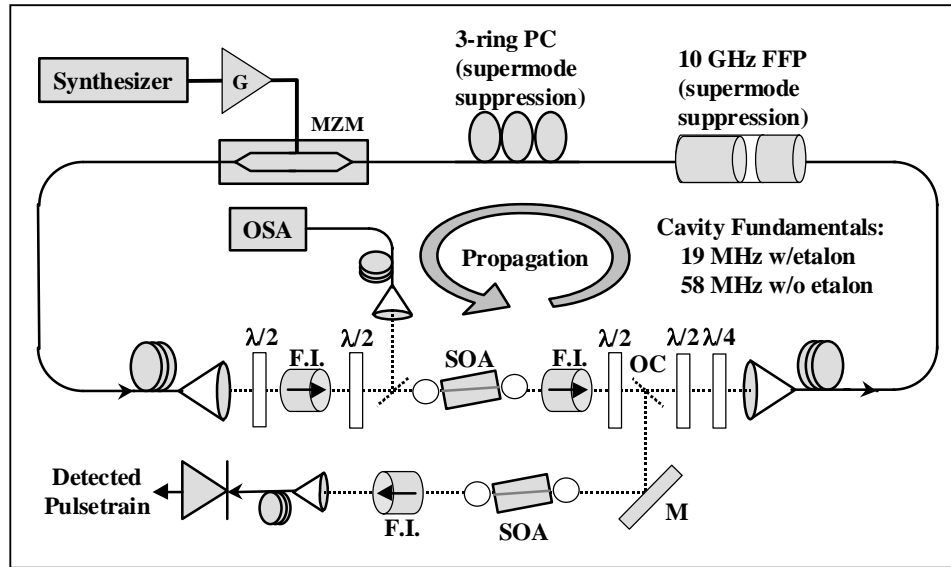
Figure 5-2. Schematic demonstration that a single laser diode could routinely generate optical sampling streams at 80 GS/s[76,77].

The productive collaboration with Peter Delfyett provided the in-house team with an in-depth understanding of the fundamentals of laser noise. More information on related efforts as well as details on those cited here is found in the final technical reports[76,78].

5.3 In-House Fiber Laser Development

5.3.1 Coupled Opto-Electronic Oscillator

SNDP has devoted considerable in-house effort to constructing erbium-doped fiber lasers (EDFLs)[79,80] of both active and passive mode-locked designs. The passively mode-locked laser incorporated a saturable absorber, but its 6 ps of timing jitter made it unsuitable for use in a photonic ADC system. New fiber laser designs based on active mode-locking had to be developed; one of these versions was a coupled opto-electronic oscillator (COEO), which is shown in Figure 5-3. The cavity was based on JPL's COEO design[81] and was shown to have low phase noise with sidemode suppression > 30 dB. No RF drive source is needed with a COEO design, which is extremely important when considering Air Force system size and power requirements.

The center frequency of the bandpass filter determined the laser mode-locked frequency. SNDP's COEO had an operating frequency of 10.0113 GHz, with a fundamental frequency of 7.55 MHz. When driven with an RF synthesizer, the optical ring cavity of the COEO produced an average output of 28 mW, with peak power of 90.6 mW for 15.9 ps pulses of 0.82 nm optical spectral width. The COEO was, however, unstable without the RF driver due to the RF filter's narrow passband ($f_{3dB} \sim 25$ MHz), which allowed multiple frequencies to simultaneously oscillate. When a second filter was incorporated to suppress the higher order frequencies that passed the RF filter, quasi-stable mode-locking was observed. The filter used was single-poled with a 3 dB width of 50 MHz. Being wider than the 25 MHz filter, it allowed more frequencies

to pass, but being single poled, it did not exhibit the problem of passing the higher order frequencies. This pre-filter stabilized the COEO by not allowing the higher order signals to reach the narrow 25 MHz filter, and in this configuration the filters had the desired effect. The drawback of using the two filters in combination was an extremely high loss in the RF leg of the COEO. The amplification required to restore those signals to the proper levels for modulation, added significant noise to the RF signal and increased instability in the laser. Better filters and amplifiers were needed to improve operation and to reduce the phase noise to a level comparable with Delfyett's actively mode-locked diode laser system.
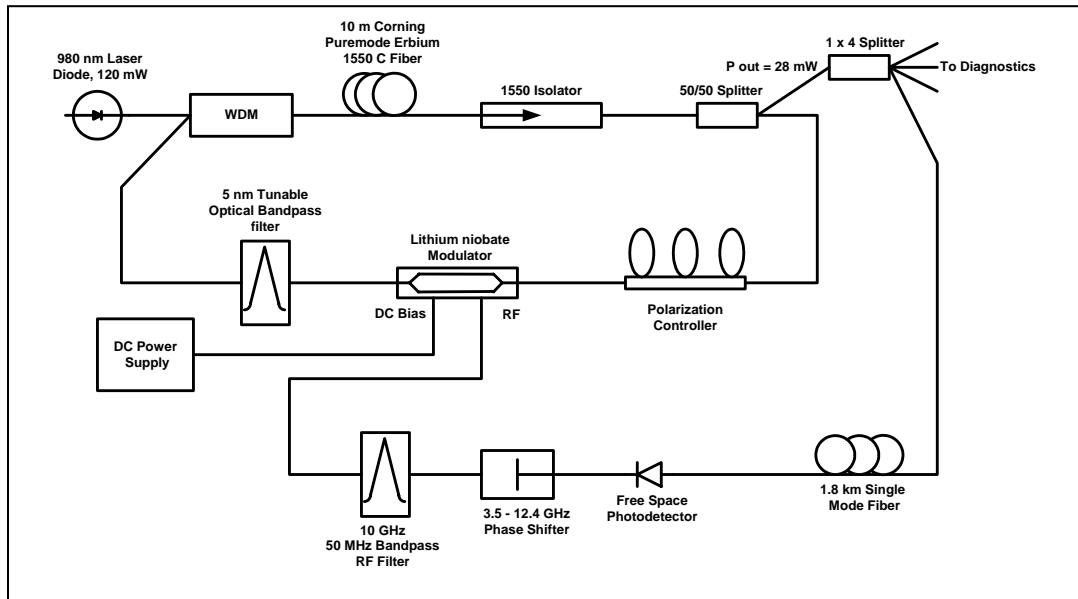
Figure 5-3. Schematic of a coupled opto-electronic oscillator (COEO).

5.3.2 High Concentration Er-Doped Fiber Laser

Fiber lasers have less low frequency phase noise due to their longer cavities and warrant further investigation even if they can not be directly integrated in a chip compatible format. The length (typically meters) of the erbium (Er)-doped fiber gain medium does add some complexity to the packaging; however, it can be reduced if the Er-ion concentration in the fiber is increased. Small devices also suffer less environmental effects, so the performance of an EDFL as a function of ion concentration within the gain medium was investigated. Results of mode-locked lasers with Lucent HE980, HG980, and HC Er-doped fibers were, therefore, compared with regards to output power as a function of length, concentration, pulse width, spectral bandwidth and phase noise.

The setup for the mode-locked ring laser is shown in Figure 5-4. A JDS Uniphase QLM95476 980 nm laser diode with 120 mW of optical output power pumped the gain medium through a 980/1550 nm wavelength division multiplexer (WDM). The Er-doped gain medium was fused to an OFR IO-H-IR2 1550 nm isolator to ensure unidirectional propagation in the cavity, and a 50/50 splitter served as the output of the cavity. A polarization controller was used to optimize the input polarization into the 20 GHz JDS Uniphase 10020465 lithium niobate modulator, which was used to mode-lock the cavity. A JDS Fitel TB1500B tunable bandpass filter with a 3 dB bandpass of 1.4 nm was used to control the operating wavelength, and the

output of the filter was fused back into the 1550 nm leg of the WDM to complete the ring cavity. Following the 50/50 output coupler, a 1x4 optical splitter was connected to various diagnostic instruments described as follows.

The average optical laser output was measured with Newport 835 power meter having an IR 818 detector. The optical spectrum was characterized using an Anritsu MS9701B optical unit with a MS9030A display unit set at a resolution of 0.1 nm. Pulse width was displayed by an Inrad 5-14-LD autocorrelation, and a high speed Antel DB-28 detector with 25 ps rise-time was used to observe the mode-locked pulse train. This split output was shown on an Agilent RF 8565 EC spectrum analyzer, while the other half was used to display the output pulses on a HP 54750A oscilloscope with a 54752A 50 GHz module and 54118A trigger box. The absolute phase noise of the laser was measured with an E5500 HP phase noise measurement system. The use of the RF spectrum analyzer in combination with the digital oscilloscope ensured that the laser was well mode-locked throughout the process.
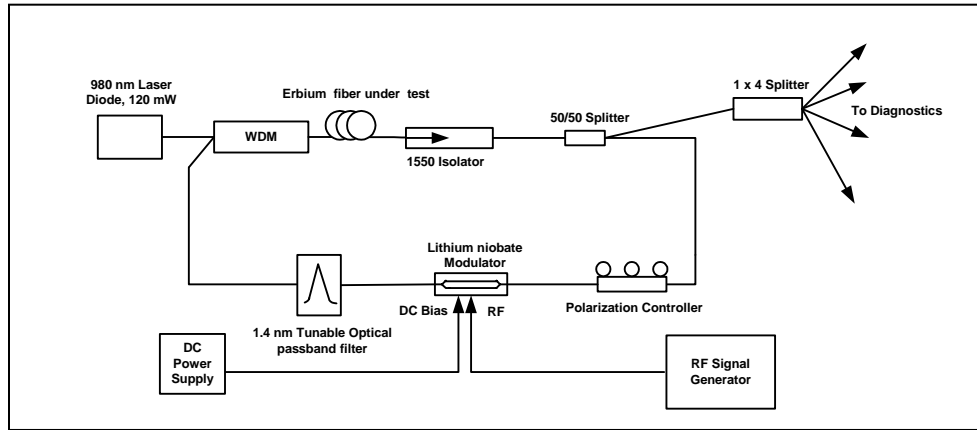
Figure 5-4. Mode-locked ring laser configuration using high concentration Er-doped fibers for the gain medium.

For each test the cavity configuration remained the same except for the three different Er-doped fibers with successively increased concentration of Er-ions. The fibers under test were Lucent Technologies HE980, HG980, and HC with Er-ion concentrations of $5.7 \times 10^{24}/m^3$, $26.5 \times 10^{24}/m^3$, and $60 \times 10^{24}/m^3$, respectively, with peak gains of 3.5 dB/m, 15.5 dB/m, and 55 dB/m near 1530 nm. The length of the gain medium was optimized for maximum output at 1550 nm and minimized for 980 nm output using the power meter. The fundamental cavity frequency was determined using the same RF spectrum analyzer. The laser was then mode-locked harmonically from 1 to 25 GHz at 1 GHz intervals, and the average optical power, optical spectral width, and auto-correlated pulse widths were recorded. Absolute phase noise measurements of the mode-locked laser were taken at 1, 5, and 10 GHz, as well as for the RF frequency synthesizer which was used to mode--lock the laser at 1, 5, and 10 GHz.

The first fiber under test was the HE 980, and for its concentration of Er it was found that a length of ~ 12.6 meters of fiber was optimal. The fundamental frequency was 8.68 MHz corresponding to a total cavity length of 23.04 m. The average output optical power before the 1x4 splitter was 28 mW at 10 GHz, corresponding to a peak pulse power of 137 mW, which was also typical of the entire mode-locked range of 1 to 25 GHz. Assuming a Gaussian pulse shape, the full width half max (FWHM) pulse width ranged from 66.45 to 14.14 ps. A plot of pulse width vs. mode-locking frequency is shown in Figure 5-5, and a typical optical pulse is shown later in this chapter. Assuming a Gaussian pulse shape, the time bandwidth product (TBP) was

0.486 at 10 GHz as compared to the theoretical value of 0.4413, which indicates pulsed performance approaching the TBP product limit.
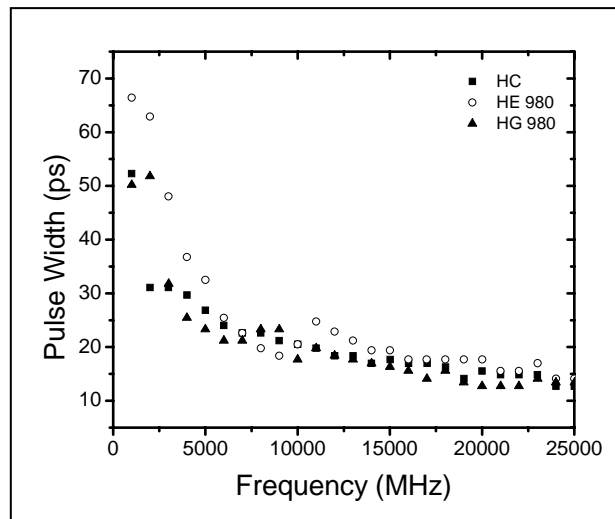
Figure 5-5. Pulse widths of the EDFLs for the three fibers under test.

The absolute phase noise of this laser at frequencies of 1, 5, and 10 GHz is shown in Figure 5-6.; this measurement method includes the noise contributed by the RF signal generator. The timing jitter calculated for the frequencies of 1, 5, and 10 GHz was, respectively, 17.11 ps, 2.42 ps, and 0.28 ps over a frequency offset of 10 Hz to 10 MHz for the HE980 fiber. The purpose of these measurements was to compare the performance of the different fiber laser media under operating conditions that were as similar as possible.
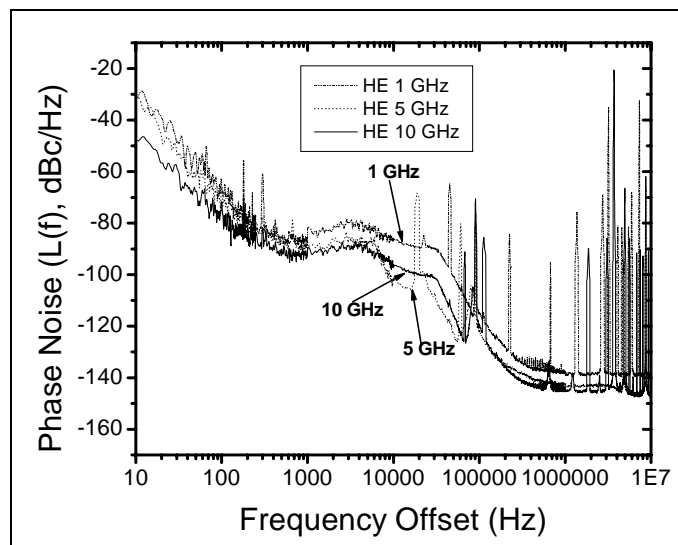
Figure 5-6. Absolute phase noise of the EDFL with HE 980.

The second fiber investigated was the HG 980 with a higher concentration of Er-ions; only ~ 3.88 meters of this fiber was needed for the gain medium, which yielded a fundamental cavity frequency of 13.97 MHz corresponding to a cavity length of 14.32 meters. The average output optical power before the 1x4 splitter was 14.44 mW at 10 GHz corresponding to a peak

pulse power of 81.6 mW. Assuming a Gaussian pulse shape, the FWHM pulse widths of this laser ranged from 50.2 to 12.7 ps (see Figure 5-5), with a time bandwidth product of 0.495 at 10 GHz. The absolute phase noise plot is shown in Figure 5-7. The timing jitter at the mode-locking frequencies of 1, 5, and 10 GHz was calculated to be 5.28, 0.53, and 0.35 ps, respectively.
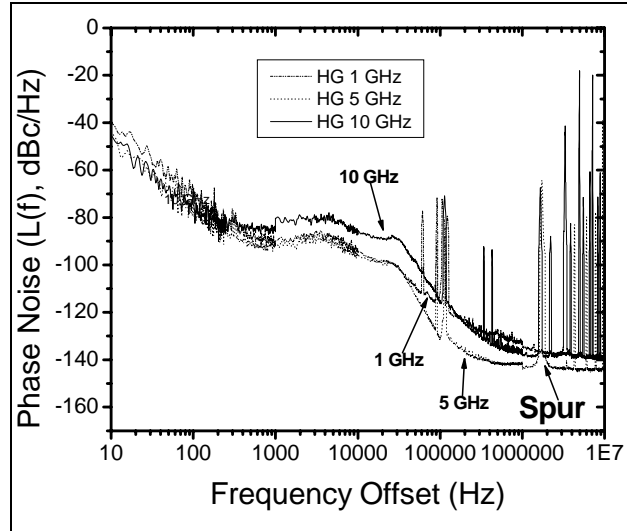
Figure 5-7. Absolute phase noise of the EDFL with HG 980.

The third medium tested was the HC fiber with approximately ten times the Er-ion concentration of the HE 980, so the optimum gain medium length was minimized at ~ 1.55 m. The fundamental cavity frequency for this was 16.68 MHz corresponding to a total cavity length of 11.99 m. The average output optical power before the 1x4 splitter in this case was 18.3 mW at 10 GHz, which yielded 89.3 mW peak pulse power. Again, an assumed Gaussian pulse shape with FWHM pulse widths ranging from 52.3 to 12.7 ps shown in Figure 5-5, indicated a time bandwidth product of 0.573 at 10 GHz. The absolute phase noise is shown in Figure 5-8 for the frequencies of 1, 5, and 10 GHz, and the corresponding timing jitters were calculated as 4.44 ps, 3.84 ps, and 0.62 ps, respectively.
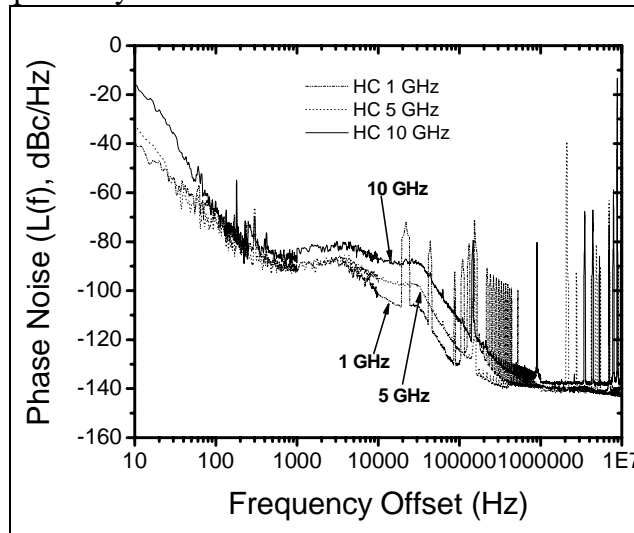
Figure 5-8. Absolute phase noise of the EDFL with HC.

To assess its contribution to the absolute phase noise measurement of the entire system, the signal generator alone was also measured, shown in Figure 5.9, so that its values could be subtracted for comparison purposes. Those results are indicated in summary in Table 5-2 by including jitter values for the HE980 laser before and after subtraction of the signal generator contribution. Subsequent measurements also made use of the residual phase noise option which effects the subtraction directly in the course of the measurement. That method was used for the erbium waveguide laser (EDWL) discussed in Section 5C3, so a direct performance comparison with the best of the three EDFLs could be made. The conclusions drawn from that are given in the final section of this chapter.

The noise spurs observed in the plots were removed from the calculated integration for the purposes of the performance comparisons, because the phase noise data acquisition at the time could not properly resolve narrow noise spikes, which yielded artificial contributions to the plot integration. Subsequent work in conjunction with Dr. Delfyett has clarified the issue more fully and established upper bounds to the actual contribution of noise spurs. Those were not essential to the purpose of the work described in this section, and the results summarized here met the accuracy required for the performance comparisons.
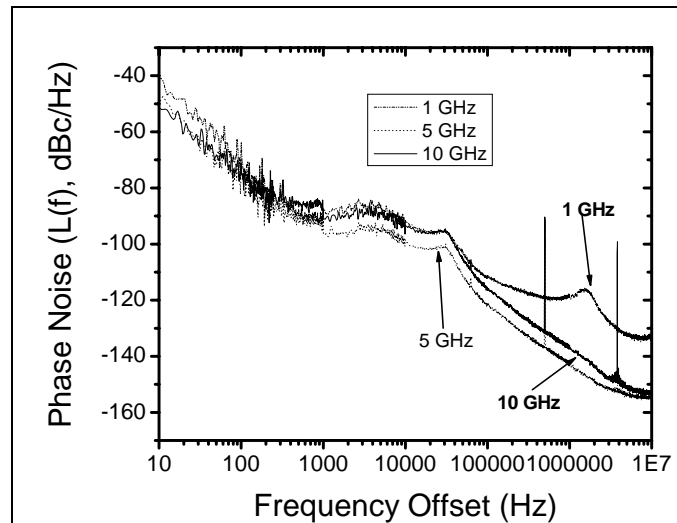
Figure 5-9. Absolute phase noise of the HP 83650 A.

In each of these EDFLs the average output optical power was consistent over the entire mode-locking range of 1 to 25 GHz. Power fluctuations up to 1 mW were observed with changes in the polarization state of the laser. When mode-locked well, the FWHM spectral width remained within 0.2 to 0.35 nm. A typical optical spectrum at a frequency of 10 GHz is shown in Figure 5-10; its relatively narrow spectral width is attributed to dispersion in the laser cavity.
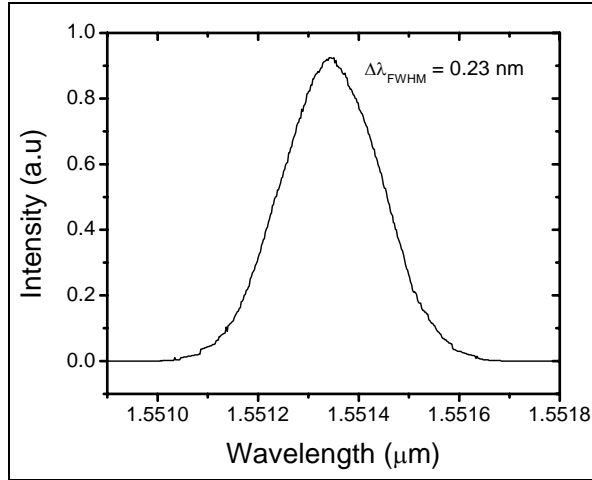
Figure 5-10. Typical optical spectrum of an EDFL at 10 GHz.

The RF spectrum of the EDFL also remained relatively constant for all three fiber types. As the mode-locking frequency was increased, the output signal power decreased. When the laser was optimally mode-locked, the side mode suppression ratio (SMSR) was greater than 50 dB, and no other cavity harmonics were observable. However, with this HC fiber it was more difficult to achieve complete suppression of the other cavity harmonics, particularly below 5 GHz. In those cases the SMSR was approximately 30 dB. A typical RF spectrum for the HC-EDFL mode-locked at 10 GHz is shown in Figure 5-11.
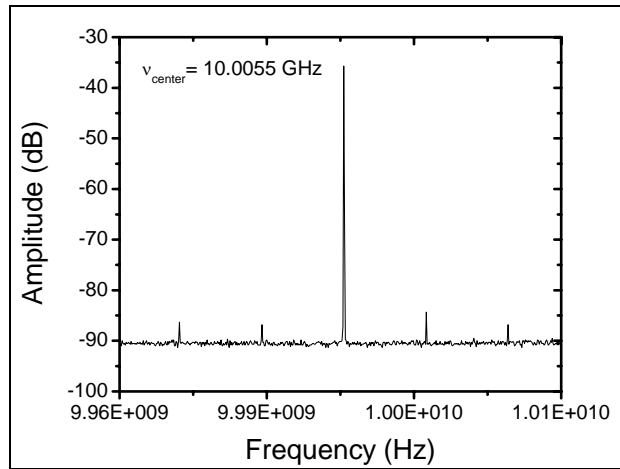
Figure 5-11. SMSR in the RF spectrum of EDFL at 10 GHz using HC fiber was typically less than that for fibers with lower concentrations.

The spectral shape of the pulse train output for all three Er-doped fibers was also similar from 1 to 25 GHz, but there were noticeable differences in the noise levels associated with those. The HC fiber produced a pulse train with greater amplitude and timing fluctuations than those for the HG980 and the HE980. As the mode-locking frequency was increased to 25 GHz, the pulses from all three types of fiber became noisier, and the amplitude of the pulse train

decreased. This was due to the modulator's bandwidth limit of 20 GHz and losses were increased as mode-locking frequencies approached or surpassed the bandwidth limits.

As expected, the pulse widths decreased as the mode-locking frequency increased, as shown in Figure 5-5. The lowest concentration Er fiber, the HE 980, at 1 GHz had the highest initial pulse width, whereas the HG 980 and the HC started at about the same pulse width. As the mode-locking frequency of the EDFL approached 25 GHz, the pulse widths of each laser converged to ~ 13 ps, which was likely limited by the dispersion remaining in the laser cavity. A typical pulse at 10 GHz as measured with an autocorrelator is shown in Figure 5-12, indicating a deconvolved pulse width was 22.4 ps.
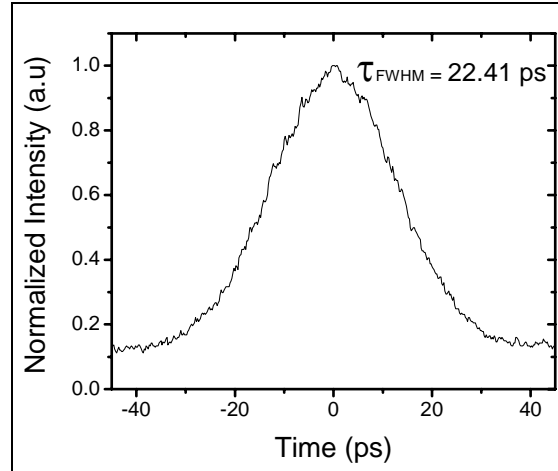
Figure 5-12. Typical auto-correlated pulse width of the EDFL at 10 GHz.

All of the EDFLs that were compared in this experiment also produced similar temporal pulse shapes. The average output optical power was less in the higher concentration fibers, but this was largely due to Er-ion absorption from incomplete pumping. The fibers' lengths were optimized to minimize this effect, but with the higher Er-ion concentration, a small length of un-pumped fiber induces a sharp increase in absorptive loss. Higher Er-ion concentration also decreased the stability as well as the ease of mode-locking, and the laser based on HC fiber required more cavity optimization to suppress other cavity harmonics. It also remained the most sensitive to changes in temperature, polarization or shock. This observation was also supported by higher timing jitter seen in the HC fiber at higher mode-locking frequencies. The time-bandwidth product also increased with Er-ion concentration, which is also associated with decreased stability. Despite increased instability with Er-ion concentration, mode-locking was nevertheless achieved with all three fibers over the range from 1 to 25 GHz.

A performance comparison of the EDFL with the three different fibers, summarized in Table 5-2, shows that all of them produced approximately the same final pulse widths as the mode-locking frequency approached 25 GHz. The gain medium's length was decreased as Er-ion concentration increased, thereby making the fundamental frequency higher. Though only 1.55 m of fiber was needed in the HC-EDFL, this laser exhibited the highest timing jitter for frequencies of 5 GHz and above. The large amount of up-conversion and spontaneous emission in this laser were likely responsible for the larger jitter. The stability of these lasers remains a critical issue, particularly when output power in the tens of milliwatts and pulse widths in the single picosecond range performance must be maintained. To address these issues, waveguide Er-doped amplifiers have more recently emerged as an integrated alternative to the meters of fiber

in conventional EDFAs.   However, to offer a viable alternative gain medium, Er-doped waveguide lasers would have to exhibit at least the same stability as conventional EDFLs.

Table 5-2. Summary of the performance characteristics of the EDFLs with each type of fiber.

Performance Characteristics		EDFLs	
	HE980	**HG980**	**HC**
Er-ion concentration	$5.7^{24}/m^3$	$26.5^{24}/m^3$	$60^{24}/m^3$
Length of Gain medium needed (m)	12.6	3.88	1.55
EDFL cavity fundamental frequency (MHz)	8.68	13.97	16.68
Average output power at 10 GHz (mW)	28	14.44	18.3
Maximum FWHM pulse width (ps)	66.45	50.2	52.3
Minimum FWHM pulse width (ps)	14.14	12.7	12.7
Timing Jitter at 1 GHz (ps) {signal generator subtracted}	17.11 {1.25}	5.28	4.44
Timing Jitter at 5 GHz (ps) {signal generator subtracted}	2.42 {1.97}	0.53	3.84
Timing Jitter at 10 GHz (ps) {signal generator subtracted}	0.28 {0.06}	0.35	0.62
Time-bandwidth product at 10 GHz	.486	.495	.573

5.3.3 Harmonically Mode-Locked Erbium-Doped Waveguide Laser

With recent advances in multi-component glass production, higher doping concentrations can be achieved than with simple silicate glasses. In particular, newly developed Er-doped multi-component glass waveguide permits significant reduction to the overall footprint of the gain medium. SNDP constructed a novel harmonically mode-locked fiber ring laser using the Er-doped multi-component glass waveguide from Inplane Photonics Inc. as the gain medium.

The setup for the mode-locked waveguide laser is shown in Figure 5-13. A Corning Lasertron CLT3 980 nm laser diode with 200 mW of optical output power pumped the Er-doped glass waveguide through an integrated 980/1550 nm wavelength division multiplexer (WDM). The waveguide device had an active length of 25 cm, an Er concentration of $1x10^{20}$ Er-ions/cm^3, and was pigtailed with singlemode fiber to allow efficient splicing into the ring cavity. The output of the waveguide was fused to an OFR IO-H-IR2 1550 nm isolator to ensure unidirectional propagation in the cavity. A 90/10 splitter served as the output of the cavity and provided enough feedback to compensate for cavity losses. An in-line Newport F-POL-IL polarization controller controlled the input polarization into the 20 GHz JDS Uniphase 10020465 lithium niobate modulator, which provided the mode-locking mechanism. A JDS Fitel TB1500B tunable bandpass filter with a bandpass of 1.4 nm controlled the operating wavelength. The output of the filter was fused back into the 1550 nm leg of the integrated WDM to complete the ring cavity. Following the output coupler, a Pritel FA-15 Er-doped fiber amplifier amplified the output sent to a 1x3 optical splitter and diagnostic equipment.
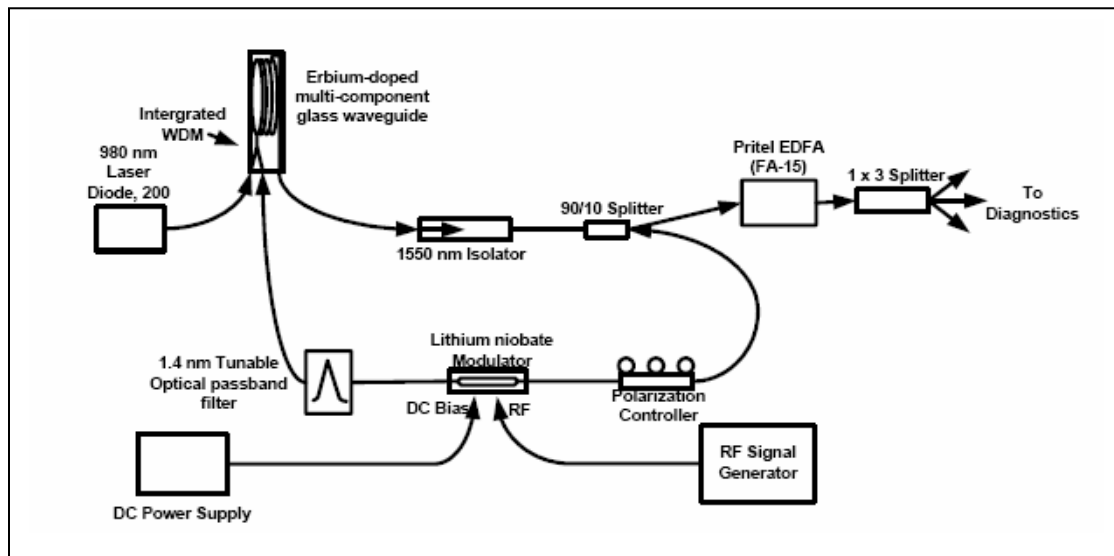
Figure 5-13. Schematic of the actively mode-locked EDWL.

The average output optical power was measured using a Newport 1835 C power meter with an IR 818 detector. The optical spectrum of the laser was characterized using an Anritsu MS9701B optical unit with a MS9030A display unit set at a resolution of 0.1 nm. The pulse width was measured with an Inrad 5-14-LD autocorrelator. A high speed Discovery Semiconductor DSC30S detector with 22 GHz bandwidth was used to detect the signal sent to the HP E5504 phase noise measurement system, and a New Focus 1444 optical detector was used to detect one of the other outputs of the 1x3 optical splitter. The detected signal was split and sent to an Agilent E4448A RF spectrum analyzer, while the other portion was displayed in the form of output pulses on an HP 54750A oscilloscope with a 54752A 50 GHz module. The use of the RF spectrum analyzer in combination with the digital oscilloscope ensured that the laser was well mode-locked. The single sideband residual phase noise of the laser was measured with the previously mentioned HP phase noise measurement system.

The gain spectrum of the waveguide was measured using a New Focus 6200 tunable laser shown in Figure 5-14. The Er-doped glass waveguide used as the gain medium for this laser has a saturated output power of 10 dBm. A 90/10 output coupler was used in the cavity to provide enough feedback to the cavity to compensate for cavity losses. The laser had a fundamental frequency of 15 MHz with an average output power of ~ 250 μW which corresponded to peak pulse power of 1.14 mW at a 10 GHz mode-locking rate. The optical spectrum of the EDWL remained constant in shape as the laser was mode-locked from 1 to 20 GHz. When properly mode-locked, the full width half max (FWHM) spectral width ranged from 0.09 to 0.25 nm. At 3 and 10 GHz the corresponding FWHM optical spectral widths were 0.096 and 0.228 nm, respectively. Assuming a Gaussian pulse shape, the FWHM of the pulses ranged from 160 ps at 1 GHz to 9.9 ps at 20 GHz. A plot of pulse width as a function of mode-locking frequency, data taken from the digital oscilloscope up to 3 GHz and from the autocorrelator in the range of 3 GHz to 20 GHz, is shown in Figure 5-15. Assuming a Gaussian pulse shape, the corresponding time bandwidth products were 0.503 and 0.523 at 3 and 10 GHz, respectively, as compared to the ideal value of 0.4413 indicating a small amount of dispersion in the cavity, which does not affect the primary performance parameters.
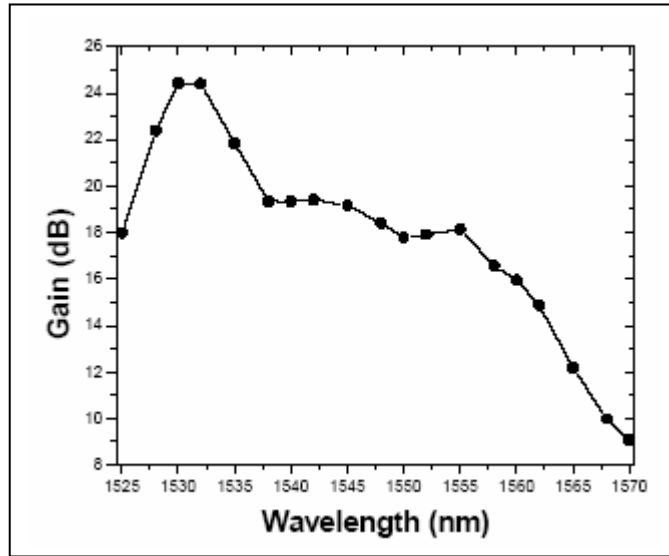
Figure 5-14. Gain spectrum of the Er-doped waveguide.
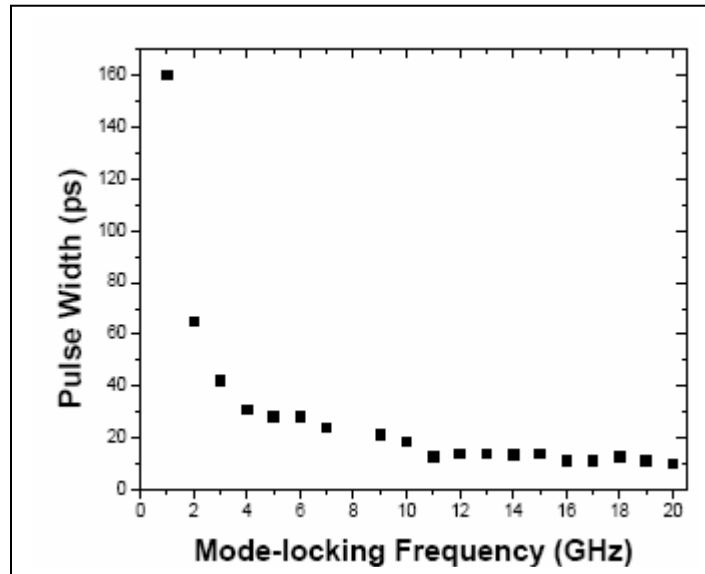
Figure 5-15. Pulse width vs. mode-locking frequency for the EDWL.

The waveform shape and RF spectrum of the EDWL remained fairly consistent as the laser was mode-locked from 1 to 20 GHz. The level of noise on the waveform did increase slightly with increased mode-locking rate, but the noise did not compromise the shape of the pulses. As the mode-locking frequency was increased, the signal decreased in amplitude. This was most likely due to the increased loss of the lithium niobate modulator as the mode-locking frequency surpassed the 3 dB frequency cut-off at 16 GHz. When the laser was optimally mode-locked, the harmonic suppression was greater than 50 dB. Typically, harmonic suppression within the laser was ~ 30 to 45 dB and is shown in Figure 5-16. The harmonic suppression, the

stability of the mode-locked pulse train, and the optical spectral width were useful indicators as to how well the laser was mode-locked.
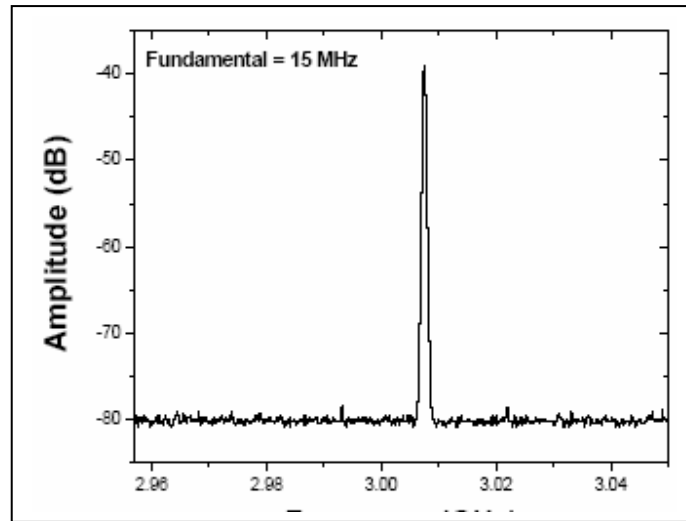
Figure 5-16. RF spectrum of the EDWL mode-locked at 3 GHz showing harmonic suppression of approximately 40 dB.

The single side band residual phase noise of this laser at the frequencies of 3 and 10 GHz is shown in Figure 5-17. Residual phase noise measurements take into account the actual phase noise within the laser itself; any external sources that contribute to the absolute phase noise, such as the frequency synthesizer, are calibrated out in this measurement. The timing jitter calculated for the frequencies of 3 and 10 GHz were 0.048 ps and 0.028 ps respectively, over a frequency offset of 10 Hz to 10 MHz. The large relaxation oscillation peak present in the residual phase noise plot for 3 GHz was due to the laser switching modes during the measurement. This peak contributed somewhat to the timing jitter calculated for 3 GHz, and was later reduced further by adding a piezo-electric (PZT) controller with a feedback loop to control the cavity length as it changes with temperature. A Fabry-Perot etalon suppresses any supermodes above the cavity fundamental and thereby also reduces timing jitter.
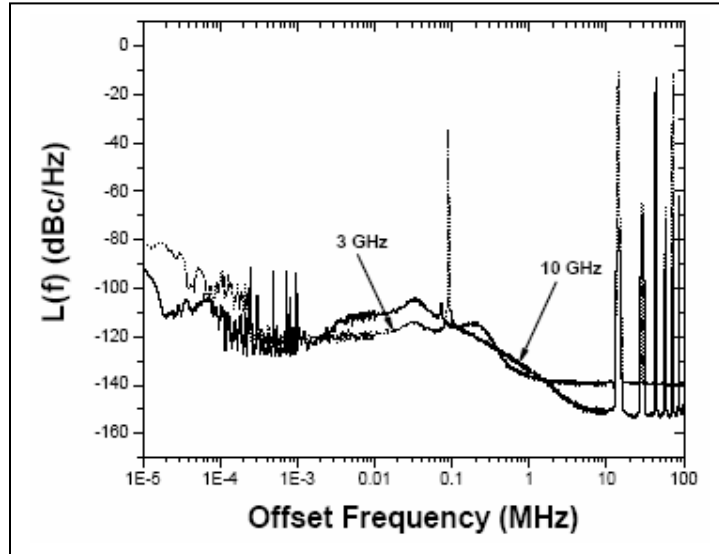
Figure 5-17. Single sideband residual phase noise for the EDWL mode-locked at 3 and 10 GHz.

External cavity lasers were studied contractually and in-house because of their potential for low phase noise level; however, in general fiber lasers still have the lowest reported jitter[82]. High concentration fiber was considered to reduce the cavity size, but it was also harder to mode-lock and had more noise. An Er-doped waveguide laser was mode-locked from 1 to 20 GHz and had an output power of ~ 250 μW. This laser produced stable picosecond pulses with harmonic suppression on the order of 40 dB, and the very low timing jitter (mode-locked at 10 GHz) was 28.3 fs over a frequency offset of 10 Hz to 10 MHz. It is shown in Table 5-2 that this exceeds the 60 fs timing jitter of the best in-house performing EDFL. The use of this low jitter laser as a sampling source in a photonic ADC system would provide a maximum theoretical resolution of 10.14 bits, which exceeded the performance of conventional electronic sampling. Both stability and timing jitter in an EDWL were superior to that of the doped erbium fiber lasers with higher up-conversion and ASE. The overall physical size of the EDWL also makes it much more practical for use on an air/space platform.

Radiation effects on components and systems become important when they move from a lab bench and into field systems. SNDP investigated and reported these effects on lasers[83-86]; however, laser stability was the focus of primary interest in this work. Low phase noise is a requirement that pertains not only to optical sampling, but also to many other applications such as optical arbitrary waveform generation.

Chapter 6. Discussion and Conclusions

Analog-to-digital converters are critical components for developing the next generation of advanced digital receivers. Wide bandwidth and high resolution ADCs would allow direct sampling of the sensor signal at RF frequencies, and eliminate the need for analog down conversion. The performance of photonic ADCs in terms of sampling speed and resolution could far surpass that of any state-of-the-art electronic ADCs; however significantly more research effort is required before a fully functional prototype system can be realized. SNDP examined some of the proposed photonic ADC systems and determined that they were largely impractical. Using the perspective acquired from that experience a system was designed that would address particular Air Force platform requirements for system integration and low power consumption. The proposed photonic ADC required three component sub systems to be concurrently developed and tailored: ML laser sources, EAM encoders, and quantizers based on optical SA technology. Each offered potential performance enhancement to exceed that of electronic systems, but also entailed challenging problems for practical realization. These subsystems and their possibilities for further development are summarized.

6.1 Discussion

An inherent drawback to some photonic approaches is the fact that alignment can require precise positioning and orientation to remain stable for long time intervals. "Pigtailing" a fiber to a laser for example, is considerably more difficult, and costly, than bonding wire to a chip[87]. However, with proper engineering and design certain optical systems can be integrated to the extent that alignment is not an issue, and the systems also become more compact and robust. It is for this reason the ADC system and its components were designed with that perspective from inception throughout the process. At the integrated stage other factors such as signal cross-talk at the device level can take on more importance.

The temperature and heating fluctuations that pose challenges to photonic-based systems can be categorized as ambient or localized effects. The ambient temperature changes affect temperature dependent parameters such as absorption coefficient, band edge, and active device dimensions. Use of thermo-electric controllers (TEC) with feedback could be successfully applied to both the EAM and SA devices to compensate for their internal heat generation. The localized thermal effects, also referred to as point source heating are much more difficult to control. The heating effects[88] in the EAMs and the SAs and the resulting band edge shifts can be large enough for the degradation to render them inoperable. Excess heating can breakdown the electronic circuitry when excess current is generated by the incident light. Even a non-catastrophic build up of carriers screens the bias applied and raises the effective value of V_π. A higher V_π is problematic for the system: high rate voltage change at modulator electrodes increases the slew rate requiring LNAs with very high gain, bandwidth and linearity, and thereby transfers difficulties to another part of the system.

For the saturable absorber, any temperature shift of band edge can require a change of threshold in the detector/comparator optoelectronic portion of the quantizer. Since the absorbers are passive, electronic circuitry breakdown is not a concern, and intensities exceeding a GW/cm^2 in 120 fs pulses did not prevent operation. Although these effects cannot be eliminated, they are mitigated by sufficiently reducing the incident optical power or the operating EAM voltage.

The operational key to the ADC operation, the all optical quantizer, entailed limitations. One advantage of optical sampling is that the signal can be sampled in real time by the modulator, and not by electronic means. In principle the use of optical pulses for the sampling could allow elimination of the "sample and hold" function, but in practice photonic ADC development must be realized in stages, which require the optical "sample and hold" detailed in section 3C2. If the saturable absorber transfer function were "ideal", (0 to 100% transmission over a narrow range of input power), then the optics adds effective "gain" to the electrical comparator function. Larger gain lowers effective aperture uncertainty, reducing the chance that the comparator makes a wrong decision (1 vs. 0). But, if the transfer functions are "soft" as discussed in Chapter 3 with slow variance in transmission from ~ 30% to ~ 40% for a wide range of input power, then the input optics "reduce" the comparator gain below what could have been achieved by the electrical ADC alone.

The multi-path or parallel flash nature of this ADC architecture posed another challenge. As in electronic flash ADCs, 2^N-1 channels are required, where N is the stated resolution. Flash architectures require a large number of channels to achieve even a moderate resolution, and the ultimate bandwidth of the ADC system may be limited by the electronics following the optical detectors. For example, if the optical sampling pulses are narrow with insufficient energy, then the electronic comparators will not function properly, and speed is sacrificed in compensating for this with electronics. Alternatively, for a given number of bits and for given losses, shot noise limits the maximum bandwidth. In practice a quantizer-SA based system could be limited to a small number of bits such as 4 to 7. In that case the bandwidth would need to be high enough (> 10 GHz at 7-8 bits) to be of practical interest and also exceed electronic capabilities. For the case of N effective bits, and to overcome shot noise and quantize the amplitude of the optical pulses, there must be at least 2^N photons present at the input of the optical splitter, beyond losses due to splitting, SAs, and limited photodiode efficiency. With splitter losses proportional to the number of branches (2^N -1), the optical power requirement is high and increases rapidly with N. This poses problems for switching at the high clock speeds of interest. The fabrication of the splitters and SAs for approximately 100 branches (for ~ 7 bits) is not straightforward when uniformity and precise control of the absorber saturation points must be maintained. Related waveguide splitting has achieved that magnitude, 1x128,[89] but not yet with modulation capability incorporated.

6.2 Implications

The saturable absorber design in this system posed a particularly difficult problem in that the "slope" response of the present state-of-the art was not sufficient for the desired quantizer performance. A solution was to incorporate a bistable waveguide saturable absorber etalon to enhance high contrast ultra-fast switching required for the analog data acquisition. The preliminary test results in conjunction with Sarnoff Corp. confirmed that the approach was promising and that the slope enhancement of more than an order of magnitude would have supported the ~ 7 bit number. The work required to tailor the sensitive control of the devices could not be completed during the project, but the test results obtained during that process contributed significantly to the development of both SA and MQW-EAMs.

The semi-conductor modulator used to encode the analog signals provided the most suitable choice in terms of extremely compact size, simplicity of fabrication, and most critically, full integration compatibility with waveguide and diode based devices. The prototypes provided in the course of the work by Professor Yu's UCSD group demonstrated an improvement of

nearly 20 dB/Hz$^{2/3}$ over the state-of-the-art at the time the program was initiated. The SFDR of > 110 dB/Hz$^{2/3}$ for broadband use demonstrated the linearity needed for most of the ADC dynamic range requirements. That development work is continued by SNDP and will result in fully packaged devices to be tested in working analog links.

Er-doped waveguide lasers and external cavity mode-locked semiconductor lasers were thoroughly investigated for use as the ADC source; their temporal resolution and stability were the key performance characteristics which ultimately dictated their selection. The latter of these two systems (developed at UCF) demonstrated high temporal stability, while the EDWL system developed by SNDP approached that performance in a configuration that eliminated free-space optics entirely from the laser cavity. Its final short term temporal stability would have sustained the desired ~ 7 bits/10 GHz goal, but design changes were required to make the system more stable long term, and eliminate adjustment or calibration during operation. The EDWL had a very compact gain medium and all of its components were either integrated or in optical fiber. In its final assembled form such a system would be suitable to meet the size constraints but would need further packaging to adequately assess the environmental robustness. The latter tests would have to be pursued in future work, and some component modifications could still be required. The remarkable progress toward ultra low phase noise and temporal stability applies not only to the sampling applications discussed here, but also to ultra-precision optical frequency comb and arbitrary waveform generation.

It is clear that the ADC system entails the functional integration of the SA, EAM, and ML laser subsystems. Central to the operation is the photonic quantizer, which was initially based on SA devices and subsequently changed to bistable waveguide SA versions. From the observed and projected performance of the components, it can be concluded that the EDWL and EAM devices reached a stage which would permit at least a prototype's short term performance to exceed that of electronics. The other key component, the SA etalon, did not reach that stage so no prototype was possible. However, later observations demonstrated the required nonlinear bistability with a suitable slope response in a waveguide configuration, although they could not be investigated in depth before the project work was completed. If future work were to be pursued in this field, control of such bistable devices would provide a productive starting point. It is clear that although the completion of this project did not yield the ultimate goal of a working ADC prototype, the progress in the sub-system component development contributed to and advanced the state-of-the-art in several critical areas. These included EAM, SA and low noise ML lasers, all of which have many potential applications to AF needs.

References

1. Robert H. Walden, "Analog-to-Digital Converter Survey and Analysis", *IEEE Journal on Selected Areas in Communications*, Vol. 17, No. 4, April 1999, pp. 539-550.

2. Robert H. Walden, "Performance Trends for Analog-to-Digital Converters", *IEEE Communications Magazine*, Feb. 1999, pp. 96-101.

3. "Boeing: Products-E-3 AWACS in Service Worldwide", http://www.boeing.com/defense-space/infoelect/e3awacs/index2.htm

4. Ahmet Kahraman, *Multimission Aircraft Design Study, Payload*, Air Force Institute of Technology Thesis, Mar 2003, pp. 2-5 – 2-31.

5. Adam J. Hebert, "Command From the Air", *Air Force Magazine*, Vol. 86, No. 8, Aug 2003, pp. 70-73.

6. Congressman Rick Larsen, D-WA, "Electronic Warfare: A Critical Asset", *Military Aerospace Technology*, Vol. 4, Issue 3, Oct 20, 2005.

7. Congressman Joseph R. Pitts, "Electronic Warfare: Protecting and Enabling Our Forces", Electronic Warfare Working Group, IDGA Air Survivability Conference, April 28, 2004

8. Defense Science Board Task Force, *Future DoD Airborne High-Frequency RADAR Needs/Resources*, April 2001.

9. "U-2 high Altitude Reconnaissance Aircraft (Dragon Lady), USA", http://www.airforce-technology.com/projects/u2/

10. "JSF (F35) Joint Strike Fighter, International", http://www.airforce-technology.com/projects/jsf/

11. "AN/APG-81 Multimode Radar for the F-35 Joint Strike Fighter", Jane's Avionics, 19-Aug-2005, http://www8.janes.com/Search/documentView.do?docId=/content1/janesdata/yb/jav/jav_9782.htm@current&pageSelected=allJanes&keyword=F-35%2019-Aug-2005&backPath=http://search.janes.com/Search&Prod_Name=JAV&

12. "Lockheed Martin F-35 Joint Strike Fighter", Jane's All the World's Aircraft, 07-Mar-205, http://www8.janes.com/Search/documentView.do?docId=/content1/janesdata/yb/jawa/jawa1347.htm@current&pageSelected=allJanes&keyword=F-35%20%2007-Mar-2005&backPath=http://search.janes.com/Search&Prod_Name=JAWA&

13. "Discoverer II (DII) Starlite", GlobalSecurity.org, 24-Sept-2005, http://www.globalsecurity.org/space/systems/discoverer2.htm

14. Sec. of Defense William S. Cohen and Gen. Henry H. Shelton, "Joint Statement on the Kosovo After Action Review", presented to the Senate Armed Services Committee, 14 Oct 1999, http://www.defenselink.mil/releases/1999/b10141999_bt478-99.html

15. Statement of James G. Roche (Secretary of the Air Force) and John P. Jumper (Chief of Staff, Dept. of the Air Force), Statement made to House Armed Services Committee on Fiscal Year 2003 National Defense Authorization Budget Request, March 6, 2002, http://www.house.gov/hasc/openingstatementsandpressreleases/107thcongress/02-03-05rochejumper.html

16. James Murphy, "Development of High Performance Analog-to-Digital Converters for Defense Applications", *19th IEEE GaAs IC Symp. Tech. Dig.*, Oct 1997, pp. 83-86.

17. Kevin R. Nary, Randy Nubling, Steve Beccue, William T. Colleran, James Penney, Keh-Chung Wang, "An 8-Bit, 2 Gigasample Per Second Analog to Digital Converter", *17th IEEE GaAs IC Symp. Tech. Dig.*, Oct. 1995, pp. 303-306.

18. Gopal Raghavan, Joseph. F. Jensen, Robert. H. Walden, and William P. Posey, "A Bandpass $\Sigma\Delta$ modulator with a 92 dB SNR and Center Frequency Continuously Programmable from 0 to 70 MHz", *ISSCC Tech Dig.*, Vol. 40, Feb 1997, pp. 214-215.

19. Henry F. Taylor, "An Optical Analog-to-Digital Converter-Design and Analysis", *IEEE J. of Quantum Electronics,* Vol. QE-15, No. 4, April 1979, pp. 210-216.

20. Rick A. Philpott, "Development of high Performance Electronics and optical-to-Electrical Advanced Circuitry for Photonic Analog-to-Digital Converters", *AFRL-SN-RS-TM-2006-1,* February 2006.

21. Josef Sauerer, Frank Oehler, Günter Rohmer, Ulrich Schlag, "GaAs for ADCs: System Needs and Device Requirements", *16th IEEE GaAs IC Symp. Tech. Dig.*, Oct. 1994, pp. 220-223.

22. Daniel Senderowicz, Germano Nicollini, Sergio Pernici, Angelo Nagari, Pierangelo Confalonieri, Carlo Dallavalle, "Low-Voltage Double-Sampled $\Sigma\Delta$ Converters", *IEEE International Solid-State Circuits Tech. Dig.*, 1997, Paper FR 13.2, pp. 210-211.

23. "A Simple ADC Comparison Matrix," Maxim Application Note 2094, Jun 02, 2003, http://pdfserv.maxim-ic.com/en/an/AN2094.pdf

24. "Pipeline ADCs Come of Age", Maxim Application Note 634, March 21, 2000, http://pdfserv.maxim-ic.com/en/an/AN634.pdf

25. Yutaka Matsuoka and Eiichi Sano, "High-Speed AlGaAs/GaAs HBT's and Their Applications to 40 Gbit/s-Class IC's", *16ᵗʰ IEEE GaAs IC Symp. Tech. Dig.*, Oct. 1994, pp. 185-188.

26. Takatomo Enoki, Takashi Kobayashi, and Yasunobu Ishii, "Device Technologies for InP-Based HEMTs and Their Application to ICs", *16ᵗʰ IEEE GaAs IC Symp. Tech. Dig.*, Oct. 1994, pp. 337-340.

27. S. Yamahata, K. Kurishima, H. Nakajima, T. Kobayashi, and Y. Matsuoka, "Ultra-High F_{max} and F_t InP/InGaAs Double Heterojunction Bipolar Transistors with Step-Graded InGaAsP Collectors", *16ᵗʰ IEEE GaAs IC Symp. Tech. Dig.*, Oct. 1994, pp. 345-348.

28. H. F. Chau and Y. C. Kao, "High F_{max} InAlAs/InGaAs Heterojunction Bipolar Transistors", *IEDM Tech. Dig.*, Dec. 1993, pp. 783-786.

29. J. I. Song, Brian W. P. Hong, Chris J. Palmstrom, and K. B. Chough, "InP Based Carbon-Doped Base HBT Technology: Its Recent Advances and Circuit Applications", *IEEE Indium Phosphide and Related Materials Conf. Proc.*, March 1994, pp. 523-526.

30. Tom P. E. Broekaert, Willie W. Ng, J. F. Jensen, Daniel Yap, d. L. Persechini, S. Bourgholtzer, Charles H. fields, Young K. Brown-Boegeman, Binqiang Shi, and Robert H. Walden, "InP-HBT Optoelectronic Integrated Circuits for Photonic Analog-to-Digital Conversion", *IEEE J. Solid-State Electronics*, Vol. 36, No. 9, Sep. 2001, pp. 1335-1342.

31. J. C. Candy and G. C. Temes, Eds., *Oversampling Delta-Sigma Data Converters*, New York: IEEE Press, 1992, Introduction.

32. J. F. Jensen, G. Raghavan, A. E. Cosand, and R. H. Walden, "A 3.2 GHz Second Order Delta-Sigma Modulator Implemented in InP0 HBT Technology", *IEEE J. Solid-State Circuits*, Vol. 30, No. 10, Oct. 1995, pp. 1119-1127.

33. F.W. Singor and W. M. Snelgrove, "Switched Capacitor Bandpass Delta-Sigma A/D Modulation at 10.7 MHz", *IEEE J. Solid-State Circuits*, Vol. 30, Mar. 1995, pp. 184-192.

34. Arun Jayaraman, Peter Asbeck, Kevin Nary, Steve Beccue, and Keh-Chung Wang, "Bandpass Delta-Sigma Modulator with 800 MHz Center Frequency", *19ᵗʰ IEEE GaAs IC Symp. Tech Dig.*, Oct. 1997, pp. 95-98.

35. Paul. W. Juodawlkis, Jonathan C. Twitchell, Gary E. Betts, Jeffrey J. Hargreaves, Richard D. Younger, Jeffrey L. Wasserman, Frederick J. O'donnell, Kevin G. Ray, and Richard C. Williamson, "Optically Sampled Analog-to-Digital Converters", *IEEE Transactions on Microwave Theory and Techniques*, Vol. 49, No. 10, Part 2, Oct. 2001, pp.1840 – 1853.

36. R.C. Williamson, P. W. Juodawlkis, J. L. Wasserman, G. E. Betts, and J. C. Twichell, "Effects of Crosstalk in Demultimplexers for Photonic Analog-to-Digital Converters", *J. of Lightwave Technology*, Vol. 19, No. 2, Feb 2001, pp. 230-236.

37. W. Ng, L. Luh, D. Persechini, D. Le, Y. M. So, M. Mokhtari, C. Fields, D. Yap, and J. Jensen, "Ultra-High Speed Photonic Analog-to-Digital Conversion Technologies", *SPIE Proceedings*, Vol. 5435, 2004, pp. 171-177.

38. W. Ng, L. Luh, D. Yap, W. Bridges, M. Mokhtari, J. Jensen, C. Fields, and Y. M. So, "Photonic Analog-to-Digital Conversion Technology, *AFRL-SN-RS-TR-2004-347*, December 2004.

39. Eric Donkor, "A 10-Bit 10 GSPS Optical ADC for Radar Signal Processing", *AFRL-SN-RS-TR-2003-271*, November 2003.

40. Henry Zmuda, "Optically Assisted High-Speed, High Resolution Analog-To-Digital Conversion", *AFRL-SN-RS-TR-2005-154*, April 2005.

41. Michael J. Hayduk, *Passively Mode-Locked Erbium-Doped Fiber Lasers Using Multiple Quantum Well Saturable Absorbers,* Cornell University Ph.D. Dissertation, Aug. 1997.

42. T. Sizer, II, T. K. Woodward, U. Keller, K. Sauer, T.-H Chiu, D. L. Sivco, and A. Y. Cho, "Measurement of Carrier Escape Rates, Exciton Saturation Intensity, and Saturation Density in Electrically Biased Multiple-Quantum Well Modulators", *IEEE J. Quantum Electron.*, Vol. 30, No. 2, Feb. 1994, pp. 399-407.

43. D. Cohen, *Femtosecond Relaxation of Electrons in the Conduction Band of InGaAs,* Cornell University Ph.D. Dissertation, 1995.

44. D. A. Humphreys, R. J. King, D. Jenkins, and A. J. Moseley, "Measurement of Absorption Coefficients of $Ga_{0.47}In_{0.53}As$ Over the Wavelength Range 1.0-1.7 μm", *Electron. Lett.*, Vol. 21, 1985, pp. 1187.

45. J. P. Theimer, M. Hayduk, M. Krol, and J. W. Haus, "Mode-locked Cr^{4+}:YAG Laser: Model and Experiment," *Optics Communications*, Vol. 142, pp. 55-60, 1997.

46. M. J. Hayduk, S. T. Johns, M. F. Krol, C. R. Pollock, and R. P. Leavitt, "Self-Starting Passively Mode-Locked Tunable Femtosecond Cr^{4+}:YAG Laser Using a Saturable Absorber Mirror" *Optics Communications*, Vol. 137, pp 55-58, 1997.

47. M. J. Hayduk, S. T. Johns, M. F. Krol, C. R. Pollock, and R. P. Leavitt, "Broadly Tunable Saturable Absorber Mode-locked Cr^{4+}:YAG Femtosecond Laser", *IEEE Lasers and Electro-Optics Society Annual Meeting*, Nov. 1996, Paper MF3.

48. M. J. Hayduk, S. T. Johns, and M. F. Krol, "Saturable Absorber Mode-Locked Femtosecond Cr^{4+}:YAG Laser", *SPIE Proceedings*, Vol. 3075, Apr. 1997, pp. 10-15.

49.   S. Gupta, J. F. Whitaker, and G. A. Mourou, "Ultrafast Carrier Dynamics in III-V Semiconductors Grown by Molecular-Beam Epitaxy at Very Low Substrate Temperatures" *IEEE J. Quantum Electron.*, Vol. 28, No. 10, 1992, pp. 2464-2472.

50.   R. Takahashi, Y. Kawamura, T. Kagawa, and H. Iwamura, "Ultrafast 1.55-µm Photoresponse in Low-Temperature-Grown InGaAs/InAlAs Quantum Wells", *Appl. Phys. Lett.*, Vol. 65, No. 14, 1994, pp. 1790-1792.

51.   N. Peyghambarian, S. W. Koch, A. Mysyrowicz, *Introduction to Semiconductor Optics*, (Prentice-Hall, Englewood Cliffs, NJ.), 1993, Chapter XIV.

52.   Akira Hirano, Hiroyuki Tsuda, Hideki Kobayashi, Ryo Takahashi, Masaki Asobe, Kenji Sato, and Kazuo Hagimoto, "All-Optical Discrimination Based Nonlinear Transmittance of MQW Semiconductor Optical Gates", *IEEE J. Light. Tech.*, Vol. 17, No. 5, 1999, pp. 873-884.

53.   M. F. Krol, T. Ohtsuki and G. Khitrova, R. K. Boncek, B. P. McGinnis, H. M. Gibbs, and N. Peyghambarian, "All-Optical, High Contrast GaAlInAs Multiple Quantum Well Asymmetric Reflection Modulator at 1.3 µm", *Appl. Phys. Lett.* Vol. 62, No. 13, 1993, pp. 1550-1552.

54.   D. T. Neilson, J. E. Ehrlich, P. Meredith, A. C. Walker, G. T. Kennedy, R. S. Grant, P. D. Roberts, W. Sibbett, M. Hopkinson and M. Pate, "Submilliwatt Optical Bistability in a Coated InGaAs/InP Multiquantum Well waveguide Fabry-Perot Cavity", *Elec. Lett.* Vol. 29, No. 17, 1993, pp. 1537-1539.

55.   Elsa Garmire, "Criteria for Optical Bistability in a Lossy Saturating Fabry-Perot", *IEEE J. Quantum Electron., Vol. 25, No. 3, 1989, pp. 289-295.*

56.   Zane Shellenbarger and Joseph H. Abeles, "Bistable Reflective Etalon (BRET)", *AFRL-SN-RS-TR-2003-210*, Sep 2003.

57.   Paul K. L. Yu, S. S. Lau, W. X. Chen, A. R. Clawson, G. L. Li, Q. Z. Liu, D. S. Shin, Yang Wu, Q. J. Xing, and J. T. Zhu, "Photonics Circuits Technology for RF Photonics Systems", *AFRL-SN-RS-TR-2000-150*, Oct. 2000.

58.   Paul K. L. Yu, A. R. Clawson, G. L. Li, Yuling Zhuang, D. S. Shin, Phil Mages, "Semiconductor Photonic Components for RF Applications", *AFRL-SN-RS-TR-2001-125*, Jun. 2001.

59.   Paul K. L. Yu, Yang Wu, G. L. Li, Yuling Zhuang, Phil Mages, A. R. Clawson, and W. X. Chen, "Semiconductor Photonic Components for RF Applications", *AFRL-SN-RS-TR-2002-214*, Aug. 2002.

60.   P. K. L. Yu, Y. Wu, A. Chan, Y. Zhuang, J. Fischer, A. R. Clawson, I. Shubin, G. L. Li, and W. X. Chen, "Wideband Electroabsorption Modulator for Microwave Photonics", *AFRL-SN-RS-TR-2004-281*, Oct. 2004.

61. L. M. Johnson and H. V. Roussell, "Reduction of Intermodulation Distortion in Interferometric Optical Modulators," *Opt. Lett.*, Vol. 13, No. 10., 1988, pp. 928–930.

62. S. A. Hamilton, D. R. Yankelevich, A. Knoesen, R. T. Weverka, and R. A. Hill, "Comparison of an In-Line Asymmetric Directional Coupler Modulator with Distributed Optical Loss to Other Linearized Electrooptic Modulators", *IEEE Trans. Microwave Theory Tech.*, Vol. 47, No. 7, 1999, pp. 1184–1192.

63. Robert B. Welstand, *High Linearity Modulation and Detection in Semiconductor Electroabsorption Waveguides*, University of California, San Diego, Ph.D. Dissertation, 1997, Chapter 3.

64. G. L. Li and P. K. L. Yu, "Optical Intensity Modulators for Digital and Analog Applications", *IEEE J. Light. Tech.*, Vol. 21, No. 9, 2003, pp. 2010-2030.

65. G. L. Li, C. K. Sun, S. A. Pappert, W. X. Chen, and P. K. L. Yu, "Ultrahigh- Speed Traveling-Wave Electroabsorption Modulator – Design and Analysis", *IEEE Trans. Microwave Theory Tech.*, Vol. 47, No. 7, 1999, pp. 1177-1183.

66. Y. Zhuang, W. S. C. Chang, P. k. L. Yu, "Peripheral-Coupled Waveguide MQW Electroabsorption Modulator for Near Transparency and High Spurious Free Dynamic Range RF Fiber Optic Link", *IEEE Photonics Technology Letters*, Vol. 16, No. 9, 2004, pp. 2033-2035.

67. J. X. Chen, Y. Wu, W. X. Chen, I. Shubin, A. Clawson, W. S. C. Chang, P. K. L. Yu, "High-Power Intrastep Wuantum Well Electroabsorption Modulator Using Single-Sided Large Optical Cavity Waveguide", *IEEE Photon. Tech. Lett.*, Vol. 16, No. 2, 2004, pp. 440-442.

68. Dong-Soo Shin, Paul K. L. Yu, Steve Pappert, "High-Power Electroabsorption Modulator Using Intra-Step-Barrier Quantum Wells", *J. of Appl. Phys.*, Vol. 89, No. 2, 2001, pp. 1515-1517.

69. G. Silverman, J. SooHoo, P. Yu, and I. Shubin, "Wideband Frequency-Agile High-SFDR Receiver Front End", *GOMAC Tech Conference*, 2005.

70. Leopold E. Pellon, "Bandpass Multibit ΣΔ Modulator Digital Receiver Topology and Its Applications", *IEEE Int'l. Microwave Symposium*, 2005.

71. D. Von der Linde, "Characterization of the Noise in Continuously Operating Mode-Locked Laser," *Appl. Phys. B*, Vol. 39, No. 4, 1986, pp. 201-217.

72. H. A. Haus, "Noise of Mode-Locked Lasers", *IEEE J. Quantum Electron.*, Vol. 29, No. 3, March 1993, pp. 983-996.

73.   S. B. Darack, D. R. Dykaar, and G. T. Harvey, "Timing-Jitter Stabilization of a Colliding-Pulse Mode-Locked Laser by Active Control of the Cavity Length", *Opt. Lett*. Vol. 16, No. 21, Nov. 1991, pp. 1677-1679.

74.   D. J. Derickson, P. A. Morton, J. E. Bowers, and R. L. Thornton, "Comparison of Timing Jitter in External and Monolithic Cavity Mode-Locked Semiconductor Lasers", *Appl. Phys. Lett*., Vol. 59, No. 26, Dec. 1991, pp. 3372-3374.

75.   Leaf A. Jiang, Matthew E. Grein, Erich P. Ippen, Cameron McNeilage and Jesse Searls, and Hiroyuki Yokoyama, "Ultra-Low Noise Semiconductor Modelocked Lasers for OTDM Applications", Poseidon Scientific Instrument library site
http://www.psi.com.au/Pages/LibraryPublished/mit-psi_optics_paper.pdf

76.   Peter J. Delfyett, "Development of a Compact, Low Jitter Modelocked Semiconductor Diode Laser", *AFRL-SN-RS-TR-2003-49*, Mar 2003.

77.   C. M. DePriest, T. Yilmaz, and P. J. Delfyett, Jr, S. Etemad, A. Braun, and J. Abeles, "Ultralow Noise and Supermode Suppression in an Actively Mode-Locked External-Cavity Semiconductor Diode Ring Laser, *Opt. Lett.,* Vol. 27, No. 9, May 2002, pp. 719-721.

78.   Peter J. Delfyett, "Stabilization of the Absolute Frequency and Phase of a Compact, Low Jitter Modelocked Semiconductor Diode Laser", *AFRL-SN-RS-TR-2005-63*, Mar 2005.

79.   M. J. Hayduk, M. F. Krol, C. R. Pollock, K. J. Teegarden, G. W. Wicks, and W. Kaechele, "Passively Mode-Locked Picosecond Erbium-Doped Fiber Lasers Using Multiple Quantum Well Satuarable Absorbers", *SPIE Proceedings*, Vol. 3384, 1998.

80.   J. W. Haus, M. J. Hayduk, W. Kaechele, G. Shaulov, K. Teegarden, J. Theimer, and G. Wicks, "Pulse Characteristics of a Mode-Locked Fiber Laser", *IEEE Lasers and Electro-Optics Society Annual Meeting*, 1998, Paper ThJ4.

81.   Ertan Salik, Nan Yu, and Lute Maleki, "Coupled OptoElectronic Oscillator for Generating Both RF Signal and Optical Pulses", *J. of Light. Tech.*, Vol. 18, No. 1, 2000, pp. 73-78.

82.   W. Ng and Y. M. So, "Characterizations of Absolute Phase Noise in fiber-Laser Modelocked by Sapphire-Loaded Cavity Resonator Oscillator at 10 GHz, *Elec. Lett.,* Vol. 40, No. 11, May 2004, pp. 672-674.

83.   R. J. Bussjager, M. J. Hayduk, S. T. Johns, E. W. Taylor, "Gamma-Ray Induced Responses in an Erbium-Doped Fiber Laser", *2001 IEEE Aerospace Conference Proceedings* on CD ROM, ISBN # 0-7803-6600-X, Mar. 10-17, 2001, Track no. 5.0202.

84.   R. J. Bussjager, M. J. Hayduk, S. T. Johns and E. W. Taylor, "Gamma-Ray Induced Pulse Width Broadening and Power Loss in a Mode-Locked Er-Doped Fiber Laser", *Elec. Lett.*, Vol. 37, No. 22, 2001.

85. R. J. Bussjager, M. J. Hayduk, S. T. Johns, and E. W. Taylor, "Comparison of Radiation-Induced Passive and Dynamic Responses in Two Erbium-Doped Fiber Lasers", *2002 IEEE Aerospace Conference Proceedings* on CD ROM, ISBN #: 0-7803-7232-8, Mar. 2002, Track No. 5.0101.

86. Rebecca J. Bussjager, Michael J. Hayduk, Steven T. Johns, Linda R. Taylor, Edward W. Taylor, "Gamma-Ray Induced Damage and Recovery Behavior in an Erbium-Doped Fiber Laser", *SPIE Proceedings,* Vol. 4547, Sep. 2001, pp.126-133.

87. J. Stich, C. Drèze, D. Pollex, K. Warbrick, K. Lowe, E. Best, T. Wilson, P. Corr & G. Weston, "The Use of III-V ICs in WDM Optical Network Equipment", *17th IEEE GaAs IC Symp. Tech. Dig*., Oct. 1995, pp. 177-180.

88. T. Sizer II, R. E. LaMarche, and T. K. Woodard, "Point Source Heating Effects in Multiple Quantum Well Modulators", *Appl. Phys. Lett*. Vol. 61, No. 4, 1992, pp. 420-422.

89. H. Takahashi, Y. Ohmori, and M. Kawachi, "Design and Fabrication of Silica-Based Integrated Optic 1x128 Power Splitter", *Elec. Lett.,* Vol. 27, No. 23, 1991, pp. 2131-2133.

Appendix A-HP 4155 Semiconductor Parameter Analyzer DC Measurements

GetVFdata2traces.vi

This virtual instrument (VI) is an example of how HP415xA subVIs can be used programmatically for a SWEEP mode operation.

It will initialize and close the instrument and driver.

Connector Pane
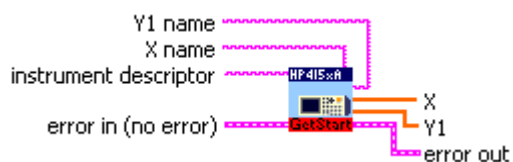
Front Panel
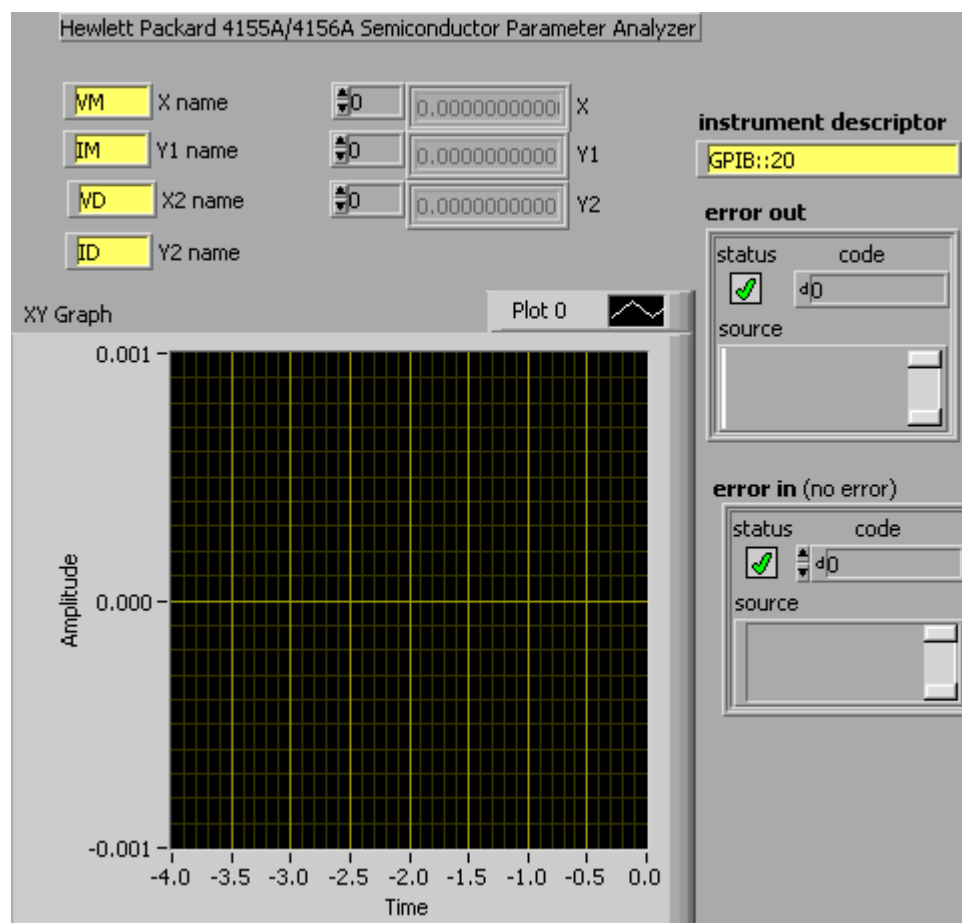
Block Diagram
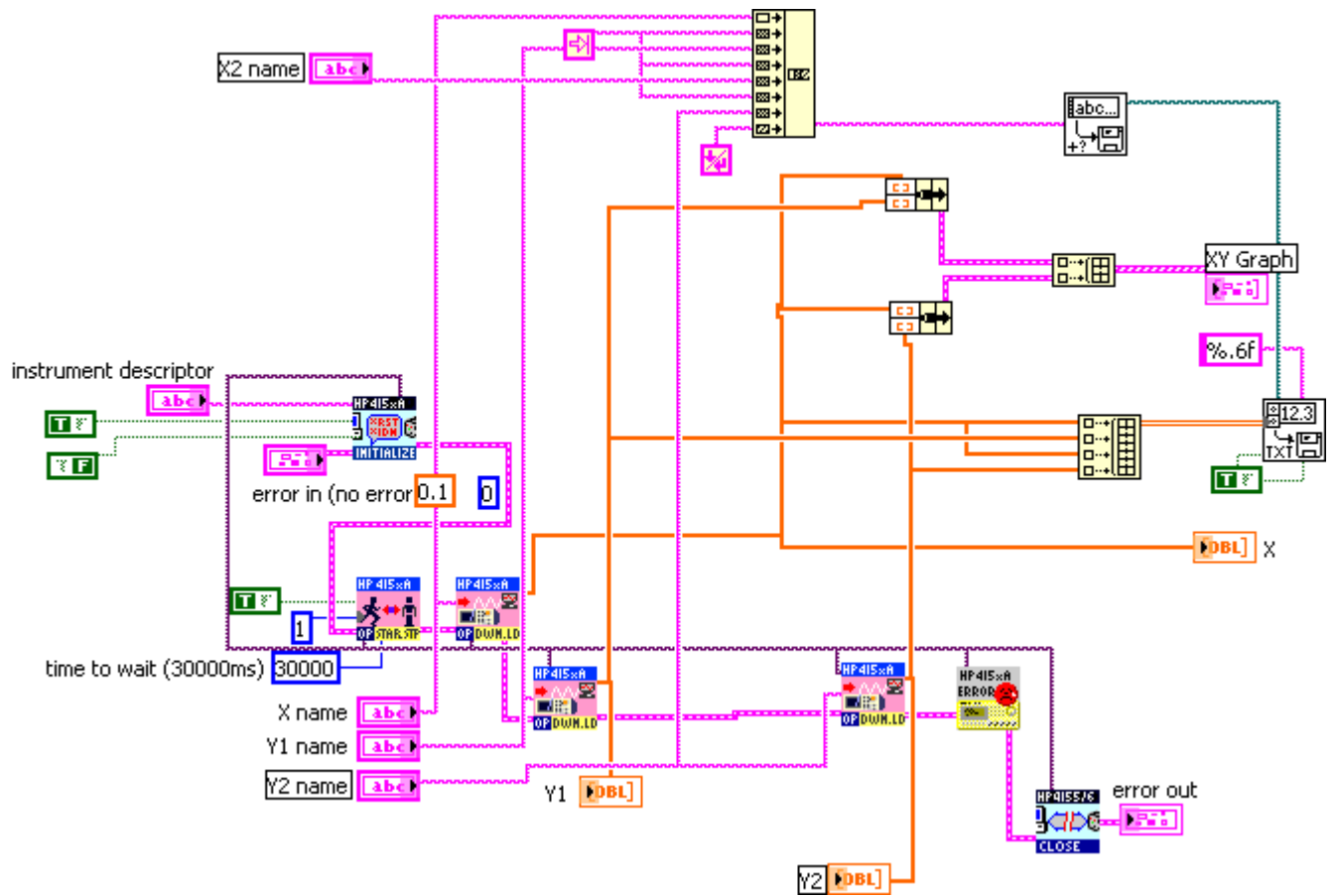
Appendix B: De-embedding S-Parameters for Microwave Probe

```
% load measured S11 (as G1, G2, G3) of combined probe and calibration
standards

clear
format short e

prompt={'S11 file for open:','S11 file for short:','S11 file for load:'};
default={'openprobe.dat','shortprobe.dat','loadprobe.dat'};
%default names -so if you save your data files with%
%these names they read in automatically.%
%Otherwise type in the names when prompted%

title='Input data files';
lineNo=1;
files=inputdlg(prompt,title,lineNo,default);

fid=fopen(char(files(1)),'rt');
x=fscanf(fid,'%15f');
N=length(x)/3;
fclose(fid);

fid=fopen(char(files(1)),'rt');
open=fscanf(fid,'%15f',[3,N]);
fclose(fid);
fid=fopen(char(files(2)),'rt');
short=fscanf(fid,'%15f',[3,N]);
fclose(fid);
fid=fopen(char(files(3)),'rt');
load=fscanf(fid,'%15f',[3,N])

fclose(fid);

G1=10.^(open(2,1:N)/20).*exp(i*open(3,1:N)*pi/180);  %converts  to  magnitude
file from VNA dB and phase format%
G2=10.^(short(2,1:N)/20).*exp(i*short(3,1:N)*pi/180);
G3=10.^(load(2,1:N)/20).*exp(i*load(3,1:N)*pi/180);

% Calculate reflection coefficients (g1, g2, g3) of calibration standards

f=load(1,1:N);    % frequency in GHz
w=2*pi*f;
Copen=-8.9;        % open capacitance in fF
Lshort=0;       % short inductance in pH
Lload=-5.4;        % load inductance in pH
% Cload=?;     % load capacitance in fF
Z1=1./(i*w*Copen*10^(-15));
Z2=i*w*Lshort*10^(-12);
Z3=50+i*w*Lload*10^(-12);
%Z3=50./(1+i*w*Cload*10^(-6));
g1=(Z1-50)./(Z1+50);
g2=(Z2-50)./(Z2+50);
g3=(Z3-50)./(Z3+50);

% calculate two-port S-parameters for probe
```

```
G12=G1-G2;
G23=G2-G3;
G31=G3-G1;
g12=g1.*g2;
g23=g2.*g3;
g31=g3.*g1;

A=g12.*G12+g23.*G23+g31.*G31;
B=g1.*G23+g2.*G31+g3.*G12;
C=G1.*g23.*G23+G2.*g31.*G31+G3.*g12.*G12;

S11p=C./A;
S22p=-B./A;
S21p=sqrt((G1-S11p).*(1-g1.*S22p)./g1);

% plot results

plot(f, 20*log10(abs(S11p)))
ylabel('S11 (dB)')
xlabel('Frequency (GHz)')

figure
plot(f, 20*log10(abs(S21p)))
ylabel('S21 (dB)')
xlabel('Frequency (GHz)')

figure
plot(f, 20*log10(abs(S22p)))
ylabel('S22 (dB)')
xlabel('Frequency (GHz)')

% write S-parameters into files

output1=[f;20*log10(abs(S11p));angle(S11p)*180/pi];
output2=[f;20*log10(abs(S21p));angle(S21p)*180/pi];
output3=[f;20*log10(abs(S22p));angle(S22p)*180/pi];

prompt={'File name for probe S11:','File name for probe S21:','File name for
probe S22:'};
default={'S11p.dat','S21p.dat','S22p.dat'};
title='output file names';
lineNo=1;
output_files=inputdlg(prompt,title,lineNo,default);
fopen(char(output_files(1)),'wt');
fprintf(fid,'%13f   %13f   %13f\n',output1);
fclose(fid);
fopen(char(output_files(2)),'wt');
fprintf(fid,'%13f   %13f   %13f\n',output2);
fclose(fid);
fopen(char(output_files(3)),'wt');
fprintf(fid,'%13f   %13f   %13f\n',output3);
fclose(fid);
```

Appendix C: De-embedding Frequency Response for Modulator

```
% load calibration data and measured link S21 and S11

clear
format short e

prompt={'Measured link S11 file:','Measured link S21 file:','Detector data
file:',...
      'Probe S21 data file:','Probe S11 data file:','Probe S22 data file:'};
default={'c48VNAs11801.dat','c48VNAs21801.dat','dummydet.dat','S21p801.dat',.
..
        'S11p801.dat','S22p801.dat'};
title='Input data files';
lineNo=1;
files=inputdlg(prompt,title,lineNo,default);

fid=fopen(char(files(1)),'rt');
x=fscanf(fid,'%15f');
fclose(fid);
N=length(x)/3

fid=fopen(char(files(1)),'rt');
s11l=fscanf(fid,'%f',[3,N]);
fclose(fid);
fid=fopen(char(files(2)),'rt');
s21l=fscanf(fid,'%15f',[3,N]);
fclose(fid);
fid=fopen(char(files(3)),'rt');
det=fscanf(fid,'%15f',[3,N]);
fclose(fid);
fid=fopen(char(files(4)),'rt');
s21p=fscanf(fid,'%15f',[3,N]);
fclose(fid);
fid=fopen(char(files(5)),'rt');
s11p=fscanf(fid,'%15f',[3,N]);
fclose(fid);
fid=fopen(char(files(6)),'rt');
s22p=fscanf(fid,'%15f',[3,N]);
fclose(fid);

S11p=10.^(s11p(2,1:N)/20).*exp(i*s11p(3,1:N)*pi/180);  %files  read  in  from
output of OurCaliProb
S22p=10.^(s22p(2,1:N)/20).*exp(i*s22p(3,1:N)*pi/180);
S21p=10.^(s21p(2,1:N)/20).*exp(i*s21p(3,1:N)*pi/180);
%Det=10.^(det(2,1:N)/20); %don't need to use if use the Lightwave. Only use
if have an external detector.
S21VNA=10.^(s21l(2,1:N)/20).*exp(i*s21l(3,1:N)*pi/180);
S11VNA=10.^(s11l(2,1:N)/20).*exp(i*s11l(3,1:N)*pi/180);

% calculate frequency response for modulator

X=S21p.^2+(S11VNA-S11p).*S22p;
S21m=(S21VNA.*S21p)./(X);
%S21m=(S21VNA.*S21p)./(X.*Det); Don't need this if use the lightwave
S11m=(S11VNA-S11p)./X;
```

```
% plot results

%polar(angle(S11m), abs(S11m))

figure
f=s11p(1,1:N);     % frequency in GHz
plot(f, 20*log10(abs(S11m)))
ylabel('S11m (dB)')
xlabel('Frequency (GHz)')

figure
plot(f, 20*log10(abs(S21m)))
ylabel('S21m (dB)')
xlabel('Frequency (GHz)')


% write S-parameters into files

output1=[f;20*log10(abs(S11m));angle(S11m)*180/pi];
output2=[f;20*log10(abs(S21m))];

prompt={'File name for modulator S11:','File name for modulator S21:'};
default={'\\E016ya080018\PCUsers\PhotonicADC\EA
Modulator\S11_mod.dat','\\E016ya080018\PCUsers\PhotonicADC\EA
Modulator\S21_mod.dat'};
title='output data files';
lineNo=1;
output_files=inputdlg(prompt,title,lineNo,default);

fopen(char(output_files(1)),'wt');
fprintf(fid,'%13f   %13f   %13f\n',output1);
fclose(fid);
fopen(char(output_files(2)),'wt');
fprintf(fid,'%13f   %13f\n',output2);
fclose(fid);
```

Appendix D: IM3 Controlled Experiment
IM-3rdOrder_HP8673E_E4448A.vi

Front Panel

Block Diagram

Measure 2F2-F1

Ave
8673E

Set to Frequency 2F2-F1

Center Frequency
:FREQ:CENT

HP
W

2*F2-F1

96
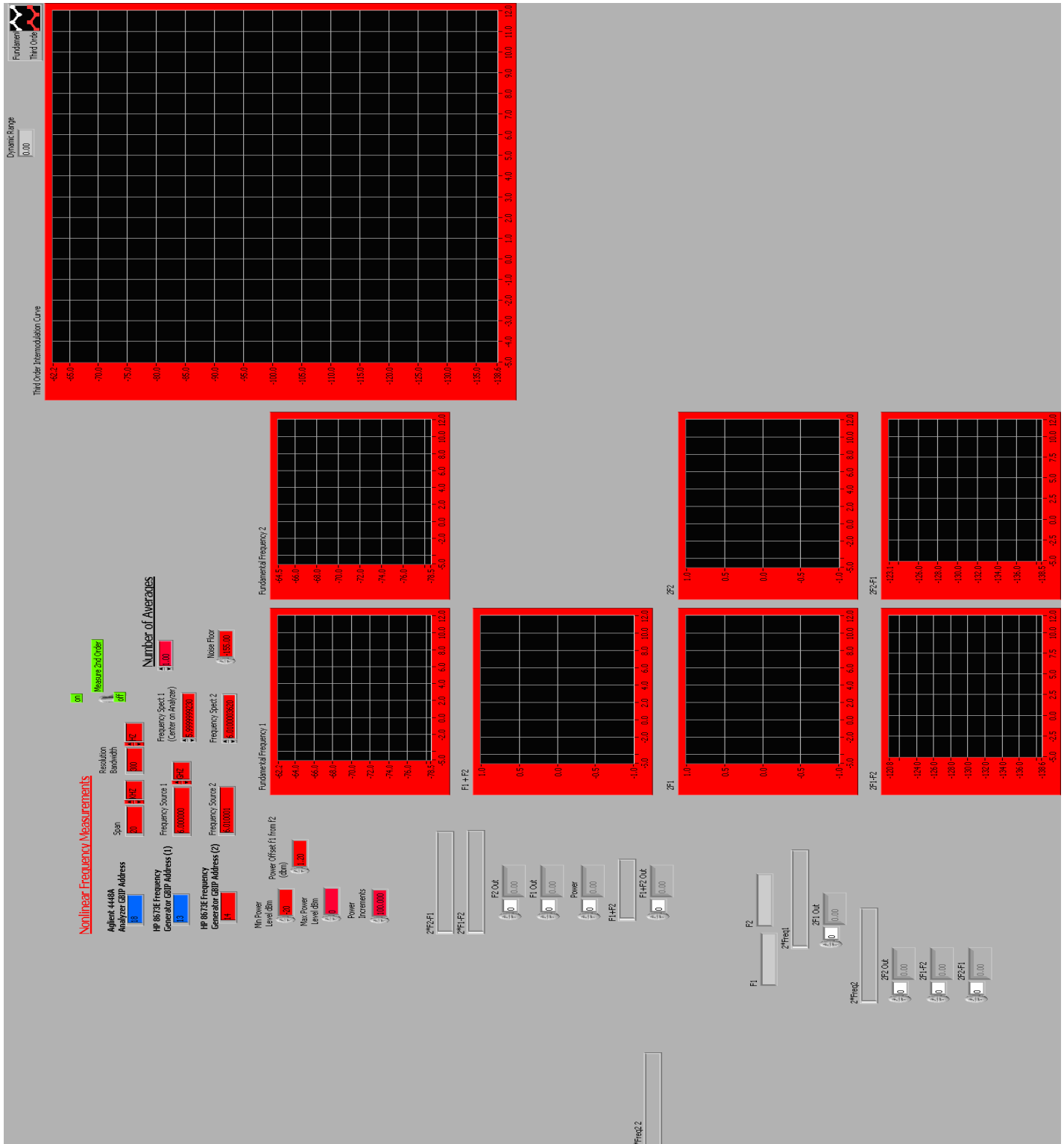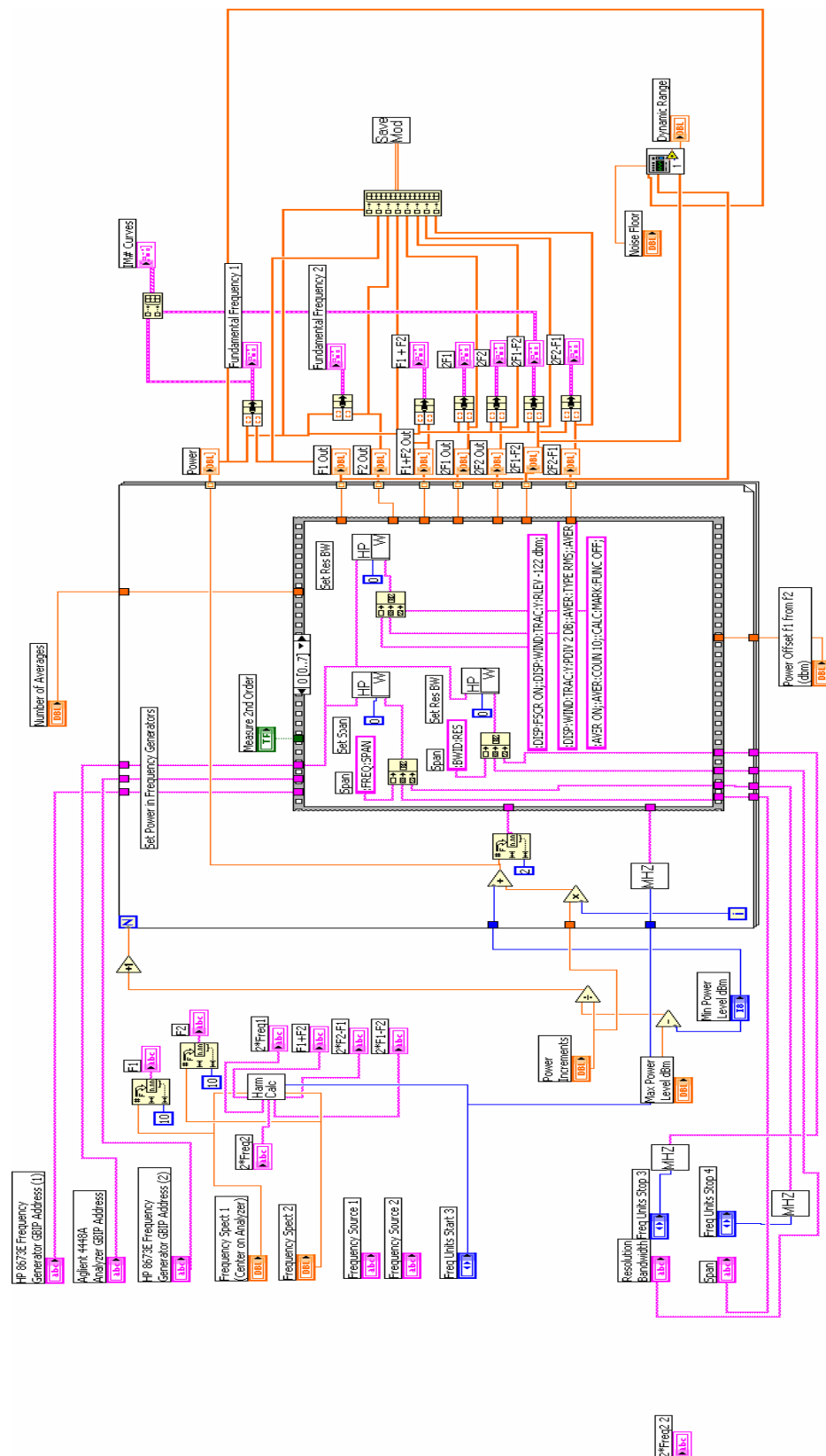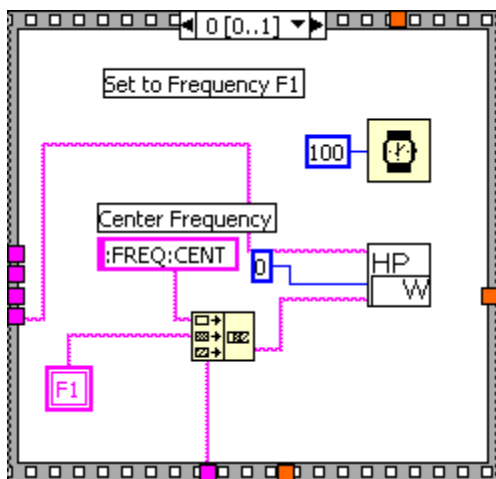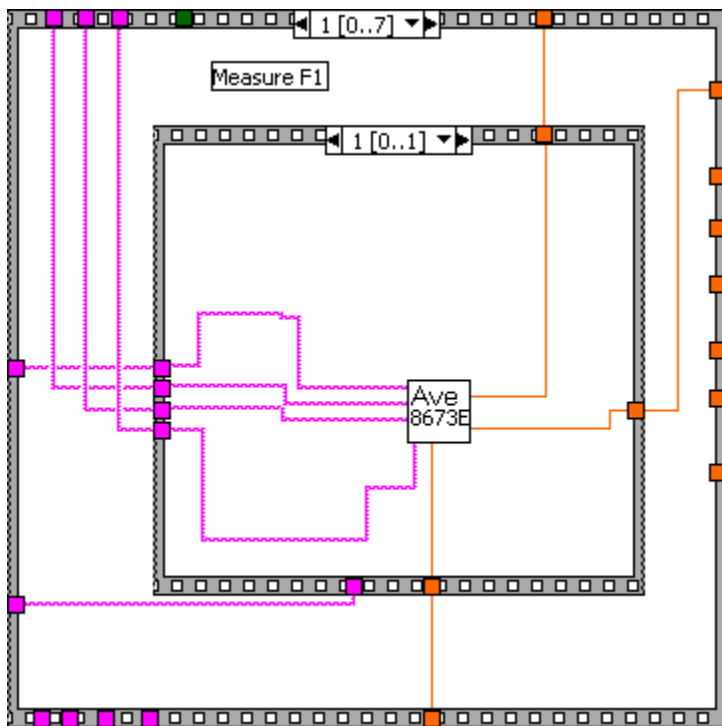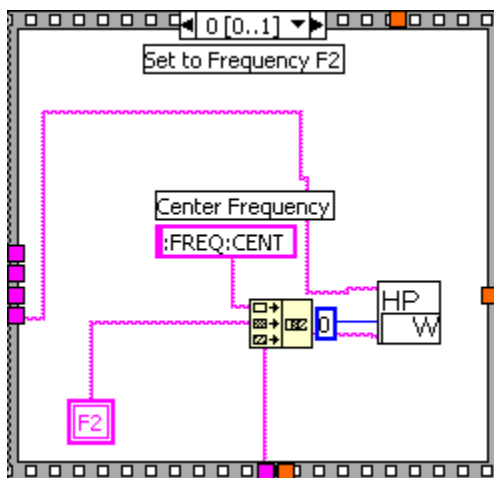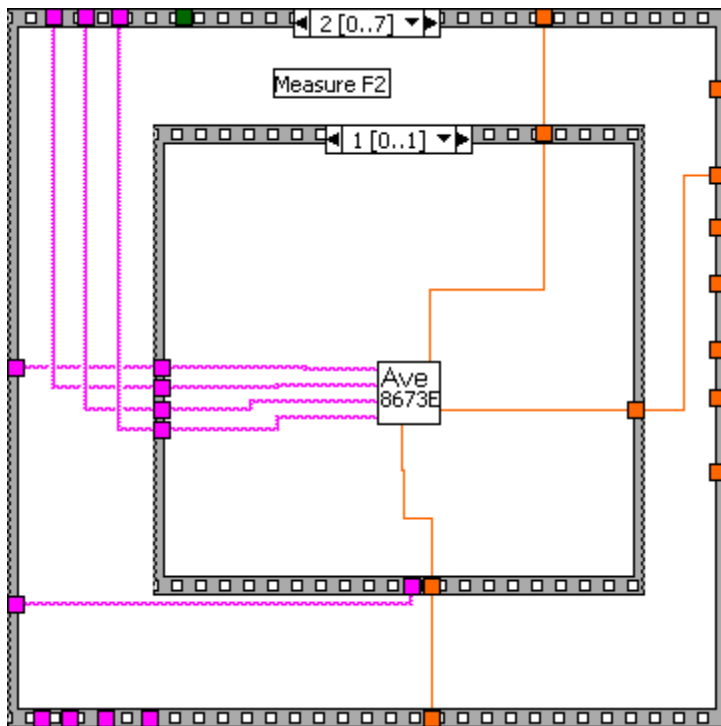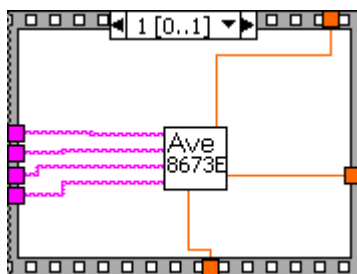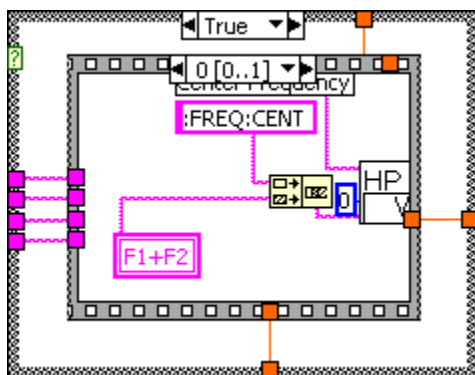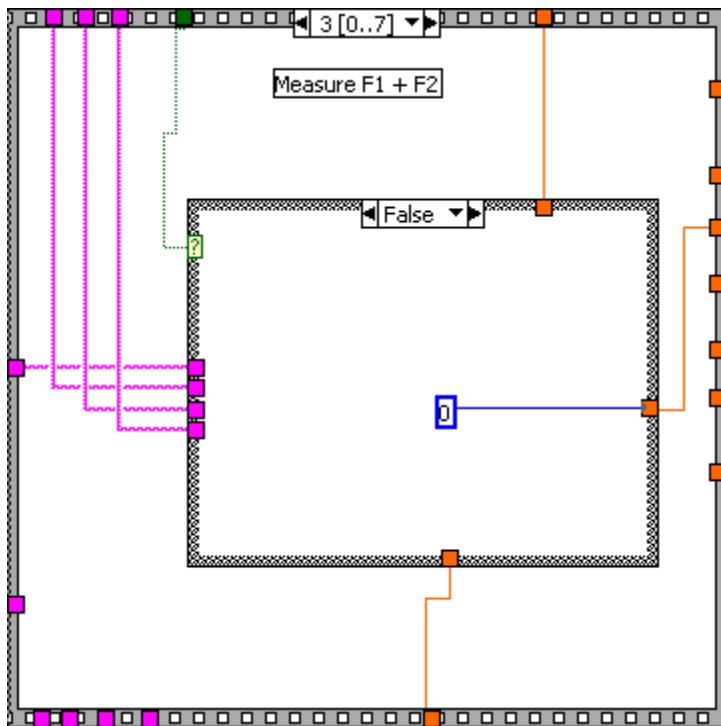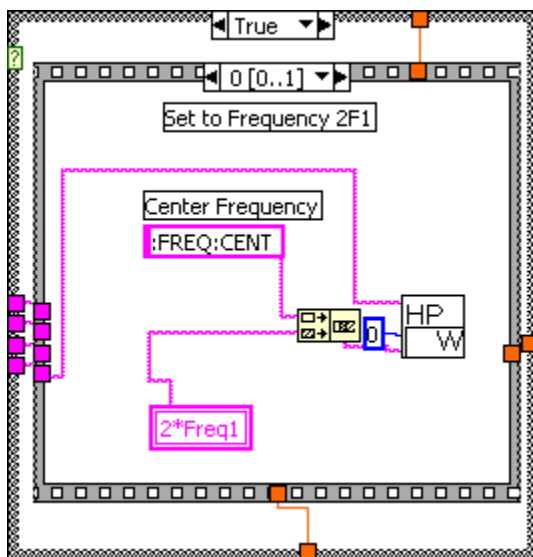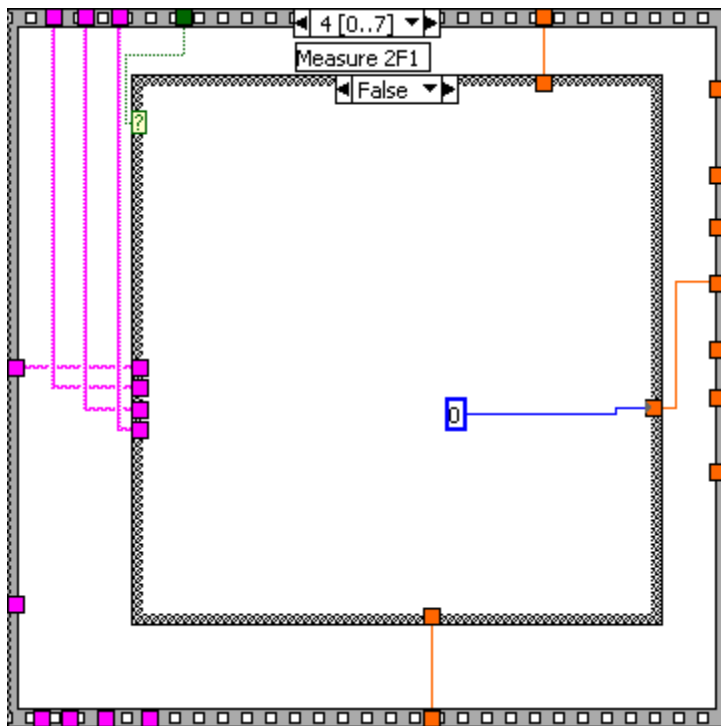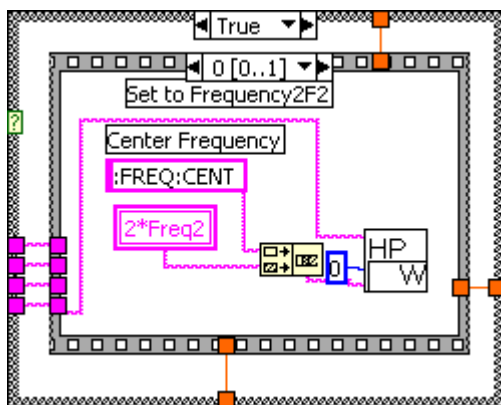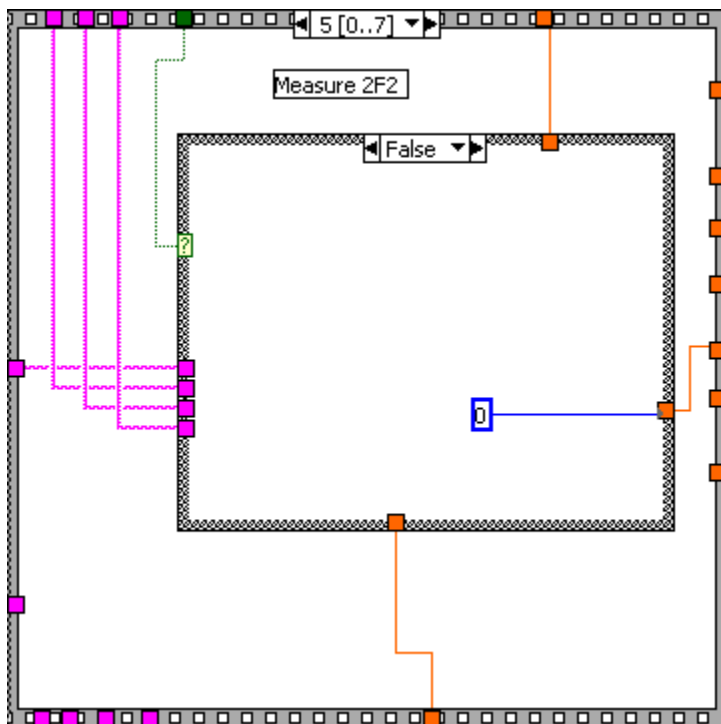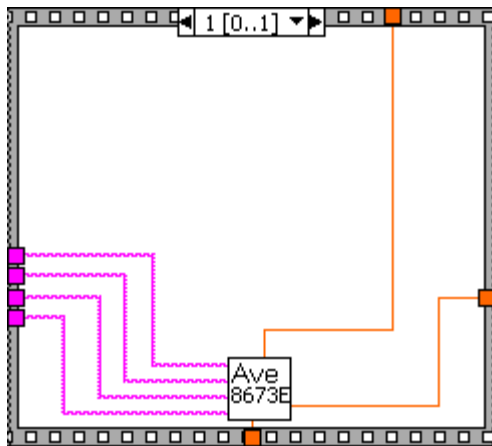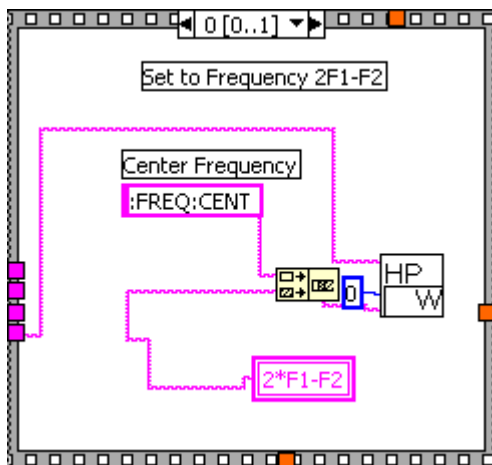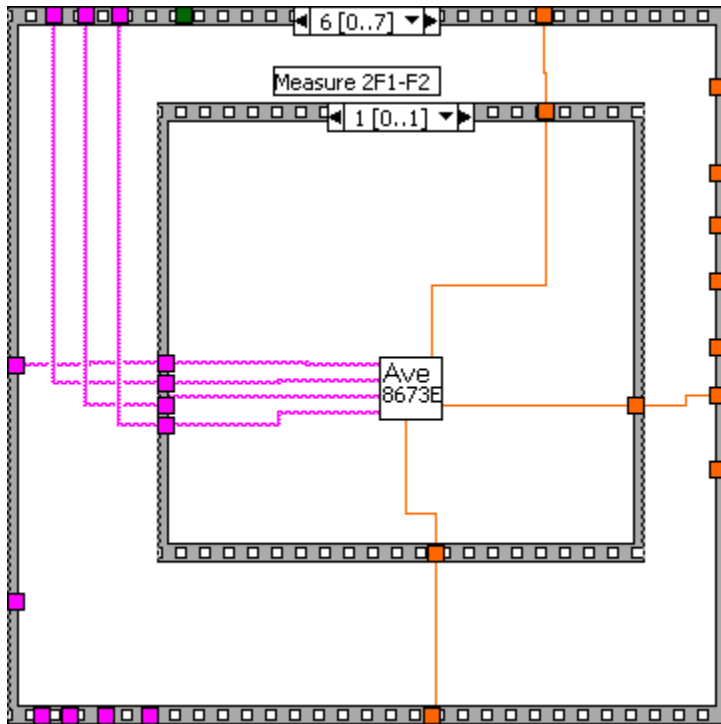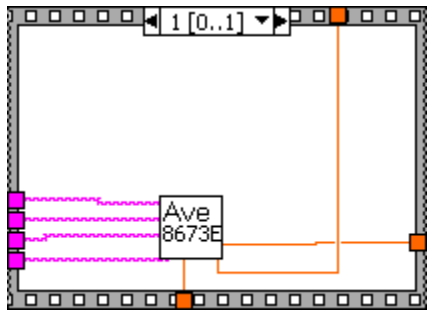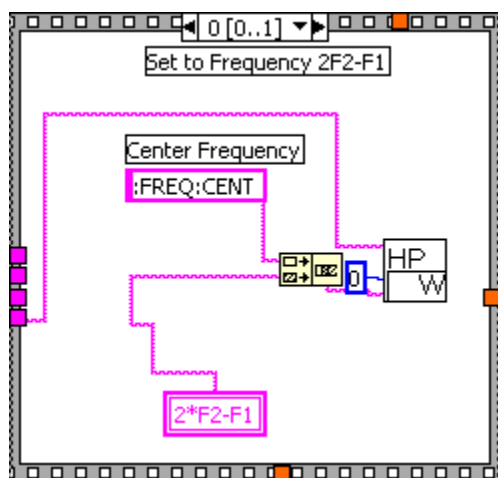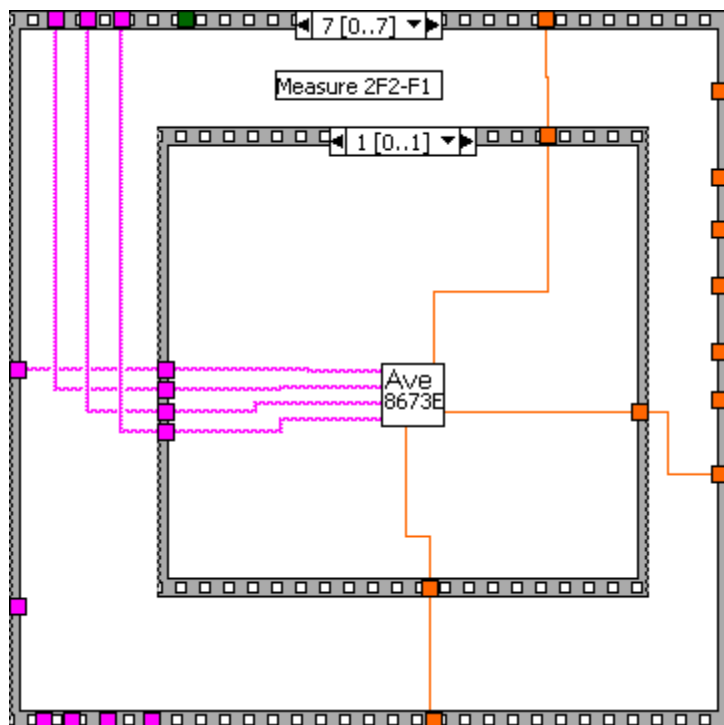
Appendix E: MathCAD Routine for Calculating Noise Floor

$mW := 10^{-3} \cdot W$ $dB(x) := 10 \cdot \log(x)$ $dBm(P) := dB\left(\dfrac{P}{1 \cdot mW}\right)$ $R_l := 50\,\Omega$

$c := 2.9998 \cdot 10^8 \cdot m \cdot s^{-1}$ $hh := 6.626 \cdot 10^{-34} \cdot J \cdot s$ $ee := 1.602 \cdot 10^{-19} \cdot C$ $kb := 1.381 \cdot 10^{-23}$ $Tk := (22 + 273.15) \cdot K$ $Tk = 295.15\,K$

$v := \dfrac{c}{1550 \cdot 10^{-9} \cdot m}$ $v = 1.93 \times 10^{14}\,\dfrac{1}{s}$ $INVdB(x) := \sqrt[10]{10^x}$

$k := kb \cdot J \cdot K^{-1}$ $dBm\left(k \cdot Tk \cdot s^{-1}\right) = -173.9$

Nominal Power

$P_L := 2 \cdot mW$ Change this power to see detector current and noise floor results

Modulator Loss $L_M := 0.4$ $dB(L_M) = -3.98$

Fiber Loss $L_F := 0.45$ $dB(L_F) = -3.47$

Responsivity $\eta_D := .8 \cdot A \cdot W^{-1}$

$\dfrac{ee \cdot P_L}{hh \cdot v} = 2.5 \times 10^{-3}\,A$

Nominal PD Current

$I_d := P_L \cdot L_M \cdot L_F \cdot \eta_D$ $\boxed{I_d = 2.8800 \times 10^{-4}\,A}$

$P_{Det} := P_L \cdot L_M \cdot L_F$ $P_{Det} = 3.6 \times 10^{-4}\,W$

Id of ~3mA give shot noise limit of -163dBm
Use PL=12mW if all else is the same

Laser RIN

$RINdB := -160$ Change RIN here

Could be as good as -165!

$RIN := 10^{\frac{RINdB}{10}} \cdot Hz^{-1}$

$INtherm := \sqrt{\dfrac{4 \cdot k \cdot Tk \cdot 1}{R_l}}$

$INtherm = 1.81 \times 10^{-11}\,s^{\frac{1}{2}} \cdot A$

$Ntherm := \dfrac{INtherm^2}{4} \cdot R_l \cdot s^{-1}$

$N_{Shot} := 2 ee \cdot I_d \cdot R_l \cdot s^{-1}$

$N_{RIN} := RIN \cdot I_d^2 \cdot R_l \cdot s^{-1}$

$N_{Out} := Ntherm + N_{Shot} + N_{RIN}$

Quantum Efficiency

$\eta := 0.56$

$iShot := \sqrt{\dfrac{2 \cdot ee^2 \cdot \eta \cdot P_{Det} \cdot 1 \cdot Hz}{hh \cdot v}}$ Boyd eq.8.53

$P_{Shot} := iShot^2 \cdot R_l$

$dBm(P_{Shot}) = -173.94$ This is here just as a check

Noise Terms

$dBm(Ntherm) = -173.9$ See Pozar eq. 10.3 for factor of 4 Vn is rms voltage

$dBm(N_{Shot}) = -173.36$

$dBm(N_{RIN}) = -183.82$

Noise Floor before postAmp

$\boxed{dBm(N_{Out}) = -170.41}$

$G_{86017A} := 42.4$ $Nf_{86017A} := 6.7$ $Attn := 19.8$ see file: \\E016\ya080018\pcusers\PhotonicADC\John\EAM SFDR\HPA83017A_Gain_NF.xls or graphs on following pages

Appendix F: Excel Spreadsheet for Calculating SFDR from Measured Data

F1=1.055 GHz
F2=1.076 GHz

Plot calculated SFDR for f1

-16.575	-166.7
-16.575	81.015668

Plot calculated SFDR for f2

-15.327	-166.7
-15.327	79.165684

Regression table:

	F1	F2	F1+F2	2*F1	2*F2	2*F1 - 2*F2	2*F2 - F1	TOI F1,2*F1-F2
	Intercept	Intercept	Intercept	Intercept	Intercept	Intercept	Intercept	Intercept
	-58.62	-58.61	0.00	0.00	0.00	-117.38	-118.08	-9.72
	Slope	Slope	Slope	Slope	Slope	Slope	Slope	
	1.351	1.341	0.000	0.000	0.000	2.975	3.173	

SFDR TOI	Calculated SFDR:
104.653	3rd order f1= 85.684
	3rd order f2= 87.534

	x value for f2	-15.327	y value for f2	-79.16568368
x value for f1	-16.575	y value for f1	-81.0157	

F1=1.055 GHz
F2=1.076 GHz

Main data table (GHz):

Power In dB	F1	F2	F1+F2	2*F1	2*F2	0 2*F1-F2	2*F2-F1	Pin	Fit f1	Fit f2	Fit 2f1-f2	Fit 2f2-f1	Noise Floor
-5	-65.49	-65.43	0	0	0	-132.12	-133.9	-180	-301.85	-300.04	-652.93	-689.13	-166.7
-4.5	-64.72	-64.69	0	0	0	-130.91	-132.56	-178	-299.14	-297.36	-646.98	-682.79	-166.7
-4	-64.02	-63.98	0	0	0	-129.62	-130.3	-176	-296.44	-294.67	-641.03	-676.44	-166.7
-3.5	-63.31	-63.26	0	0	0	-127.71	-129.32	-174	-293.74	-291.99	-635.08	-670.10	-166.7
-3	-62.61	-62.54	0	0	0	-126.15	-127.75	-172	-291.04	-289.31	-629.13	-663.75	-166.7
-2.5	-61.92	-61.88	0	0	0	-124.53	-126.19	-170	-288.33	-286.63	-623.18	-657.41	-166.7
-2	-61.27	-61.23	0	0	0	-123.32	-124.26	-168	-285.63	-283.94	-617.23	-651.06	-166.7
-1.5	-60.6	-60.57	0	0	0	-122	-122.89	-166	-282.93	-281.26	-611.28	-644.72	-166.7
-1	-59.97	-59.95	0	0	0	-120.45	-121.17	-164	-280.23	-278.58	-605.33	-638.37	-166.7
-0.5	-59.33	-59.33	0	0	0	-118.84	-119.71	-162	-277.52	-275.89	-599.38	-632.03	-166.7
0	-58.72	-58.72	0	0	0	-117.4	-118.03	-160	-274.82	-273.21	-593.43	-625.68	-166.7
								-158	-272.12	-270.53	-587.48	-619.34	-166.7
								-156	-269.42	-267.85	-581.53	-612.99	-166.7
								-154	-266.71	-265.16	-575.58	-606.65	-166.7
								-152	-264.01	-262.48	-569.63	-600.30	-166.7
								-150	-261.31	-259.80	-563.68	-593.96	-166.7

-166.7

-166.7	-587.61	-557.72	-257.12	-258.61	-148
-166.7	-581.27	-551.77	-254.43	-255.90	-146
-166.7	-574.92	-545.82	-251.75	-253.20	-144
-166.7	-568.58	-539.87	-249.07	-250.50	-142
-166.7	-562.23	-533.92	-246.39	-247.80	-140
-166.7	-555.89	-527.97	-243.70	-245.09	-138
-166.7	-549.54	-522.02	-241.02	-242.39	-136
-166.7	-543.20	-516.07	-238.34	-239.69	-134
-166.7	-536.85	-510.12	-235.66	-236.99	-132
-166.7	-530.51	-504.17	-232.97	-234.28	-130
-166.7	-524.16	-498.22	-230.29	-231.58	-128
-166.7	-517.82	-492.27	-227.61	-228.88	-126
-166.7	-511.47	-486.32	-224.93	-226.18	-124
-166.7	-505.13	-480.37	-222.24	-223.47	-122
-166.7	-498.78	-474.42	-219.56	-220.77	-120
-166.7	-492.44	-468.47	-216.88	-218.07	-118
-166.7	-644.72	-611.28	-281.26	-282.93	-166
-166.7	243.59	221.80	94.30	95.43	114
-166.7	-473.40	-450.62	-208.83	-209.96	-112
-166.7	-467.06	-444.66	-206.15	-207.26	-110
-166.7	-460.71	-438.71	-203.47	-204.56	-108
-166.7	-454.37	-432.76	-200.78	-201.85	-106
-166.7	-448.02	-426.81	-198.10	-199.15	-104
-166.7	-441.68	-420.86	-195.42	-196.45	-102
-166.7	-435.33	-414.91	-192.74	-193.75	-100
-166.7	-428.99	-408.96	-190.05	-191.04	-98
-166.7	-422.64	-403.01	-187.37	-188.34	-96
-166.7	-416.30	-397.06	-184.69	-185.64	-94
-166.7	-409.95	-391.11	-182.01	-182.94	-92
-166.7	-403.61	-385.16	-179.32	-180.23	-90
-166.7	-397.26	-379.21	-176.64	-177.53	-88
-166.7	-390.91	-373.26	-173.96	-174.83	-86
-166.7	-384.57	-367.31	-171.28	-172.13	-84
-166.7	-378.22	-361.36	-168.59	-169.42	-82

SFDR for F1 Vs. 2F1-F2

MZ SFDR =85.684 Hz $^{2/3}$

F1=1.055 GHz; slope f1 = 1.351
F2=1.076 GHz; slope 2f1-f2 =2.975
0 V bias, P_{opt} =1.5 mW

RF Input Power (dBm)
RF Output Power (dBm)

SFDR for F2 Vs. 2F2-F1

MZ SFDR =87.534 Hz $^{2/3}$

F1=1.055 GHz; slope f2 = 1.341
F2=1.076 GHz; slope 2f2-f1 =3.173
0 V bias, P_{opt} =1.5 mW

RF Input Power (dBm)
RF Output Power (dBm)

-80	-166.72	-165.91	-355.41	-371.88	-166.7
-78	-164.02	-163.23	-349.46	-365.53	-166.7
-76	-161.31	-160.55	-343.51	-359.19	-166.7
-74	-158.61	-157.86	-337.55	-352.84	-166.7
-72	-155.91	-155.18	-331.60	-346.50	-166.7
-70	-153.21	-152.50	-325.65	-340.15	-166.7
-68	-150.50	-149.82	-319.70	-333.81	-166.7
-66	-147.80	-147.13	-313.75	-327.46	-166.7
-64	-145.10	-144.45	-307.80	-321.12	-166.7
-62	-142.40	-141.77	-301.85	-314.77	-166.7
-60	-139.69	-139.09	-295.90	-308.43	-166.7
-58	-136.99	-136.40	-289.95	-302.08	-166.7
-56	-134.29	-133.72	-284.00	-295.74	-166.7
-54	-131.59	-131.04	-278.05	-289.39	-166.7
-52	-128.88	-128.35	-272.10	-283.05	-166.7
-50	-126.18	-125.67	-266.15	-276.70	-166.7
-48	-123.48	-122.99	-260.20	-270.36	-166.7
-46	-120.78	-120.31	-254.25	-264.01	-166.7
-44	-118.07	-117.62	-248.30	-257.67	-166.7
-42	-115.37	-114.94	-242.35	-251.32	-166.7
-40	-112.67	-112.26	-236.40	-244.98	-166.7
-39	-111.32	-110.92	-233.42	-241.81	-166.7
-38	-109.97	-109.58	-230.44	-238.63	-166.7
-37	-108.62	-108.24	-227.47	-235.46	-166.7
-36	-107.26	-106.89	-224.49	-232.29	-166.7
-35	-105.91	-105.55	-221.52	-229.12	-166.7
-34	-104.56	-104.21	-218.54	-225.94	-166.7
-33	-103.21	-102.87	-215.57	-222.77	-166.7
-32	-101.86	-101.53	-212.59	-219.60	-166.7
-31	-100.51	-100.19	-209.62	-216.42	-166.7
-30	-99.16	-98.85	-206.64	-213.25	-166.7
-29.5	-98.48	-98.18	-205.16	-211.67	-166.7
-29	-97.81	-97.51	-203.67	-210.08	-166.7
-28.5	-97.13	-96.83	-202.18	-208.49	-166.7
-28	-96.45	-96.16	-200.69	-206.91	-166.7
-27.5	-95.78	-95.49	-199.20	-205.32	-166.7

-27	-95.10	-94.82	-197.72	-203.73	-166.7
-26.5	-94.43	-94.15	-196.23	-202.15	-166.7
-26	-93.75	-93.48	-194.74	-200.56	-166.7
-25.5	-93.08	-92.81	-193.25	-198.98	-166.7
-25	-92.40	-92.14	-191.77	-197.39	-166.7
-24.5	-91.72	-91.47	-190.28	-195.80	-166.7
-24	-91.05	-90.80	-188.79	-194.22	-166.7
-23.5	-90.37	-90.13	-187.30	-192.63	-166.7
-23	-89.70	-89.46	-185.82	-191.04	-166.7
-22.5	-89.02	-88.79	-184.33	-189.46	-166.7
-22	-88.35	-88.12	-182.84	-187.87	-166.7
-21.5	-87.67	-87.45	-181.35	-186.29	-166.7
-21	-86.99	-86.78	-179.87	-184.70	-166.7
-20.5	-86.32	-86.10	-178.38	-183.11	-166.7
-20	-85.64	-85.43	-176.89	-181.53	-166.7
-19.5	-84.97	-84.76	-175.40	-179.94	-166.7
-19	-84.29	-84.09	-173.91	-178.35	-166.7
-18.5	-83.62	-83.42	-172.43	-176.77	-166.7
-18	-82.94	-82.75	-170.94	-175.18	-166.7
-17.5	-82.27	-82.08	-169.45	-173.60	-166.7
-17	-81.59	-81.41	-167.96	-172.01	-166.7
-16.5	-80.91	-80.74	-166.48	-170.42	-166.7
-16	-80.24	-80.07	-164.99	-168.84	-166.7
-15.5	-79.56	-79.40	-163.50	-167.25	-166.7
-15	-78.89	-78.73	-162.01	-165.66	-166.7
-14	-77.54	-77.39	-159.04	-162.49	-166.7
-13	-76.18	-76.05	-156.06	-159.32	-166.7
-12	-74.83	-74.70	-153.09	-156.15	-166.7
-11	-73.48	-73.36	-150.11	-152.97	-166.7
-10	-72.13	-72.02	-147.14	-149.80	-166.7
-9	-70.78	-70.68	-144.16	-146.63	-166.7
-8	-69.43	-69.34	-141.19	-143.46	-166.7
-7	-68.08	-68.00	-138.21	-140.28	-166.7
-6	-66.73	-66.66	-135.24	-137.11	-166.7
-5	-65.37	-65.32	-132.26	-133.94	-166.7
-4	-64.02	-63.97	-129.29	-130.77	-166.7

-3	-62.67	-62.63	-126.31	-127.59	-166.7
-2	-61.32	-61.29	-123.34	-124.42	-166.7
-1	-59.97	-59.95	-120.36	-121.25	-166.7
0	-58.62	-58.61	-117.38	-118.08	-166.7
1	-57.27	-57.27	-114.41	-114.90	-166.7
2	-55.92	-55.93	-111.43	-111.73	-166.7
3	-54.56	-54.58	-108.46	-108.56	-166.7
4	-53.21	-53.24	-105.48	-105.39	-166.7
5	-51.86	-51.90	-102.51	-102.21	-166.7
6	-50.51	-50.56	-99.53	-99.04	-166.7
7	-49.16	-49.22	-96.56	-95.87	-166.7
8	-47.81	-47.88	-93.58	-92.70	-166.7
9	-46.46	-46.54	-90.61	-89.52	-166.7
10	-45.11	-45.20	-87.63	-86.35	-166.7
11	-43.75	-43.85	-84.66	-83.18	-166.7
12	-42.40	-42.51	-81.68	-80.01	-166.7
13	-41.05	-41.17	-78.71	-76.83	-166.7
14	-39.70	-39.83	-75.73	-73.66	-166.7
15	-38.35	-38.49	-72.76	-70.49	-166.7
16	-37.00	-37.15	-69.78	-67.32	-166.7
17	-35.65	-35.81	-66.80	-64.14	-166.7
18	-34.30	-34.47	-63.83	-60.97	-166.7
19	-32.94	-33.12	-60.85	-57.80	-166.7
20	-31.59	-31.78	-57.88	-54.63	-166.7
21	-30.24	-30.44	-54.90	-51.45	-166.7
22	-28.89	-29.10	-51.93	-48.28	-166.7
23	-27.54	-27.76	-48.95	-45.11	-166.7
24	-26.19	-26.42	-45.98	-41.93	-166.7
25	-24.84	-25.08	-43.00	-38.76	-166.7
26	-23.49	-23.74	-40.03	-35.59	-166.7
27	-22.13	-22.39	-37.05	-32.42	-166.7
28	-20.78	-21.05	-34.08	-29.24	-166.7
29	-19.43	-19.71	-31.10	-26.07	-166.7
30	-18.08	-18.37	-28.13	-22.90	-166.7
31	-16.73	-17.03	-25.15	-19.73	-166.7
32	-15.38	-15.69	-22.18	-16.55	-166.7

33	-14.03	-14.35	-19.20	-13.38	-166.7
34	-12.67	-13.01	-16.23	-10.21	-166.7
35	-11.32	-11.66	-13.25	-7.04	-166.7
36	-9.97	-10.32	-10.27	-3.86	-166.7